Prospects to Improve the Critical Current Density of Superconducting Nb_3Sn strands

DISSERTATION

Presented in Partial Fulfillment of the Requirements for the Degree Doctor of Philosophy in the Graduate School of The Ohio State University

By

Xingchen Xu

Graduate Program in Materials Science and Engineering

The Ohio State University

2016

Dissertation Committee:

Prof. Mike D. Sumption, Advisor

Prof. Sheikh Akbar

Prof. Hamish Fraser

Abstract

Superconducting Nb_3Sn strands are the key building block of high-field (>10 T) magnets. There are multiple figures of merit defining the quality of a Nb_3Sn strand, such as critical current density (J_c), residue resistivity ratio (RRR), and effective subelement size (d_{eff}), among which the high-field J_c is the key factor for the application of Nb_3Sn strands in magnets, because the supercurrent-carrying capability of Nb_3Sn strands essentially determines the limit of the magnetic field that can be generated in a fixed magnet design. It is the primary goal of this dissertation to explore how to improve the high-field non-matrix J_c of Nb_3Sn strands without sacrificing other factors (e.g., RRR and d_{eff}).

A green-state Nb_3Sn wire is composed of precursors including Sn, Cu, and Nb metals or alloys, which transform to superconducting Nb_3Sn phase through a diffusion reaction process during a heat treatment at typically 600-800 °C. Since the fabrication of the first Nb_3Sn wires in the early 1970s, the high-field non-matrix J_c of Nb_3Sn strands has been improved significantly due to the extensive efforts by the scientists of the Nb_3Sn community. These improvements in J_c were mainly driven by three aspects: improvement of the subelement design (i.e., optimizing the subelement architecture and the precursor amounts, e.g., enhancing the Nb and Sn fractions in subelements), use of the right type and amount of dopants, and optimization of the heat treatment schedules. However, the

improvement in J_c of Nb_3Sn strands has been saturated since 2002, with the rod-in-tube (RIT) strands pushing the 4.2 K, 12 T non-matrix J_c to ~3000 A/mm^2, and the 15 T value to ~1600 A/mm^2. After that progress in strand development was mainly achieved in reducing subelement size.

Given the plateau of J_c improvement for the last decade, researchers have been asking these questions: has the J_c of Nb_3Sn strands reached its limit? If not, what is the limit, and how to arrive there? These are also the questions that this dissertation aims to answer. For this goal, a literature review of the factors determining J_c of Nb_3Sn conductors is given in the "introduction" chapter. It is seen that the non-matrix J_c of Nb_3Sn strands are mainly determined by three factors: the fraction of current-carrying Nb_3Sn phase in a subelement, the irreversibility field B_{irr} which mainly depends on the Nb_3Sn phase composition (i.e., Sn content), doping, and strain state, and the flux-line pinning characteristics (including the maximum pinning force $F_{p,max}$ and the pinning force peak field) which mainly depend on grain size. Then these three parts will be addressed in three separate chapters. In chapter 3, the question "what is the maximum limit of Nb_3Sn fraction in a subelement" is investigated. A model is developed to predict the phase fractions in reacted strands based on the starting amounts of precursors. In chapter 4, a model is developed to find out what essentially determines the composition of non-stoichiometric compounds formed by diffusion reactions. It can be used as a guide for controlling the Sn content of the Nb_3Sn phase formed in Sn source/Nb_3Sn/Nb diffusion reaction couples. Finally, in chapter 5, it is demonstrated that the subelement structures can be carefully modified to enable the internal oxidation of Nb-Zr alloy, so

that fine ZrO_2 precipitates are formed in Nb_3Sn; these ZrO_2 particles can significantly refine Nb_3Sn grain size and improve the high-field J_c.

Dedication

This document is dedicated to my family.

Acknowledgments

First, I want to thank Prof. Sumption for his guidance, his patience, and particularly room he gave me allowing me to work on topics and projects that I believed to be promising. I want to thank Dr. Xuan Peng and Hyper Tech Research Inc. for their help in strand fabrication; without their help, many studies would just remain in the "idea" stage. I would also like to thank Drs. Collings and Majoros for their help from time to time. I want to thank my colleagues in this group, with whom the countless discussions really benefitted me a lot: Mike Susner, Yuan Yang, Chris Kovacs, Yi Ding, Guangze Li, Hyun-Sung Kim, Fang Wan, and Xiong Li. I want to thank the committee members of my dissertation, Prof. Akbar and Prof. Fraser for their advice. Finally, many thanks should be given to the United States Department of Energy, Office of High Energy Physics for their financial support.

Vita

Nov. 1988.....Born in China

June. 2009 .....B.S. in Materials Science and Engineering
Harbin Institute of Technology, China

Feb. 2011 to present .....Graduate Research Associate, Department of Materials Science and Engineering, The Ohio State University

Publications

1. X. Xu and M. D. Sumption, "A model for the compositions of non-stoichiometric intermediate phases formed by diffusion reactions, and its application to Nb_3Sn superconductors", Sci. Rep., Sci. Rep. 6, 19096; doi: 10.1038/srep19096 (2016).

2. X. Xu, M. D. Sumption, and X. Peng, "Internally Oxidized Nb_3Sn Superconductor with Very Fine Grain Size and High Critical Current Density", Adv. Mater., 27, 1346-1350 (2015).

3. X. Xu, M. Majoros, M. D. Sumption and E. W. Collings, "Persistent-Current Magnetization of Nb_3Sn Strands and Cables: Influence of Applied Field Angle and Transport Current", IEEE Trans. Appl. Supercond., 25, 8200704 (2015).

4. X. Wang, G. Ambrosio, G. Chlachidze, E. W. Collings, D. R. Dietderich, J. DiMarco, H. Felice, A. K. Ghosh, A. Godeke, S. A. Gourlay, M. Marchevsky, S. O. Prestemon, G. Sabbi, M.

D. Sumption, G. V. Velev, X. Xu, A. V. Zlobin, "Validation of Finite-Element Models of Persistent-Current Effects in Nb_3Sn Accelerator Magnets", IEEE Trans. Appl. Supercond., 25, 4003006 (2015).

5. X. Xu, M. D. Sumption, and E. W. Collings, "Influence of Heat Treatment Temperature and Ti doping on Low Field Flux Jumping and Stability in $(Nb\text{-}Ta)_3Sn$ Strands", Supercond. Sci. Technol. 27, 095009 (2014).

6. X. Xu, M. D. Sumption, X. Peng, and E. W. Collings, "Refinement of Nb_3Sn grain size by the generation of ZrO2 precipitates in Nb3Sn wires", Appl. Phys. Lett. 104, 082602 (2014).

7. X. Xu, E. W. Collings, M. D. Sumption, C. Kovacs, and X. Peng, "The effects of Ti addition and high Cu/Sn ratio on tube type $(Nb,Ta)_3Sn$ strands, and a new type of strand designed to reduce unreacted Nb ratio", IEEE Trans. Appl. Supercond. 24, 6000904 (2013).

8. X. Xu, M. D. Sumption, and E. W. Collings, "A Model for Phase Evolution and Volume Expansion in Tube Type Nb_3Sn Conductors", Supercond. Sci. Technol. 26, 125006 (2013).

9. X. Xu, M. D. Sumption, S. Bhartiya, X. Peng, & E. W. Collings, "Critical current densities and microstructures in rod-in-tube and tube type Nb_3Sn strands – present status and prospects for improvement", Supercond. Sci. Technol. 26, 075015 (2013).

Fields of Study

Major Field: Materials Science and Engineering

Table of Contents

List of Figures

Chapter 1: Introduction and problem statement

In this chapter, following a brief introduction to superconductivity and Nb_3Sn superconductors, the factors determining the non-matrix J_c of Nb_3Sn wires will be summarized, and the microstructure factors determining these properties as well as how to optimize these microstructures by controlling the starting chemistry and fabrication process will be analyzed.

1.1. A brief introduction to superconductors

A superconductor is a material that loses electrical resistivity when cooled below a transition temperature (named the critical temperature T_c). Superconductors are classified into two types based on their behaviors in a magnetic field, as shown by Figure 1. As the applied field is small, both types of superconductors are in the perfect diamagnetic state, that is, $\boldsymbol{B}=\mu_0(\boldsymbol{M}+\boldsymbol{H})=0$, where $\boldsymbol{B}$ is the magnetic flux density with the unit of T, μ_0 is the vacuum permeability with the unit of T·m/A, $\boldsymbol{M}$ is the magnetization with the unit of A/m, and $\boldsymbol{H}$ is the applied magnetic field with the unit of A/m. However, their behaviors differ as $\mu_0 H$ is above a certain value, which is named the critical field $\mu_0 H_c$ for type I and the lower critical field $\mu_0 H_{c1}$ for type II, respectively. For type I superconductors, mainly pure metals, the superconductivity and the accompanying perfect diamagnetic state are destroyed instantaneously as $\mu_0 H$ is increased to $\mu_0 H_c$. In contrast, the

destruction of the superconductivity of a type II superconductor starts from $\mu_0 H_{c1}$ but would not finish until $\mu_0 H$ reaches the upper critical field $\mu_0 H_{c2}$. Between $\mu_0 H_{c1}$ and $\mu_0 H_{c2}$ it is at the "mixed" state because both superconducting and normal state regions are present. It should be noted here that conventionally the symbol B is often used to stand for "applied magnetic field" instead of $\mu_0 H$ (with the unit of Tesla), so in the following sections of this dissertation this convention will be followed. Thus, B_{c1} and B_{c2} will be used for the lower and upper critical fields, respectively.

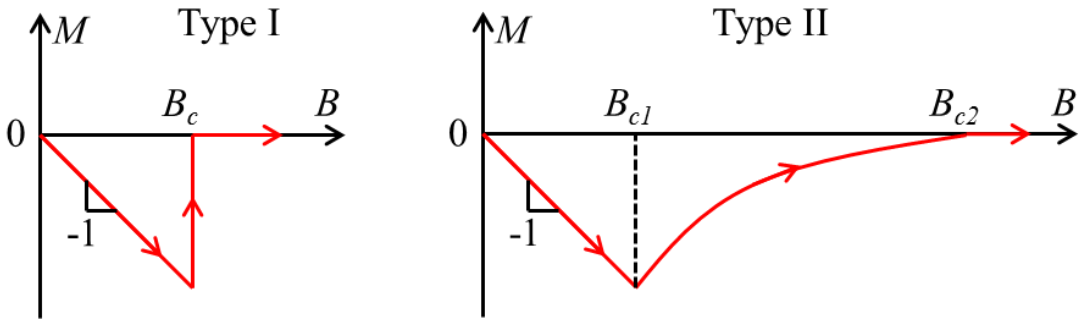

Figure 1. Schematics of ideal *M*-*B* curves for type I and type II superconductors below T_c.

Because B_{c1} is usually very small (for Nb_3Sn, this value is 0.4 T [1]), most type II superconductors work at the mixed state. For a type II superconductor in the mixed state, the magnetic flux penetrates into the superconductor body in the form of discrete quanta named fluxons, as shown in Figure 2 [2]. The magnetic flux of a fluxon is $\Phi_0 = 2.07 \times 10^{-15}$ $T \cdot m^2$. A fluxon is comprised of two regions: a normal state core and a shielding supercurrent circulating area, the radii of which equal to the coherence length ξ and penetration depth λ, respectively. Both parameters are characteristics of a superconductor,

and also depend on temperature, alloying, etc. Fluxons with the same direction of magnetic flux have repulsive interactions.

In a perfect-crystal superconductor that has no crystal defects, fluxons distribute evenly and are arranged as close-packed hexagonal lattice as a result of the repulsion forces among them. The lattice parameter of the fluxon lattice changes with applied field, and follows the relation: $a_0 = (4/3)^{1/4}(\Phi_0/B)^{1/2}$. Apparently, as B is increased, more fluxons penetrate into the superconductor, making the distance of the fluxons smaller. When B reaches the upper critical field B_{c2}, all the normal fluxon cores overlap each other, and the superconductor goes normal. The B_{c2} of a superconductor is correlated with the fluxon normal core size ξ: $B_{c2} = \Phi_0/(2\pi\xi^2)$.

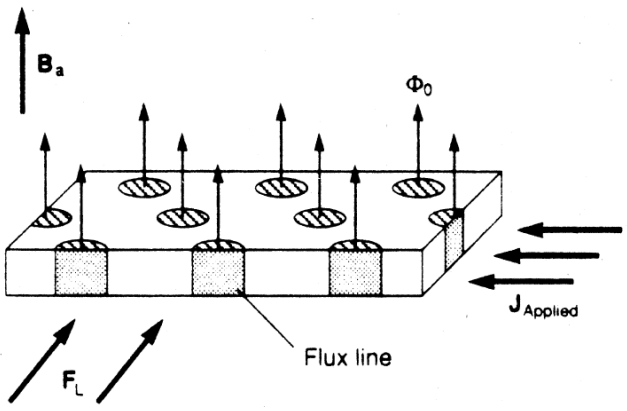

Figure 2. Schematic of a mixed-state type II superconductor as a current ***J*** passes through it [2].

When a transport current runs through a type II superconductor in the presence of an applied magnetic field, B, Lorentz forces ($\boldsymbol{F_L} = \boldsymbol{J} \times \boldsymbol{B}$, where $\boldsymbol{F_L}$ is the Lorentz force per volume in N/m^3, $\boldsymbol{J}$ is the current density in A/m^2 which is defined as current per cross-

section area) would be generated and exerted on these fluxons. The fluxon lines and $\boldsymbol{F_L}$ of a bulk superconductor are schematically shown in Figure 2. In ideal crystals fluxons would move under $\boldsymbol{F_L}$. According to the Faraday's law, an electric field $\boldsymbol{E}=\boldsymbol{v}\times\boldsymbol{B}$ (where $\boldsymbol{v}$ is the velocity of the fluxons) would be generated once fluxons begin to move, resulting in a unit-volume power dissipation of $\boldsymbol{J}\cdot\boldsymbol{E}$. In this case the material cannot maintain its superconductivity.

For non-ideal superconductors, however, the presence of crystal defects (such as vacancies, dislocations, grain boundaries, precipitates) leads to a different distribution of fluxons. These defects could "pin" the fluxons from moving unless the current density J is large enough so that $F_L=J\cdot B$ (assuming $\boldsymbol{J}$ and $\boldsymbol{B}$ are perpendicular) surpasses the pinning forces per volume, F_p that these crystal defects can provide. At a certain applied field B, the current density that causes the Lorentz forces to depin the fluxons is named critical current density J_c. Apparently, as J is below J_c, the fluxons are pinned to their positions so that the superconducting matrix can provide unobstructed paths for supercurrents flowing; as J is above J_c, however, fluxons would drift under F_L, and the accompanying resistance would make the material non-superconducting. Thus, J_c at a certain field B is determined by the bulk pinning force (F_p) that these defects can provide at this field to balance the F_L, i.e., $J_c = F_p/B$. Therefore, the primary approach to improving J_c is to enhance the F_p. One way to do this is to increase the density and strength of the pinning centers.

From the above discussions, it can be seen that the state of a type II superconductor is determined by three parameters: the temperature T, the magnetic field B, and the

current density J; each has its individual critical value: the critical temperature T_c, the upper critical field B_{c2} and the critical current density J_c, respectively. However, the three parameters are not independent. For instance, B_{c2} decreases with T, and J_c decreases as T or B increases. There is a boundary surface defined by these three parameters, as shown in Figure 3. Only if temperature, magnetic field, and current density of a material all fall below its critical surface, can this material maintain its superconductivity.

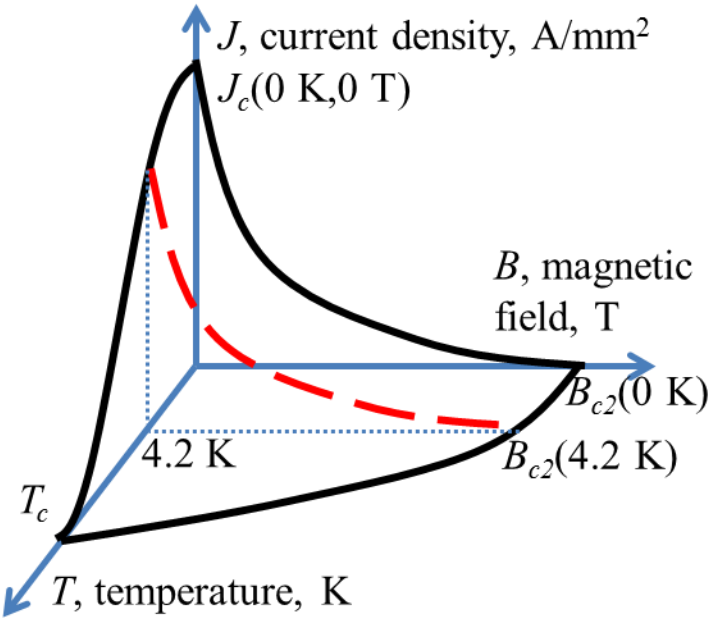

Figure 3. The critical surface of a type II superconductor. The red dashed line shows the J_c-B curve at 4.2 K.

The T_c and B_{c2} are intrinsic properties of a superconductor, and can vary with its stoichiometry, doping, and strain state. Generally, each superconductor has a maximum T_c (e.g., 18.3 K for Nb_3Sn), and this value can hardly be considerably improved. The B_{c2}

of a superconductor can usually be controlled within some range by doping, which changes its coherence length. On the other hand, J_c is an extrinsic property and also depends on crystal defects, and this is why it is possible to improve J_c by engineering the microstructure via control of the chemistry/processing. The goal of this work is mainly to improve the high-field J_c of Nb_3Sn wires at 4.2 K, the boiling temperature of liquid He.

1.2. A brief introduction to Nb_3Sn superconductor

Nb_3Sn belongs to the $Pm\bar{3}n$ space group and has a cubic A15 crystal structure, as shown in Figure 4. In each unit cell Sn atoms are seated on the corners and the body center, while on each face two Nb atoms are seated, forming three orthogonal Nb chains. The lattice constant of stoichiometric Nb_3Sn is around 0.529 nm. It is interesting to note that the Nb-Nb atomic spacing in the three orthogonal chains is 0.265 nm, smaller than the Nb-Nb spacing in pure Nb (0.286 nm). This is argued to be the cause of the high T_c of Nb_3Sn relative to that of Nb, 9.2 K [1].

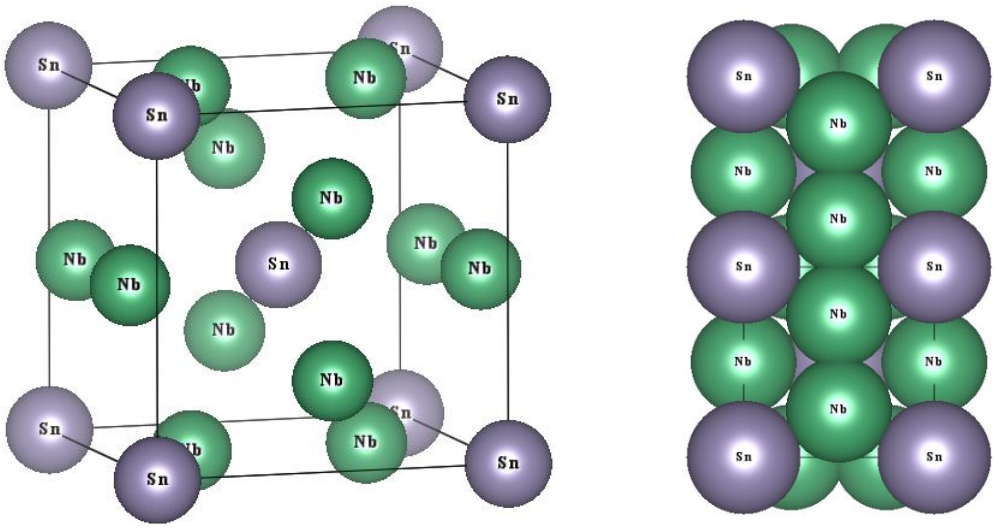

Figure 4. Schematic illustration of a unit cell of Nb_3Sn lattice.

The most widely-accepted binary Nb-Sn phase diagram above 0 °C is shown in Figure 5 (a) [3]. According to this diagram, Nb and Sn can form three intermetallic compounds, $NbSn_2$, Nb_6Sn_5 and Nb_3Sn. Since the T_cs of Nb_6Sn_5 and $NbSn_2$ are both below 2 K [1], they are not practical superconducting phases. In a binary Nb-Sn diffusion reaction couple, when heat treated below 845 °C, they first form $NbSn_2$, which later transforms to Nb_6Sn_5, and then to Nb_3Sn if Nb is in excess. It was found that Cu can destabilize $NbSn_2$ and Nb_6Sn_5 phases, and thus benefit the formation of Nb_3Sn [4]. Moreover, it is evident from this phase diagram that Nb_3Sn is not a line compound. Instead, the Sn content varies from ~17% to 26%. Atomic calculations show that Nb-on-Sn antisite defects are the main cause of the sub-stoichiometry [5].

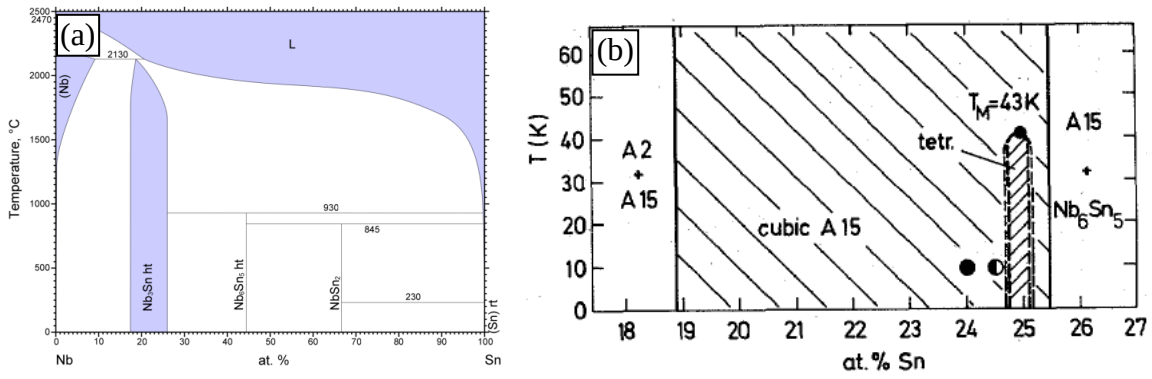

Figure 5. The phase diagrams of Nb-Sn (a) above 0 °C [4] and (b) at cryogenic temperatures [6].

It was first discovered by Mailfert *et al.* [6] that Nb_3Sn alloys in the composition range of 24.6-25.2 Sn at.% would undergo a transformation in the crystal structure below 43 K, from cubic to tetragonal, as shown by the low temperature Nb-Sn phase diagram in Figure 5 (b). This martensitic transformation is believed to have significant influence on the vaiation of B_{c2} with the Sn content of Nb_3Sn phase, as will be discussed later.

NbTi has been the dominant superconductor for magnets applications. However, its low B_{c2} (~15 T at 0 K) limits its application range below 10 T. On the other hand, Nb_3Sn conductors, with a B_{c2} (0 K) of 31 T (while 35 T was also reported [7,8]), are able to extend the application range to higher fields (12-25 T). The relatively easy fabrication processes and low cost, compared with its counterparts such as Nb_3Al, Bi:2212, and $YBa_2Cu_3O_{7-x}$ superconductors, make Nb_3Sn strands the conductor of choice in the field of 12-20 T.

Specifically, Nb_3Sn conductors have significant application potentials in the following areas: the central solenoid (CS) and the toroidal field (TF) coils in tokamak

fusion devices (such as International Thermonuclear Experimental Reactor, ITER), dipole and quardrupole magnets in high energy physics (HEP), magnetic resonance imaging (MRI), nuclear magnetic resonance (NMR), and research used high-field magnets including hybrid magnets.

For these applications, Nb_3Sn conductors must have the following characteristics. First, Nb_3Sn is used in the form of round wire, in order to facilitate cabling, because the generation of a high magnetic field requires a large current (tens of kA) that can only be supplied by many wires in parallel. Conductors with shapes of large aspect ratios (e.g., tapes) are difficult to wind into cables, and thus are inconvenient for magnet usage. This is why although Nb_3Sn tapes were used in 1960s, they were quickly replaced by wires after the early 1970s, when the invention of a bronze-process method enabled Nb_3Sn conductors to be fabricated as round wires [9].

Second, a Nb_3Sn wire should be comprised of not only Nb_3Sn phase, but also matrix material which is usually Cu, as a protection of the conductor for two purposes. First, as some local Nb_3Sn segments temporarily lose their superconductivity for some reason (e.g., heat pulse induced by mechanical movement under Lorentz force) and turn to the normal state, which has very high electric resistivity, the Cu matrix can provide a bypath for electric current, which significantly reduces the joule heating. Second, the Cu matrix plays a critical role in maintaining the temperature equality between the superconductor and the outside cold environment (e.g., helium pool): once heat is generated in the superconductor, it can be quickly conducted away via the Cu matrix, which is a superior thermal conductor. This is very important because at low temperatures Nb_3Sn has

extremely low heat capacity, so any heat generated in the superconductor will cause very large temperature rise, possibly causing the temperature of Nb_3Sn to surpass its T_c. Since normal state Nb_3Sn has high electrical resistivity, which causes more heat, in this case the normal zone would propagate, following the loop "heat → temperature rise → loss in superconductivity → high electric resistivity → heat" [10]. The presence of a matrix with good thermal conductivity can conduct the heat away, preventing the occurrence of such an avalanche. Thus, it is important to maintain the high purity of the Cu matrix to guarantee its good thermal conductivity. A parameter characterizing the thermal conductivity at cryogenic temperature is the residue resistivity ratio (RRR), which is defined for Nb_3Sn strands as the electric resistivity at 273 K over that at 20 K, considering that the thermal conductivity is proportional to the electrical conductivity according to the Wiedemann–Franz law. A low RRR value indicates the pollution of the Cu matrix, which markedly reduces its thermal conductivity and electromagnetic stability of the conductor. To protect the purity of the Cu matrix, sufficient barrier materials (e.g., Nb or Ta) are usually used to separate the Nb_3Sn and the Cu matrix; otherwise, after a certain reaction time Sn may diffuse into the Cu matrix and form Cu-Sn alloy with reduced RRR.

Third, the size of each superconducting unit (named "subelement") should be minimized, considering that Nb_3Sn itself is a bad thermal conductor, so a large subelement size may cause an adiabatic situation. Apparently, to reduce subelement size, a large-diameter Nb_3Sn wire should be comprised of a plurality of fine Nb_3Sn subelements which are embedded and distributed uniformly in the Cu matrix. It has been

well established that the instabilities of Nb_3Sn conductors include current distribution effects either from transport current redistribution of magnetization [11], or from self-field effects [12-14]. The instabilities coming from the magnetization component are tied to the effective subelement diameter d_{eff} (which is more or less equal to the subelement diameter d_{sub} for a fully-reacted high-J_c Nb_3Sn strand), while those from the self-field component depend on strand diameter, and both can be partially suppressed by some level of dynamic stabilization, which requires a high RRR value. A series of studies carried out at Fermi National Accelerator Lab (e.g. [15, 16]) and Brookhaven National Lab (e.g. [17, 18]) demonstrated the importance of reducing d_{eff} and improving RRR, respectively, for improving low-field stability. The magnetization of a superconductor is proportional to the product of J_c and d_{eff}. Reducing the magnetization not only helps to improve the stability, but also benefits reducing the persistent-current magnetization induced magnetic field errors in magnets. In 1999 the U.S. Conductor Development Program (CDP) set the target parameters for the Nb_3Sn conductors for HEP application, which include but not limited to a 12 T non-matrix J_c of > 3000 A/mm^2 and d_{eff} of < 40 μm [19]. In order to reduce subelement size without decreasing the superconducting area fraction, one can either increase the subelement count in a strand or decrease the strand diameter. For example, a typical strand structure of modern design is 0.7-0.8 mm diameter with 217 subelements embedded in the Cu matrix, which gives a subelement size of ~40 μm [20]. To obtain such small size, many courses of deformations like extrusion and drawing to the starting billet/restack are performed before reaching the final size.

Fourth, because Nb_3Sn phase is a brittle intermetallic compound, all the deformation process must be done before Nb_3Sn phase is formed. Thus, a wire usually starts with a stack composed of precursors including ductile Sn, Cu, and Nb metals or alloys (e.g., Nb-7.5 wt.%Ta), which is processed into the final size by multiple courses of extrusion and drawing. Then the final-size, green-state wires are winded to cables or coils, and finally, heat treatments are applied to transform the precursors to Nb_3Sn phase. To guarantee that the subelements can be processed down to fine sizes, the precursors must be ductile.

At present there are several types of Nb_3Sn strands based on the architecture of the precursors. Generally, they can be classified to two categories: one type has low J_c (generally <1000 A/mm^2 for the 4.2 K, 12 T non-matrix J_c) but very small filament size (typically ≤ 6 μm); the other type has high J_c (above 2000 A/mm^2 for the 4.2 K, 12 T non-matrix J_c) but large subelement size (typically >35 μm, although as small as 12 μm is achievable in one type of the strands [20]). It is worth mentioning that for all present Nb_3Sn strands, due to its function of destabilizing the high-Sn Nb_6Sn_5 and $NbSn_2$ phases and thus encouraging the formation of Nb_3Sn, Cu is used as an indispensable element in the subelements. Microanalysis shows that Cu mainly segregates in Nb_3Sn grain boundaries instead of dissolving in Nb_3Sn lattice [21]. The low-J_c and low-d_{eff} type includes bronze-process strands and single-barrier internal-tin strands with high Cu/Nb ratio in each subelement. In these strands, after heat treatment the Nb_3Sn filaments are well separated by the bronze. This type of strands are mainly targeted for the application in fusion devices, where the fast current ramp rates place a high requirement of low a.c. losses. The high-J_c type includes distributed-barrier internal-tin (also named rod-restack-

process, RRP, or rod-in-tube, RIT) with very low Cu/Nb ratio in each subelement, powder-in-tube (PIT), and tube type strands. These high-J_c Nb_3Sn strands are mainly targeted for high energy physics (HEP) applications.

Bronze process takes advantage of Cu-Sn bronze alloy as the Sn source [9]. A certain number of Nb rods are inserted into the axially gun-drilled holes in the bronze billet, and then the composite is wrapped with a tantalum foil and inserted to a Cu can, and the stacking together is drawn down to the final size. The Ta layer serves as a barrier against Sn leakage into the outside Cu matrix during heat treatment. Each Nb alloy rod in the green state transforms to a Nb_3Sn filament after heat treatment, leading to small filament size (several microns) and thus good stability and low a.c. loss. The drawback of the bronze-process strand is that the solubility of Sn in bronze is limited, which leads to formation of Nb_3Sn phase with low quality, which will be discussed later.

To overcome this disadvantage, the single-barrier internal-Sn strands use pure Sn (or Sn-Ti alloy) instead of bronze as the Sn source, and the Nb rods are inserted to axial holes of a Cu billet, BSE image of which shown in Figure 6 (a). During heat treatment Cu and Sn first mix and form Cu-Sn alloy before reacting with Nb to form Nb_3Sn phase. Similar to bronze process strands, the Nb_3Sn filaments are well separated by bronze after heat treatment, leading to very small filament size. In this structure the Sn content of the Cu-Sn alloy can be controlled via the size of the Sn alloy rod in each bundle.

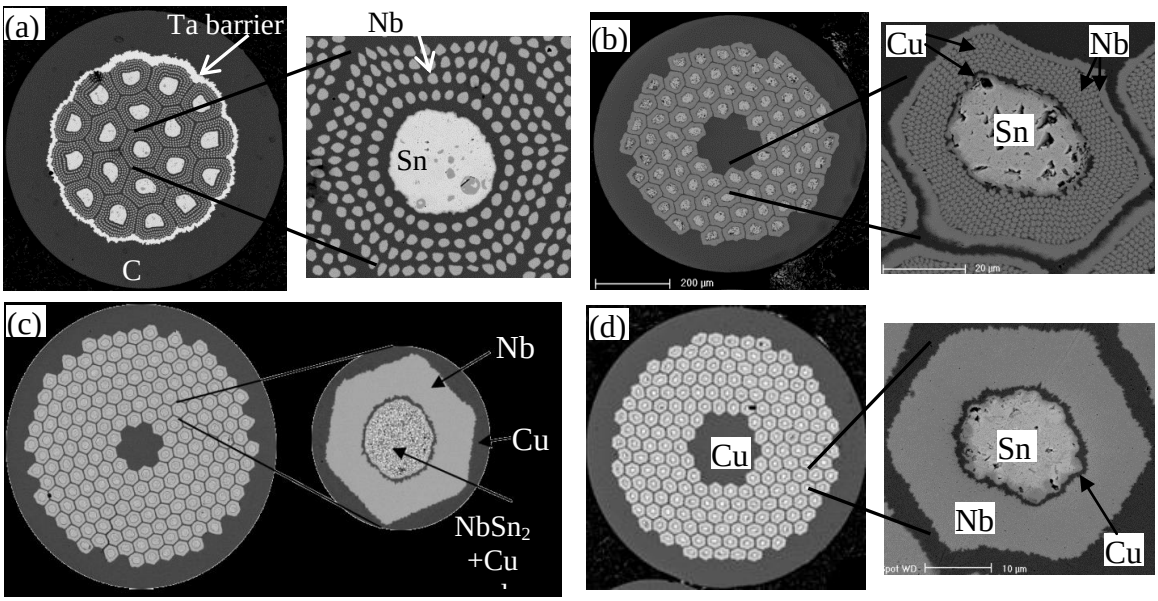

Figure 6. BSE/SEM images of cross sections of (a) single-barrier internal-tin, (b) RIT, (c) PIT [25] and (d) tube type Nb_3Sn strands.

Distributed-barrier internal-tin (also named RRP or RIT) strands, the variance of the above single-barrier internal-Sn strands, use a stacking of Cu-encased Nb rods instead of a Cu billet with Nb rods in axial holes to compose a subelement [22] (SEM images of cross sections of a RRP strand are shown in Figure 6 b), and since the Cu jacket of each Nb rod can be very thin, the overall Cu/Nb ratio in each subelement can be much lower. Another difference between RRP strands and the internal-tin strands for fusion reactors is the barrier materials. In the high Cu/Nb ratio internal-tin strands there is only one master Ta barrier in each strand to prevent the inner bronze releasing Sn to the outside Cu matrix. However, in RRP strands, each subelement has a barrier, and the barrier material is usually Nb so that part of it can transform to Nb_3Sn to maximize the Nb_3Sn fraction, and after reaction each subelement becomes a current-carrying unit embedded in the Cu

matrix. In contrary to the single-barrier internal-Sn strands used for fusion reactors, the much lower Cu/Nb ratio in RRP strands leads to not only higher Nb_3Sn area fractions, but also improved Nb_3Sn quality, both factors significantly benefiting high-field non-barrier J_c of RRP strands, which will be discussed later. Presently RRP strands keep the record non-matrix J_c (~3000 A/mm^2 at 4.2 K, 12 T) among present Nb_3Sn strands. However, one drawback of RRP strands is that after reaction all the Nb filaments in each subelement merge and form a single Nb_3Sn annulus; this leads to a large subelement size, which is adverse to the stability and a.c. losses properties. Because of bonding issues [23] and metalworking difficulty due to Nb/Cu microcomposite hardening [24], it is difficult to reduce the subelement size of such strands to below 40 μm.

Tubular (PIT and tube type) strands (SEM images shown in Figure 6 c [25] and d, respectively), which use a single Nb tube instead of a stacking of hundreds of Cu-encased Nb rods to compose a subelement, are promising to get even smaller subelement size. At present, Hyper Tech Research Inc. (HTR) has successfully produced 1387-subelement tube type strands at 0.7 mm diameter, reducing the subelement diameter to 12 μm [20]. The difference between PIT and tube type strands is that PIT strands use $NbSn_2$+Cu [26] (or Nb_6Sn_5+Cu [27], or Cu_5Sn_4 [28]) powders as the Sn core, whereas tube type strands simply use a Cu jacketed Sn rod. Similar to single-barrier and distributed-barrier internal-tin strands, Cu and Sn mixes before reacting with Nb to form Nb_3Sn. Apparently PIT strands are more expensive because very fine powders are required to ensure a good drawability.

1.3. What determines $J_c(B)$ of Nb_3Sn and how to improve it?

There are three types of critical current density J_c, depending on which areas the critical current I_c is normalized to. The whole-wire J_c (or, engineering J_c) is defined as the critical current over the whole strand cross section area, while the non-matrix J_c is I_c over the sum of the subelement areas (i.e., the whole strand area minus the Cu matrix area), and the layer J_c is I_c over the superconducting Nb_3Sn area that carries the super current. Usually the engineering J_c is the one most closely related to practical applications, but the non-matrix J_c is the most commonly used index of the performance of a strand, while the layer J_c directly reflects the quality of the superconducting Nb_3Sn phase. The non-matrix J_c equals to the product of the supercurrent-carrying Nb_3Sn area fraction in the subelement and the layer J_c that the Nb_3Sn layer carries. At present, the highest 4.2 K, 12 T Nb_3Sn-layer J_cs of ~5000 A/mm^2 is achieved simultaneously in optimized RRP, PIT, and tube type strands [24,29]. However, different current-carrying Nb_3Sn area fractions in these strands lead to different non-matrix J_cs. This will be further discussed in section 3.1.

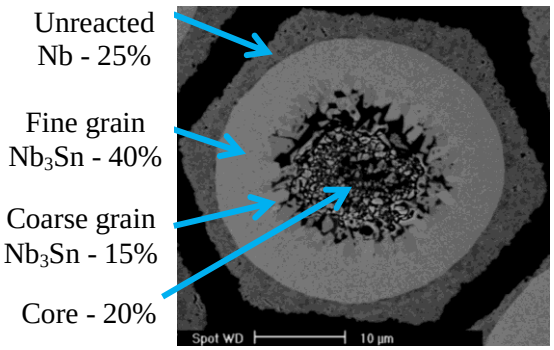

Figure 7. BSE image of a fully-reacted tube type subelement with the fractions of each component.

First, let us look at what determines the Nb_3Sn area fraction in a subelement. Figure 7 shows BSE image of a typical tube type subelement after being fully reacted. As can be seen, such a subelement is comprised of four components: the unreacted (or remaining) Nb area which serves as a barrier against Sn leakage into the outside Cu matrix and takes about 25 % of the subelement, the fine-grain Nb_3Sn area which has grain size of 100-200 nm and takes about 40 % of the subelement, the coarse-grain Nb_3Sn area which has large grain size (typically > 1 μm) and takes about 15 %, and finally a core region which is composed of low-Sn Cu-Sn alloy, Kirkendall voids, and some disconnected Nb_3Sn particles, and takes about 20 % of the subelement area. It is worth mentioning that the coarse-grain Nb_3Sn and the Nb_3Sn particles in the core are formed by the dissociation of the intermediate Nb_6Sn_5 phase, and do not carry supercurrent, while the fine-grain Nb_3Sn, which is formed by diffusion reaction between Sn and Nb, is the only supercurrent-carrying phase in a subelement. Thus, the non-matrix J_c equals to the product of the FG layer J_c and this fraction (i.e., 40 % in Figure 7). At present, the highest fine-grain Nb_3Sn fraction (~60 %) is achieved in RRP strands [24]. The prospects of improving this

fraction will be discussed in chapter 3, and next let us see what determines the layer J_c of a Nb_3Sn strand.

From Figure 3 it is clear that J_c decreases monotonically with increasing B, reaching zero at B_{c2}. Here it must be pointed out that Nb_3Sn superconductors are always found to lose the capacity to carry supercurrent at a field that is smaller than B_{c2}. This field is named the irreversibility field, B_{irr}, which is usually $0.8\sim0.9B_{c2}$ for Nb_3Sn. The difference between B_{irr} and B_{c2} in Nb_3Sn was first noticed by Suenaga [30], who attributed it to the threshold of thermally activated flux line jumping, like in high temperature superconductors. However, it was later found that in wire samples the difference between B_{irr} and B_{c2} is mostly enlarged by the inhomogeneity of the Nb_3Sn layer [1, 31]. In the following discussions the B_{irr} will be used as the field at which J_c vanishes.

As discussed in section 1.1, at a certain field B the critical current density J_c is determined by the highest bulk pinning force that pinning centers can supply at this field according to the relation $F_p=J_c \times B$. The bulk pinning force F_p is a function of B, and the curve $F_p(B)$ has the following characteristics: at zero field, F_p and F_L are zero because there are no fluxons in the superconductor body yet; at low fields, the density of fluxons is low, so only a small fraction of pinning centers interact with fluxons, so bulk pinning force per volume, F_p, is low; as B reaches B_{irr}, F_p and F_L again vanish because the critical current is zero. Therefore, there must be a peak at a certain intermediate field, at which the pinning sites work most effectively.

In history there have been many models trying to quantify the $F_p(B)$ relations of Nb_3Sn, of which the most widely accepted one was proposed by Kramer [32]. According to this model, at high fields the pinning force is given as

$$F_p = 3.494 F_{p,\max} b^{1/2} (1-b)^2 \tag{1.1}$$

where $b=B/B_{irr}$, and $F_{p,max}$ is the maximum pinning force in N/m^3, which depends on microstructure, temperature, and B_{irr}. From equation (1.1), it is clear that $F_p(B)$ curve peaks at b=0.2, i.e., $F_p(0.2B_{irr})= F_{p,max}$.

The typical normalized $F_p(B)$ curve for Nb_3Sn is shown by the black solid curve in Figure 8, along with the curves assuming B_{irr} or $F_{p,max}$ is improved by 20% while the other is kept constant, respectively. It is very clear that improvements in B_{irr} and $F_{p,max}$ can both lead to improvements of F_p and thus J_c in the high field range (> $0.3B_{irr}$) where Nb_3Sn superconductors are used.

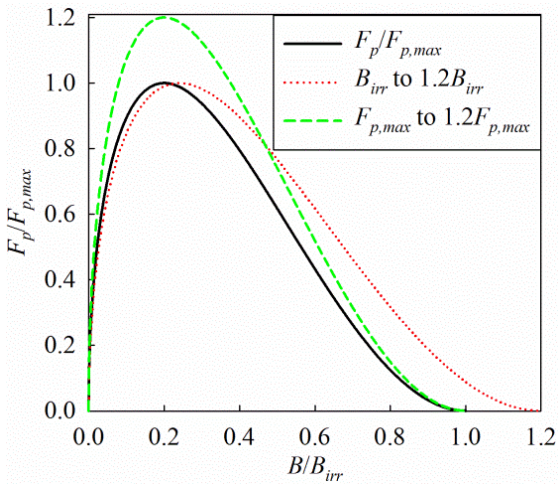

Figure 8. The sketch of $F_p(B)$ curves for Nb_3Sn: the black solid curve stands for a standard normalized $F_p(B)$ curve; the red dotted and the green dashed curves stand for $F_p(B)$ with B_{irr} and $F_{p,max}$ improved by 20%, respectively.

Herein, according to Kramer's model, a $J_c(B)$ curve is determined if the two parameters, $F_{p,max}$ and B_{irr}, are fixed. By inserting $F_p = J_c \times B$ and $b = B/B_{irr}$ into the equation (1.1) and rearranging it, an equivalent expression to equation (1.1) can be obtained:

$$J_c^{1/2} B^{1/4} = a + kB \tag{1.2}$$

where a and k are parameters depending on B_{irr} and $F_{p,max}$. It should be noted that equation (1.2) assumes that Nb_3Sn grain size is far larger than flux line spacing, which is true for present commercial Nb_3Sn strands. The case where grain size becomes comparable to the flux line spacing will be discussed in chapter 5. Other cases where Kramer plots are not linear for present strands are occasionally reported and modifications to Kramer's model have been suggested [33,34]; however, majority of present Nb_3Sn strands follow Kramer's model very well. Thus, by finding out the a and k values by fitting the Kramer plots ($J_c^{1/2}B^{1/4}$ vs B) using equation 1.2, B_{irr} and $F_{p,max}$ values can be calculated:

$$B_{irr,K} = -a/k \quad , \quad F_{p,\max} = \left[a^{2.5} / (-k)^{0.5} \right] / 3.494 \tag{1.3}$$

where $B_{irr,K}$ denotes the irreversibility field derived from Kramer's plot.

As discussed above, the way to enhance layer J_c of Nb_3Sn superconductors is to improve $F_{p,max}$ and B_{irr}. The next two sections will discuss what determines these two factors and how to improve them.

1.4. What determines $F_{p,max}$ in Nb_3Sn and how to improve it?

Kramer's derivations also give the expression of $F_{p,max}$ [32]:

$$F_{p,max} = C_s B_{c2}^{2.5} / \kappa_1^2 \tag{1.4}$$

where C_s is a microstructure (e.g., density of flux line pinning centers) dependent parameter, and κ_1 is the Ginzburg-Landau parameter. From equation 1.4, it is clear that the two factors influencing the $F_{p,max}$ of Nb_3Sn phase are its superconducting properties (B_{c2} and κ_1) and its microstructure, which is self-evident because greater densities of flux line pinning centers certainly lead to higher pinning force per volume. What determines the superconducting properties of Nb_3Sn will be discussed in section 1.5 and chapter 4, now let us see how the microstructural factors influence the $F_{p,max}$.

After Kunzler *et al*. [35] discovered in 1961 the capacity of Nb_3Sn superconductor to carry large current density at high fields, intensive researches were carried out in the 1960s and 1970s in search of the microstructure factors influencing F_p. These studies, first based on tapes and then on bronze-process Nb_3Sn wires, led to the discovery that the major flux-line pinning centers in Nb_3Sn are grain boundaries [36,37]. The results by Scanlan *et al.* [36] showed that $F_{p,max}$ was improved by a factor of 8 as the grain size d was refined from 530 nm to 80 nm.

It was also found that $F_{p,max}$ may depend not only on grain size, but also on grain morphology. It was reported in [38] that columnar grains in bronze-process wires have lower pinning efficiency than equaixed grains in high-J_c type wires. Study [39], in which

the change of $F_{p,max}$ with grain size in RIT strands was studied by varying the reaction temperature and time in a wide range, also confirmed this conclusion. It was shown that $F_{p,max}$ increases linearly with the reciprocal of grain size, $1/d$, as the grain size is larger than 120 nm, but the $F_{p,max}(1/d)$ curve bends over as the grain size is smaller than 100 nm, as shown in Figure 9. The author noted that the sub-100 nm grains, which were obtained on strands reacted at 615 °C, had relatively large aspect ratios; herein, the authors concluded that the transition of the $F_{p,max}(1/d)$ curve could be because the grain boundaries of the columnar grains are mainly low-angle grain boundaries, which are less efficient pinning centers than boundaries of equaixed grains. On the other hand, the low B_{c2}s of the strands reacted at 615 °C may also contribute to their low $F_{p,max}$, because $F_{p,max}$ also depends on the superconducting properties of Nb_3Sn, according to equation 1.4.

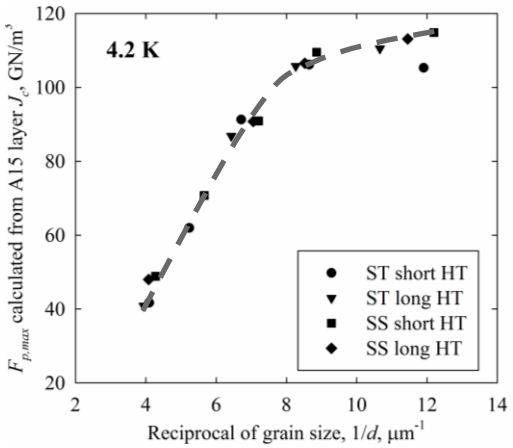

Figure 9. The variation of $F_{p,max}$ with grain size for RIT strands [39].

It was found that the Nb-Sn reaction temperature (i.e., the Nb_3Sn formation temperature) and heat treatment time are the two most important determinants of Nb_3Sn grain size. The influence of heat treatment on Nb_3Sn grain size was systematically investigated by Schelb [40] in 1981. In this work bronze-process Nb_3Sn strands were systematically heat treated at various temperatures and for various durations at each temperature. It was found that the grain size d depended strongly on reaction temperature T_R but mildly on reaction time t_R. While d increased with T_R exponentially, it increased with t_R at the first stage and then eventually plateaued. Therefore, to achieve fine grain size for the goal of high $F_{p,max}$, Nb_3Sn strands should be heat treated at low temperatures (usually below 675 °C). The variations of average grain sizes with heat treatment temperature in paper [39] are shown in Figure 10, indicating that Ti doping enhanced grain growth by decreasing the activation energy.

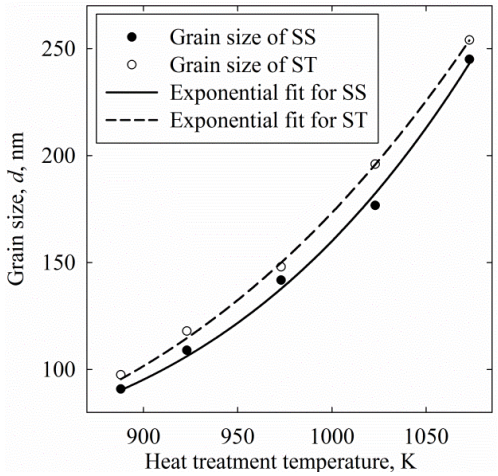

Figure 10. The dependence of grain size on reaction temperature for SS (Nb_3Sn with Ta addition) and ST (Nb_3Sn with both Ta and Ti additions) RIT strands [39].

At present most Nb_3Sn wires are heat treated at 615-700 $^{\circ}$C, with the typical average grain size around 100-200 nm. It is unlikely to markedly refine the grain size by further reducing the reaction temperature. Thus, using alternative approaches, mainly introducing second phase additions [41], to improve the pinning capacity has attracted more and more attentions in recent years. It is worth pointing out that second phase additions to Nb_3Sn wires can be classified into two categories. One type serves directly as artificial pinning centers (APC) for flux lines, and improves the pinning capacity of the superconductor. The other type of second phase additions (e.g., fine particles distributed at Nb_3Sn grain boundaries) may not remarkably improve the $F_{p,max}$ by themselves, but they can refine Nb_3Sn grain size, while the refined grain size leads to enhanced pinning capacity [42]. The usage of second phase particles to refine Nb_3Sn grain size will be discussed in chapter 4. Here an example of APCs intended to directly pin flux lines is introduced.

The approach of introducing nanometer Cu APCs into Nb_3Sn strands was investigated by Zhou [43] and Rodrigues et al. [44]. In this method, filaments comprised of thin Cu ribbons (with thickness of 20~40 nm) sandwiched between Nb tapes (with thickness of 30~100 nm) are produced by successive steps of bundling and mechanical deformation of the Cu-Nb composites. These non-superconducting Cu ribbons (which would transform to Cu-Sn during the reaction stage) are expected to serve as APCs impeding the flux lines motion. Rodrigues et al. reported that by optimizing the heat treatment schedule of these new conductors, a shift of the peak of the $F_p(B)$ curve to higher field was achieved [44]. They reported that for some of their strands the field of $F_{p,max}$ was shifted to half of the B_{irr}, the same behavior with Nb-Ti conductors. However,

the J_cs of the conductors reported were low. Besides, from the SEM images they provided, it is clear that Cu ribbons had agglomerated into isolated large-size Cu (or Cu-Sn) islands after heat treatments. Since the boundaries of these Cu islands coincide with the A15 grain boundaries, it is interesting to ask that the Cu APCs could lead to significant improvement in pinning capacities. Therefore, the effectiveness of this approach needs further investigation.

1.5. What determines B_{c2} of Nb_3Sn and how to improve them?

Before getting into the discussion of the factors determining B_{c2} of Nb_3Sn strands, it is worth pointing out the origin of the difference between the B_{c2} and B_{irr} values. Since the Nb_3Sn phase in Nb_3Sn strands is formed via solid state diffusion reaction, there is an inevitable Sn content gradient across the formed Nb_3Sn layer [31]. As will be seen later, Sn content influences B_{c2} of Nb_3Sn significantly. Thus, the Nb_3Sn layer in a subelement can be regarded as being composed of many layers with different B_{c2} and J_c values. Because the Sn content gradient in the Nb_3Sn layer in a subelement is in the radius direction, these layers are current paths in parallel. Figure 11 (a) shows a schematic of a Nb_3Sn layer that is composed of two parallel Nb_3Sn layers with different B_{c2} values, 20 T and 25 T at 4.2 K. Here we assume that the grain sizes of the two layers are the same (which is typically true for high-J_c strands), and the $F_{p,max}$ of the layer with a B_{c2} of 25 T is 20% higher than that of the layer with a B_{c2} of 20 T, because $F_{p,max}$ increases with B_{c2},

according to equation 1.4. Then the Kramer plots of these two layers and the bi-layer sample can be calculated, and are shown in Figure 11 (b). Apparently, as a linear fit to the Kramer plot of the whole sample at intermediate fields (8-15 T for most labs) is used to obtain the $B_{irr,K}$, the value is between the minimum and the maximum B_{c2} values. For instance, in Figure 11 (b) this $B_{irr,K}$ value is 22.8 T.

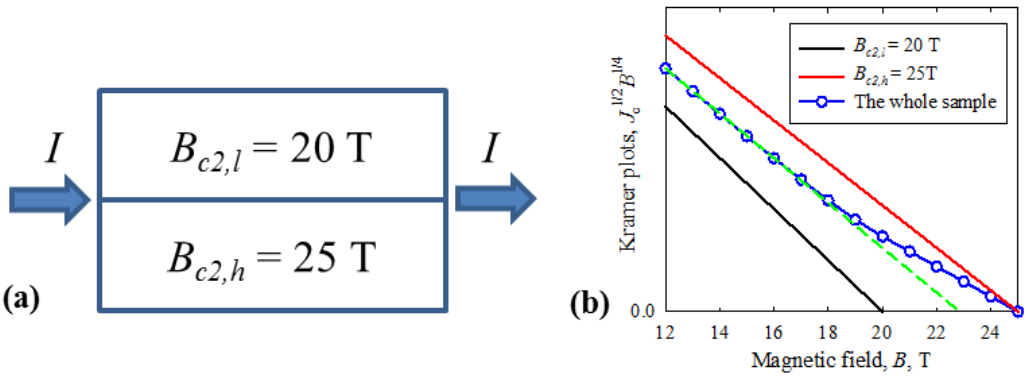

Figure 11. (a) Schematic of two Nb_3Sn layers with different B_{c2} values in parallel, and (b) Kramer plots of the three cases. The green dashed line stands for a linear fit of the $J_c^{1/2}B^{1/4}$ vs B for the whole sample at intermediate fields.

On the other hand, the most commonly used method to measure the B_{c2} of a Nb_3Sn sample is: at a certain temperature, the resistance R of a sample is measured using the four-point method with a very small sensing current (e.g., 10 mA) supplied as the magnetic field is increased, and the magnetic field where the resistivity increases from zero to a normal-state value is taken as the B_{c2}. Apparently, according to Figure 11 (b), this gives the B_{c2} of the best current path in the sample. For any inhomogeneous sample, the Kramer plots would have a tale extending to the B_{c2} of the best current path of the sample [45]. Thus, the $B_{irr,K}$ and B_{c2} values of a Nb_3Sn strand are different due to its

inhomogeneity. This is also the major origin for the difference between them. Herein, in section 1.5, we only discuss what determines B_{c2} of a homogeneous Nb_3Sn sample.

As shown in Figure 3, B_{c2} decreases with temperature. Usually it is necessary to obtain the whole $B_{c2}(T)$ superconducting phase boundary. The relation between B_{c2} and T has been studied extensively in history. The applicability of the MDG theory (named after Maki [46] and De Gennes [47]) to present Nb_3Sn superconductors in the "dirty" limit was demonstrated by Godeke [1]. Here "dirty" means in a superconductor the electron mean free path l is smaller than the coherence length ξ, while "clean" means $l \geq \xi$. A pure, stoichiometric Nb_3Sn crystal is usually in the "clean" limit. As defects such as vacancies and substitutions are introduced into the Nb_3Sn crystal, these disorders would increase electron scattering and thus decrease l, making the crystal "dirtier". Most practical Nb_3Sn samples are in the dirty limit because they are non-stoichiometric and they usually have Ta or Ti addition. According to the MDG theory [1], B_{c2} (0 K) = $-0.693T_c \cdot (\mathrm{d}B_{c2}/\mathrm{d}T)|T_c$. Thus, B_{c2} (0 K) is determined by two parameters: T_c and the slope of $B_{c2}(T)$ curve around T_c.

What essentially determines the B_{c2} of Nb_3Sn superconductors? Orlando *et al.* [48] calculated the $(\mathrm{d}B_{c2}/\mathrm{d}T)|T_c$ using the Ginzburg-Landau-Abrikosov-Gor'kov (GLAG) theory and obtained

$$-\left(\frac{\partial B_{c2}}{\partial T}\right)_{T_c} \approx C_1\gamma^2 T_c + C_2\gamma\rho_n \tag{1.5}$$

where γ is the coefficient of electronic specific heat per unit volume and has a unit of $J/(m^3 \cdot K^2)$, ρ_n is the normal state electrical resistivity with a unit of $\mu\Omega \cdot cm$ and

conventionally measured at a temperature slightly above T_c (e.g., 20 K for Nb_3Sn) to destruct the superconductivity, C_1 and C_2 are constants with approximate values of 5×10^{-8} $(m^4\cdot K^2)/(J\cdot A)$ and 5.5×10^3 K/V, respectively [48].

Plugging equation (1.5) into the MDG theory gives B_{c2} (0 K) $\propto C_1\gamma^2\cdot T_c^2 + C_2\gamma\cdot T_c\cdot\rho_n$. According to this equation, increasing ρ_n, which can be realized by introducing various disorders to Nb_3Sn, may be an effective way to improve B_{c2} (0 K) if it would not degrade T_c or γ to an extent that the increase in ρ_n cannot compensate. The variation of B_{c2} with ρ_n was investigated by Orlando *et al.* in 1981 [49]. In this work thin film samples were fabricated at various substrate temperatures to produce samples of different ρ_ns. Apart from these samples, the authors also collected a series of data from previous researches including off-stoichiometric and irradiated samples, and samples with additives. The plot showing the variation of B_{c2} with ρ_n is reprinted in Figure 12. It was claimed that as ρ_n was below 60 μΩ-cm all samples displayed a universal behavior regardless of the ways disorders were introduced, while as ρ_n was above 60 μΩ-cm, the off-stoichiometric Nb_3Sn fell off the universal behavior. As ρ_n was below 30 μΩ-cm T_c was almost independent of ρ_n, but above 30 μΩ-cm T_c dropped drastically. The slope of B_{c2} with temperature at T_c, $(dB_{c2}/dT)|T_c$, first increased and then decreased with ρ_n, peaking at ~40 μΩ-cm. The combining effect is that $B_{c2}(0)$ peaked at 20-30 μΩ-cm, reaching ~30 T. The ρ_n of a binary, stoichiometric Nb_3Sn single crystal was reported to be 4 μΩ-cm [50]. Increasing ρ_n can be realized by decreasing Sn content and/or adding dopants to Nb_3Sn lattice. The influences of Sn content and additives on the B_{c2} of Nb_3Sn phase will be discussed below.

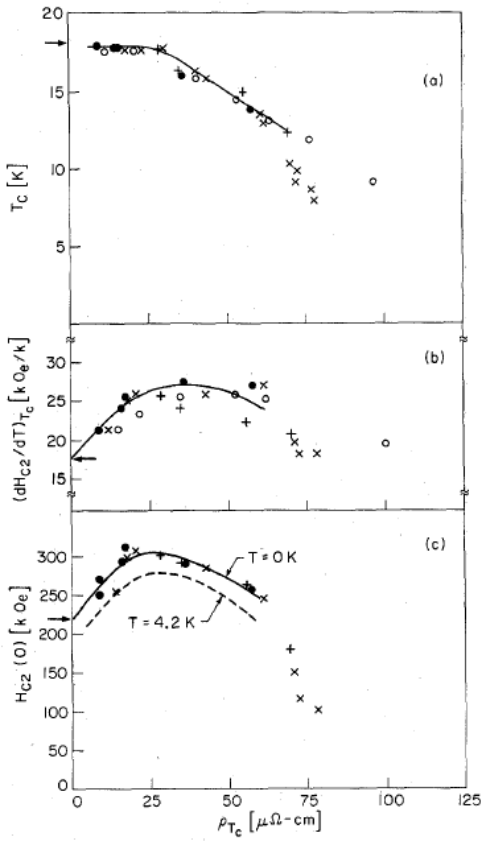

Figure 12. The variations of (a) T_c, (b) $(dB_{c2}/dT)|T_c$, and (c) upper critical field B_{c2} with normal state electrical resistivity ρ_n (at 20 K) for Nb_3Sn [49].

Apart from composition and doping that can be deliberately controlled to some extent to improve B_{c2}, the strain state of Nb_3Sn can also have significant influence on its B_{c2}. Nb_3Sn is a brittle intermetallic compound; its superconducting properties (T_c and B_{c2}) and supercurrent-carrying capability get degraded as the strain (either tensile or compressive) applied on it increases [51]. The degradation of B_{c2} with strain could be because the elastic strain causes tetragonal distortion to Nb_3Sn lattice [52]. If the strain level is low, the performance of the conductor can be recovered as the strain is released.

However, as the strain reaches some critical value, irreversible damage can occur. There are mainly two types of strains in Nb_3Sn conductors. First, thermal strain originates from the different thermal contraction coefficients of its different components as a composite conductor is cooled from its formation temperature (900-950 K) to room temperature and to the operation temperature, which is usually 1.9 or 4.2 K. For example, Cu matrix has a larger thermal contraction coefficient than Nb_3Sn [53], which causes axial compressive strain to Nb_3Sn phase during cooling down. Second, large strains can be induced by the Lorentz forces acted on Nb_3Sn cables when they are used in magnets due to the high transport current they carry and the magnetic field they are in.

According to the binary phase diagram of Nb_3Sn (Figure 4 a), the composition of Nb_3Sn phase extends from ~17 to ~26 Sn at.%. The influences of Sn content on the superconducting properties have been studied for several decades, and it has been proven that these influences are critical. Godeke [1] reviewed these studies in literature and compiled the data set into the graphs of T_c(at.% Sn) and B_{c2}(at.% Sn), which are reprinted in Figure 13 (a) and (b), respectively. It is clear that T_c increases monotonically with Sn content from 6 K at 18 at.% to 18 K at 24.5%, and then levels off. From Figure 13 (b), $B_{c2}(0)$ values increase monotonically with Sn content in the 19.5 to 24 at.% range. A linear fit was proposed in this range, resulting in a slope of ~6 T/at.% Sn. Beyond 24.5 at.%, however, $B_{c2}(0)$ drops drastically as Sn content increases.

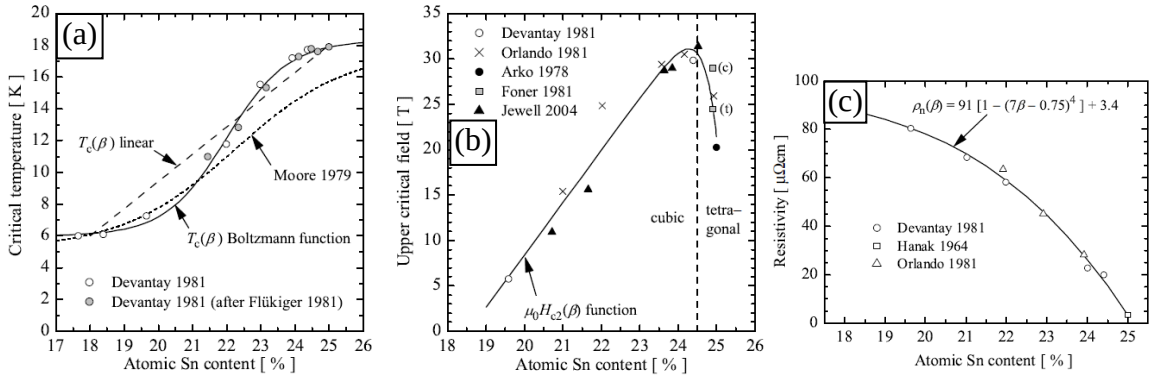

Figure 13. The changes of (a) critical temperature T_c, (b) upper critical field B_{c2}, and (c) normal state electrical resistivity ρ_n with Sn content in binary Nb_3Sn [1].

The variation of normal state electrical resistivity ρ_n with Sn content presented in [1] is reprinted in Figure 13 (c). It can be seen that ρ_n increases monotonically from 4 to 80 μΩ-cm as Sn content decreases from 25 to ~19.5 at.%. This is because the point defects (Sn vacancies and Nb-on-Sn anti-site defects) associated with the sub-stoichiometry increase electron scattering. From Figure 13 (c), ρ_n arrives at 20-30 μΩ-cm at 24-24.5 at.%, which, according to Orlando's theory, leads to the maximum B_{c2}. This perhaps explains why maximum $B_{c2}(0)$ occurs as Sn content is 24-24.5 at.% (Figure 13 b). However, there are still some debates for the cause of the sharp drop of $B_{c2}(0)$ as Sn content increases from 24.5 to 25 at.% and beyond. Some researchers believe this is due to the martensitic transformation at low temperatures [54], which is similar to the tetragonal distortion as Nb_3Sn phase is under strain [52]; while some argue that martensitic transformation in this composition range does occur at low temperatures, but such a transformation does not lead to $B_{c2}(0)$ drop [55,56], and what causes such a $B_{c2}(0)$ drop is the sharp decrease in ρ_n.

In practical Nb_3Sn strands, Sn content gradients across the Nb_3Sn layer are always present. Although most Nb_3Sn wires can have Sn contents of 24 at.% or greater in their best parts, they have different Sn content gradients across the Nb_3Sn layer: for example, the gradient can be greater than 3 at.%/μm for bronze-process wires but be less than 0.3 at.%/μm for PIT wires. Apparently, the B_{irr} values can be further improved if the Sn content of the whole Nb_3Sn layer is pushed up to 24 at.%. Practically, it is found that the Sn content of a Nb_3Sn wire is mainly influenced by its reaction temperature and time. In fact, increasing heat treatment temperature has been the primary method of improving B_{irr}. However, as discussed in section 1.4, increasing heat treatment temperature leads to increase in grain size, which undermines $F_{p,max}$, so a balance must be found for Sn content and grain size. On the other hand, reaction time plays a secondary role in influencing B_{irr}: B_{irr} first increases with reaction time and then gradually plateaus [37,57].

Numerous studies have been conducted to study the effects of third elements on Nb_3Sn. The initial purpose of introducing additives into Nb_3Sn was to improve B_{c2}, because once incorporated into the Nb_3Sn lattice, the additives, usually acting as substitutional point defects, would increase normal state electrical resistivity and thus improve B_{c2} in a certain range. Elements that cannot dissolve in Nb_3Sn but can increase the Nb_3Sn layer growth rate when added to Cu-Sn alloy (e.g., Mg [58], perhaps by enhancing the activity of Sn in Cu-Sn alloy) will not be discussed here. Since only the elements that have similar atomic size and properties (e.g., electro-negativities) can substitute Nb or Sn atom in a considerable amount, additions of elements adjacent to Nb or Sn in the periodic table were studied, including titanium [59,60], zirconium [59,60],

hafnium [59], vanadium [60], tantalum [60,61], molybdenum [60] (on the Nb side) and gallium [59,61], germanium [61], indium [61] (on the Sn side). It turned out that some elements have limited solubility in Nb_3Sn (e.g., Zr, Hf [59], and Ge [61]). It was also reported that some elements may influence Nb_3Sn layer growth rate (e.g., Ti, Zr and Hf [59]) and Nb_3Sn grain size (e.g., Ga can cause grain coarsening [59]). Dopants may have different influences on Sn content of Nb_3Sn as well, depending on whether they substitute Nb or Sn. For example, it was found that the Sn at.% decreased mildly with the additions of Ta, Mo, and V, but drastically with Ti and especially Zr [60]. This was argued to be an indication of the fact that Ta substitutes Nb while Ti sits on Sn when they dissolve in Nb_3Sn lattice [34].

The variations of T_c and B_{c2} with alloying contents for some elements from Ref. [60] are reprinted in Figure 14 (a) and (b), respectively. While small amounts of Ti and Ta additions led to slight increase in T_c, excess additions caused serious decrease. In contrast, V, Mo, and Zr additions decreased T_c monotonically, with the slope of Zr the sharpest. On the other hand, B_{c2} measurements showed that the additions of Ti and Ta resulted in significant increase (by >3 T) in B_{c2}, while V and Mo had weaker effects. The addition of Zr worked positively only in a small amount (~0.36 at.%) associated with a very limited increase of B_{c2} (by 0.7 T). Over doping of Ti, Ta, V, and Mo would also decrease B_{c2}. The optimum amount of Ti is around 1.5 at.%, and that of Ta is around 4 at.%, both lead to a maximum B_{c2} of 27 T at 4.2 K. Suenaga *et al.* [60] contended that the positive effect on T_c and $B_{c2}(0)$ by Ti and Ta doping was because these additions could

suppress the tetragonal transformation by depressing the tetragonal transformation temperature.

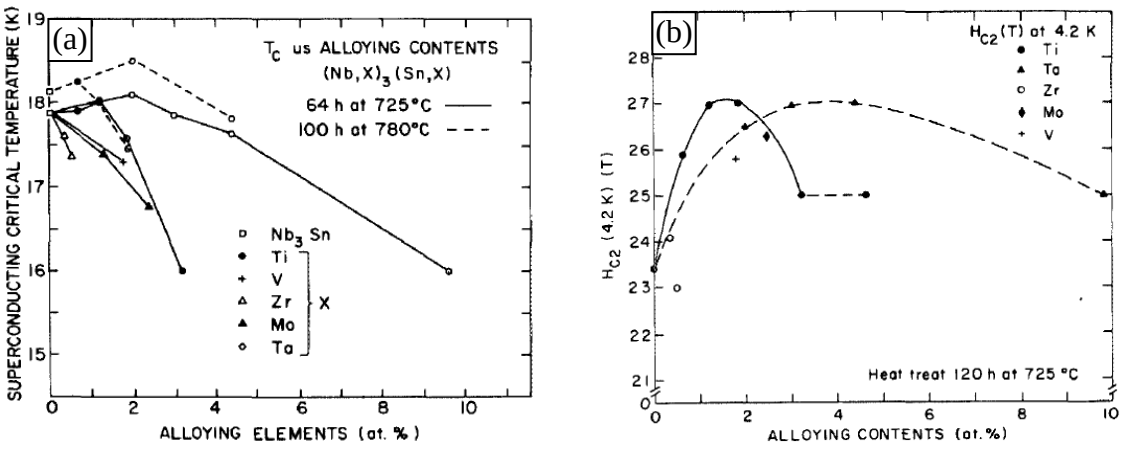

Figure 14. Variations of (a) T_c and (b) B_{c2} (4.2 K) with alloying contents for Ti, Ta, Zr, Mo, and V additions [60].

The study by Bormann *et al.* [7] on Nb_3Sn films showed that the addition of Ga may have the best influence on Nb_3Sn: it can significantly increase $B_{c2}(0)$ (to nearly 35 T) without degrading T_c. However, the use of Ga is limited because of some technical difficulties [60].

Although Ta and Ti are both the most widely used additives at present due to their great benefits to B_{c2} of Nb_3Sn, they are different in several aspects. First, Ta doping can be easily realized by using the commercially available Nb-7.5wt%Ta alloy, while because Nb-1.5at.%Ti alloy is not commercially available, practically Ti is introduced by either using Sn-Ti alloy or distributing commercially available Nb-47wt.%Ti rods in pure Nb metal so that Ti can diffuse into Nb during heat treatments [23,62]. Second, Ti both

segregates at Nb_3Sn grain boundaries and dissolves in Nb_3Sn lattice [21, 63], while Ta in Nb-7.5wt.%Ta can be entirely incorporated to Nb_3Sn lattice. Third, while it was reported that small amount of Ta addition (up to 10 at.%) had little effect on Nb_3Sn growth kinetics [64], Ti works effectively to enhance the diffusivity of Sn and the Nb_3Sn layer growth rate [65]. Fourth, Ta has no influence on the Nb_3Sn grain size, while Ti doping increased grain size by decreasing the activation energy of grain growth [39], so that Ti doping could flatten the $J_c(B)$ curves by not only increasing high field J_c but also reducing low field J_c [39,60,66,67]. Fifth, Ti atoms are believed to substitute the Sn atoms, while Ta atoms sit on Nb sites in the Nb_3Sn lattice [34]. Finally, it is found that Ti helps reduce the strain sensitivity of Nb_3Sn better than Ta [68]. It was reported that strands with simultaneous Ta and Ti additions in proper amounts had similar B_{irr} values with exclusively Ti doped strands, while the strands with only Ta doping via Nb-7.5wt.% Ta alloy had lower B_{irr}s for the same heat treatments [69, 70]. The stronger effect on B_{irr} improvement by Ti doping than Ta doping was also reported in [71]. In [69] as the heat treatment temperature was increased, B_{irr}s of Ta-doped and Ti-doped wires both finally reached 27-28 T (at 4.2 K), which is consistent with Suenaga's results [60]. According to [69], for RRP type strands, Ti doped ones can achieve high B_{irr}s ($\geq$ 26 T at 4.2 K) at low reaction temperatures (650-665 °C), while in order for those RRP strands with only Ta doping to achieve such high B_{irr}s, very high reaction temperatures (nearly 700 °C) have to be used.

1.6. Summary of the introduction and objective of this dissertation

This dissertation aims to explore the prospects to further improve the non-matrix J_c of Nb_3Sn strands. As discussed in this chapter, the non-matrix J_c of a strand is determined by the superconducting area fraction and Nb_3Sn-layer J_c, which is further determined by $F_{p,max}$ and B_{irr}. Improving $F_{p,max}$ can be realized by introducing artificial pinning centers and refining grain size, which requires reducing reaction temperatures. Improving B_{irr} can be realized by homogenizing the Nb_3Sn layer, raising Sn content to near stoichiometry and proper doping. Thus, this dissertation is mainly comprised of three parts, discussing prospects to improve Nb_3Sn area fraction, $F_{p,max}$ and B_{irr}, respectively.

In chapter 3, a model will be developed to find out the influence of the fractions of precursors in the green-state strands on the fraction of the supercurrent-carrying Nb_3Sn area in the fully-reacted subelement, and what the possible maximum current-carrying Nb_3Sn area fraction in subelements is. Also, it is noticed that the tubular strands have lower fine-grain Nb_3Sn area fractions than RIT strands. This chapter will also discuss the possibility of improving the fine-grain Nb_3Sn area fractions in tubular strands by improving their filament architecture.

Chapter 4 will first discuss a possible route to reach the maximum B_{c2} of Nb_3Sn. Then a model is developed aiming to find out what essentially determines the Sn content of Nb_3Sn formed in a Sn source/Nb_3Sn/Nb diffusion reaction couple.

Chapter 5 will discuss how to introduce grain refiners to Nb_3Sn wires, and will demonstrate that the internal oxidation method can markedly refine Nb_3Sn grain size and

can be used in wires. Finally, a prediction about the ultimate J_c that can be achieved in Nb_3Sn wires is given.

Chapter 6 will summarize this dissertation and give the conclusions.

Chapter 2: Experimental Methods

Most of the green-state Nb_3Sn strands used in this dissertation were fabricated at Hyper Tech Research Inc. The details of these strands are described in each chapter. Preparations for strand heat treatments and characterization methods are discussed below.

2.1. Strands Heat Treatment

Depending on the intended characterization methods, the green-state Nb_3Sn strands were mainly heat treated in two scenarios: (i) for voltage - current (*V-I*) transport measurements using the four-point method on long pieces (> 1 m) of samples, green-state strands were wound and heat treated on ITER-type barrels, (ii) for microscopy studies, magnetic measurements and *V-I* measurements on short pieces (typically < 10 cm), short straight strands were heat treated. In either case, the strands had to be heat treated in atmospheres with very low contents of reactive gases (e.g., oxygen) to prevent contamination or reaction (e.g., oxidation) of the strand materials at elevated temperatures. The only exception is a particular experiment in chapter 5, where a short, straight strand were heat treated in atmospheres with controlled oxygen partial pressures, which will be specified in detail in chapter 5.

For the heat treatments of long pieces of strands, ITER type barrels with an outer diameter of 32 cm and a length of 28.6 cm were machined from Ti-6Al-4V alloy and fitted with Cu rings on each end. Ti-6Al-4V is used for ITER barrels because this alloy has a thermal contraction coefficient that matches that of Nb_3Sn better than other materials (e.g., stainless steel), and thus causes smaller strain as the barrel and the strand are cooled down together from the reaction temperature to 4.2 K. However, because it is difficult to solder Ti-6Al-4V alloy to the current leads during preparation for *V-I* measurements, two Cu-end rings were fitted to the Ti-6Al-4V barrel, and fixed using stainless steel screws. The Ti-6Al-4V barrel and the two Cu end-rings were threaded into matching helical grooves, to minimize the strand motion under Lorentz force during *V-I* measurements in magnetic fields. The pitch length for the grooves is 3.2 cm. A single piece of green-state strand about 1.5 m in length (with both ends rolled or sealed with a blowtorch against subsequent Sn leakage during heat treatments), was wound around the grooves in the Ti-6Al-4V barrel and the Cu end-rings, and fixed to the Cu end-rings with stainless steel screws. Then they together were heat treated in well-closed furnaces under flowing argon to guarantee low reactive gas contents.

For the heat treatments of short pieces, straight green-state strands of about 25 cm in length were also rolled or torched on their ends, after which they were either put into open-ended Nb tubes and heat treated in closed furnaces under flowing argon, or sealed in quartz tubes with reactive gases removed, and then transferred to furnaces for heat treatment. In the latter case, the quartz tubes containing the strands were pumped to high vacuum ($<10^{-3}$ Pa) using a system equipped with a regular mechanical pump (which

provides a rough vacuum for the system), a cold trap (which uses liquid nitrogen to condense gases from the quartz tube and back-streaming oil vapor from the diffusion pump), and an oil diffusion pump (for providing high-speed oil vapor that transfers momentum to gas molecules from the quartz tubes) in series. Then the quartz tubes were backed up with ~0.3 bar of argon (which corresponds to about 1 atm at the heat treatment temperatures, 600-700 °C) before being sealed and transferred to furnaces for heat treatments.

The specific heat treatment schedule for each experiment will be described in each chapter. Magnetic, microscopy, and short-piece transport J_c studies were performed on strand pieces removed from the centers of the heat treated short, straight samples.

2.2. Sample Characterizations

Characterization methods used in this dissertation include scanning electron microcopy (SEM), energy dispersive X-ray spectroscopy (EDS), transmission electron microscopy (TEM), X-ray diffraction (XRD), vibrating sample magnetometer (VSM), and transport *V-I* measurements, etc.

A scanning electron microscope is a machine that can produce a focused beam of accelerated electrons and use it to scan the surface of a conductive sample, and generate images using the signals produced by the interaction between the electron beam and the sample. As the accelerated incident electrons travel into the sample body, they can: i)

knock out outer-shell electrons of sample atoms out of the sample (these electrons are called “secondary electrons”), ii) be bounced back by nuclei of sample atoms and become “backscattered electrons”. Moreover, as inner-shell electrons of sample atoms are knocked out, some outer-shell atoms may jump to these vacant sites and release the extra energy in X-rays. The secondary electrons (SE), backscattered electrons (BSE), and X-rays are the most commonly used signals for SEM. Each of them gives unique information about the sample. Secondary electrons have low energy, so only those within a small depth (tens of nanometers) below the sample surface can escape from the sample. Thus, the yield of secondary electrons is sensitive to the sample surface topography: holes reduce the number of secondary electrons, while hills increase it, causing brightness contrast in the SE images. Backscattered electrons, on the other hand, generally have much higher energy and can escape from a relatively larger depth (1-2 μm), and are less sensitive to surface topography. Instead, the yield of backscattered electrons is sensitive to the atomic numbers of the probing area: high-atomic-number elements yield more backscattered electrons and thus appear brighter in the image. Since the energies of electrons at each shell (K, L, M, etc.) for different atoms are different, the energies of the characteristic X-rays emitted by the sample reveal which atoms are in the probing area and their strengths can be used to calculate the composition of the sample. The use of these three signals for Nb_3Sn and their sample preparation methods will be discussed individually below.

The SE image of a surface mainly reflects its topography. The most commonly used sample preparation method to get SE images of a reacted Nb_3Sn sample is simply to

fracture it by bending, and then take SE images on the fractured surface. The phases in a Nb_3Sn strand can be distinguished from their unique fracture modes and characteristics. For example, metals and alloys (e.g., Nb alloys) are ductile and thus show micro-void coalescence fracture mode, while the Nb_3Sn phase is a brittle intermetallic compound and usually displays an inter-granular fracture mode, and the Nb_6Sn_5 phase that contacts the Nb_3Sn layer has a long-needle morphology. Meanwhile, fine grain (FG) and coarse grain (CG) Nb_3Sn areas can also be differentiated due to their quite different grain sizes. Due to inter-granular fracture in FG Nb_3Sn area, high-magnification SE images of fractured surfaces are often used to calculate Nb_3Sn grain size. This technique will be heavily used in chapter 4. SEM images for this analysis were taken on a Sirion field emission SEM which has a spatial resolution of 1-3 nm in the ultra-high resolution mode. In this work, the Nb_3Sn grain size was calculated in a way described in [72]: the outlines of grains were drawn, and their cross-section areas were measured, and these cross sections were regarded as circles for the calculation of their diameters; a large number (generally > 50) of grains in random were averaged to calculate the average grain size. The grain sizes calculated from SE images on fractured surfaces were compared with those obtained from TEM images, and very good agreement was seen.

The BSE image mainly reflects compositional variation. To obtain BSE images of a sample, one needs to polish it to a very flat, smooth surface to avoid the influence of surface topography. Images of either the transverse or the longitudinal cross section of a Nb_3Sn strand can be obtained. To permit handling, wire samples must be first attached to a mount prior to polishing because they are usually small. One way to do this is to solder

or stick (using conductive pastes) the samples to a metal block (e.g., Cu), with the strand axes either parallel or perpendicular to the surface to be polished. After that the Cu block carrying the samples can be mounted using either "cold mount" or "hot mount" techniques. For the former, the block was put in a liquid mixture of epoxy resin, epoxy resin hardener, and graphite powder (which was added in to ensure a good electric conductivity) in proper ratios, and cured for 6-8 hours at room temperature. For the latter, the block was buried in conductive Bakelite powder, which was then compacted under high pressures and at elevated temperatures (~180 °C) for about ten minutes. After being mounted, the samples were then polished to obtain a smooth surface. The samples were first polished using SiC abrasive papers on a polishing station to 1200-fine, and then polished on a short-nap polishing cloth with 1 μm diamond paste for 5 minutes. The final polishing step was performed on a long-nap polishing cloth with either 0.25 μm diamond suspension (for green-state Nb_3Sn strands), or with 0.05 μm colloidal silica suspension (for reacted Nb_3Sn samples). The green-state Nb_3Sn strands cannot be polished using 50 nm colloidal silica suspension because the alkaline environment can attack the Sn metal. The samples were cleaned ultrasonically after each step. BSE images were also taken on the Sirion SEM mentioned above.

Compositions of phases were measured using energy dispersive X-ray spectroscopy (EDS) in the BSE mode, on an FEI QUANTA 200 SEM with EDS attachment. The most common elements in Nb_3Sn phase in a Nb_3Sn wire are: Nb, Sn, Cu, Ta, and Ti. The signal of each element must be properly chosen to avoid spectrum overlap. For example, due to significant overlap between CuK and TaL signals, CuL and TaM peaks were used

to determine the Cu and Ta contents. It is well known that a higher accelerating voltage leads to a larger interaction volume, which undermines the spatial resolution. For instance, for Nb_3Sn the diameter for the interaction volume at 20 kV is about 2.0 μm, while that for 15 kV is only 1.2 μm, which can be calculated using an Monte-Carlo simulation software. However, the accelerating voltage should be at least 2-3 times of the exciting energies of the selected signals for all present elements. Taking account of all of these effects, an accelerating voltage of 15 kV was used, and CuK, TaM, NbL, SnL, and TiK signals were used for the calculation of element fractions in Nb_3Sn. For each spot data were collected for long enough periods to enhance the signal-to-noise ratio. To guarantee the reliability of the EDS results, a standard Nb_3Sn bulk sample with a composition of Nb-25 at.% Sn fabricated in Research Center Karlsruhe was used for calibration prior to each measurement.

In contrast to SEM, TEM uses much higher accelerating voltage (>100 kV) and works on a very thin sample (typically ≤ 200 nm) so that electrons can pass through the sample after being deflected by the lattice. Images are generated by detecting the scattered electrons. In this dissertation specimens were prepared via focused ion beam (FIB) using an FEI dual-beam Helios NanoLab 600. A thin foil of ~1.5 μm thickness was first trenched out of the region of interest and attached to a Cu grid, and then thinned to ~100 nm using incidenting Ga ion beam. The whole operation process can be viewed in a window using the SE signals. Finally, the foil was observed in an FEI/Philips CM-200T TEM, which was operated in an accelerating voltage of 200 kV.

Magnetic measurements were performed using the vibrating sample magnetometer (VSM) function of a Quantum Design Model 6000 "physical property measuring system" (PPMS) on strand pieces about 4-5 mm long removed from the centers of heat treated short, straight samples. The VSM can measure the magnetic moment, *m*, of a sample as a function of the applied field *B* or the temperature *T* by vibrating the sample at a certain frequency and measuring the induced voltage using a pickup coil.

Magnetization (the magnetic moment normalized to the superconductor volume) vs applied magnetic field (*M*-*B*) loop measurements were performed at a certain temperature (e.g., 4.2 K) on samples oriented parallel or perpendicular to applied fields within ±14 T at a field ramp rate of 13 mT/s. The heights of the *M*-*B* loops, ΔM, were used to calculate the magnetic J_c-*B* curves of the superconducting samples. The equations used for the calculations are based on the following assumptions. First, the Nb_3Sn layer in a subelement is represented by a hollow cylinder of a uniform, isotropic superconductor, so that J_c is the same everywhere in the sample. Second, the derivations are based on the "semi-Bean" model (i.e., assuming the density of current flowing in the sample is just its J_c, and J_c varies with field *B*, but does not vary with position in the superconductor). Third, the superconductor is in the fully penetrated state (in type II superconductors with fluxon pinners, flux lines move into the superconductor body as the applied magnetic field increases, and the superconductor is in the fully penetrated state as the fluxons have penetrated into its inner-most part so that now the supercurrent is flowing everywhere in the superconductor body). Then it can be easily derived that as the applied field is

perpendicular to the axis of the hollow cylinder, the magnetic moment produced by the critical current density J_c in the superconductor is:

$$m_{\perp} = J_c L(d_o^3 - d_i^3)/6 \tag{2.1}$$

where L is the length of the sample, d_o and d_i are the outer and inner diameters of the current-carrying Nb_3Sn layer, respectively. Therefore, the height of the *M-B* loop is:

$$\Delta M_{\perp} = 4J_c d_{eff}/(3\pi) \tag{2.2}$$

where ΔM is Δm over the superconducting volume, i.e., $\pi L \cdot (d_o^2 - d_i^2)/4$ for a hollow cylinder, and d_{eff} is the effective subelement diameter: for a hollow cylinder, $d_{eff} = d_o(1-\eta^3)/(1-\eta^2)$, in which $\eta = d_i/d_o$. Apparently, d_{eff} is not necessarily equal to the subelement diameter d_{sub}, but the difference is usually within 10% for a fully reacted Nb_3Sn subelement.

For the case that the applied field is parallel with the axis of the hollow cylinder, the magnetic moment produced is:

$$m_{\parallel} = \pi J_c L(d_o^3 - d_i^3)/12 \tag{2.3}$$

Thus, the height of the *M-B* loop is:

$$\Delta M_{\parallel} = J_c d_{eff}/3 \tag{2.4}$$

From equations 2.2 and 2.4, it is clear that as the applied field direction is shifted from parallel to perpendicular to the strand axis, ΔM should increase by $4/\pi = 27\%$ in the fully penetrated state. But practical multifilamentary Nb_3Sn strands do not exactly follow the above assumptions (because, for example, the Nb_3Sn superconductor is not homogenous everywhere), so the variation can be more complex [73]. From the measured

M-B loops, magnetic $J_c(B)$ can be calculated using Equations 2.1 – 2.4. It has been verified that the magnetic J_c determined from $\Delta M_\perp$ can be quite close to transport J_c [24].

Besides *M-B* loops, the other important magnetic measurement for Nb_3Sn samples is the magnetization vs temperature (*M-T*), which can be measured at different magnetic fields (e.g., 5 mT, 2 T, ..., 14 T) between 5 and 20 K and used to determine the critical temperature T_cs of Nb and Nb_3Sn at different fields. The T_c values were determined as the 50% of the superconducting transitions, as shown in Figure 15, following the method described in [74] in detail. From the measured T_c values at different magnetic fields (up to 14 T), the T_c-*B* (or inversely, B_{c2}-*T*) curves can be obtained, which can be used to calculate $B_{c2}(0)$ by extrapolation using the Maki-DeGennes (MDG) theory.

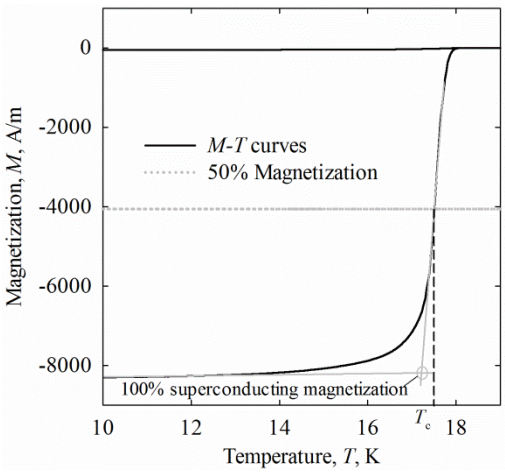

Figure 15. An illustration of the determination of superconducting transition temperature from an *M-T* curve.

Transport J_c measurements can be performed on two types of samples: long samples wound on ITER barrels and short, straight samples. Different probes were used to

perform these two types of measurements, although both were based on the four-point measurement technique.

After being heat treated on ITER barrels, the segments of the strands that were wound on the Cu-end rings were soldered down to the Cu end rings so that the applied transport current could flow from the Cu end rings, which themselves would be soldered to the current leads, to the strands to be measured. It was previously found that the transition regions between the Cu end rings and the Ti-6Al-4V barrel were the weakest parts of the sample, and as such might degrade the I_c results of the whole sample strand. To assist current transfer through these regions, a 3-loop sister strand was carefully rotated to each transition region and soldered together with the sample strand. The barrels were then mounted onto a current-carrying probe with the two Cu-end rings soldered to the positive and negative current leads, respectively, and voltage taps were soldered on the sample strand at a separation (gauge length) of 50 cm. A thin layer of thermally conductive blue stycast was painted on the barrel to prevent the strand motion during measurement. The measurements were performed in liquid helium in fields perpendicular to the strand axis from 0 T to 14 T; the I_cs were determined from the measured current-voltage (*I*-*V*) curves at a voltage criterion of 0.1 μV/cm.

For measurements of short samples, straight segments of 4-5 cm were put on a G10 piece attached to a current-carrying probe and soldered to the two fixed current leads. Voltage taps were soldered in the center of the samples at a separation (gauge length) of 5 mm. Typically 2 cm is sufficient for current transfer from the Cu matrix to Nb_3Sn superconductor in Nb_3Sn strands. The measurements were performed in liquid helium in

magnetic fields perpendicular to strand axes; the I_cs were determined from the measured current-voltage (I-V) curves at a voltage criterion of 1 μV/cm. Following the measurements of I_c, the three types of J_c, i.e., Nb_3Sn-layer J_c, non-matrix J_c, and whole-wire J_c (or engineering J_c) can be calculated.

Chapter 3: The area fraction of supercurrent-carrying Nb_3Sn in subelements

In this chapter the area fraction of current-carrying Nb_3Sn phase in a subelement is discussed. This factor does not influence the quality of Nb_3Sn phase, but affects the non-matrix and engineering J_cs of Nb_3Sn strands.

3.1. The influence of area utilizations on the non-Cu J_cs of present high-J_c Nb_3Sn wires

At present the highest reported non-Cu J_cs of rod-in-tube (RIT), powder-in-tube (PIT), and tube type strands at 4.2 K, 12 T are ~3000, 2700, and 2500 A/mm^2, respectively. Even higher values can be achieved (e.g., 3500 A/mm^2 for RIT strands [75]) if RRR is sacrificed, but this would lead to problems for application and is not considered here. Work [24] shows that both the Nb_3Sn stoichiometry and the grain size of tube type strands are more or less equivalent to those of the best RIT strands: for the two types of strands (both with 7.5wt.% Ta addition) reacted at ~650 °C, the Sn contents are 22-24 at.%, leading to B_{irr}s of 24-26 T at 4.2 K, while grain sizes of both are around 120 nm. This leads to similar layer J_cs in both tube type and RIT strands, 5000-6000 A/mm^2 at 4.2 K, 12 T. Similar values are also reported in optimized PIT strands [29].

So what accounts for the difference in their non-Cu J_cs? Area fraction analysis shows that the cause for the lower non-Cu J_c in tubular strands is their lower current-carrying Nb_3Sn area fractions. BSE images of a RIT and a tube type Nb_3Sn subelements (both fully reacted) are shown in Figures 16 (a) and (b), while SE images on fractured surfaces are shown in (c) and (d), respectively.

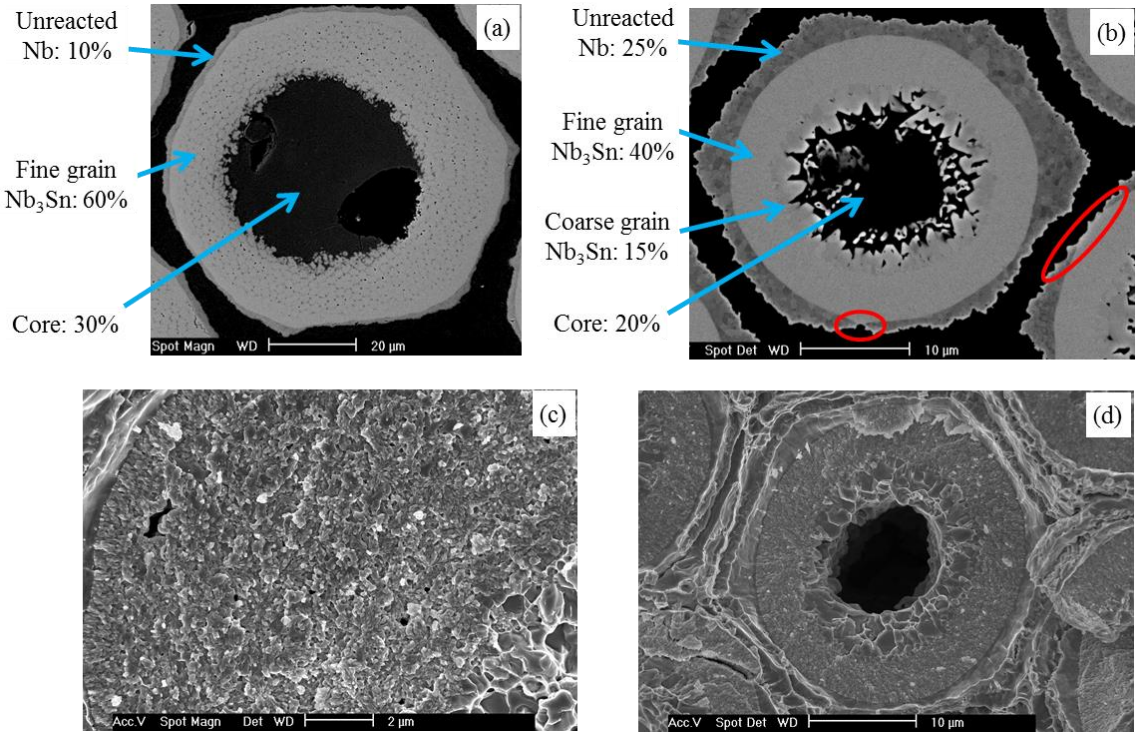

Figure 16. BSE images of fully-reacted (a) RIT and (b) tube type Nb_3Sn subelements, and SE images on fractured surfaces of (c) RIT and (d) tube type Nb_3Sn subelements.

As can be seen, tube type strands have two types of Nb_3Sn areas: fine-grain (FG) Nb_3Sn with a grain size of typically 100-200 nm when reacted at 625-700 °C, and coarse-grain (CG) Nb_3Sn, of which the grain size is generally above 1 µm. This CG Nb_3Sn layer cannot conduct transport supercurrent because the non-superconducting Cu-Sn phase

separating these coarse grains blocks the supercurrent in the longitudinal direction, which can be seen from a longitudinal BSE image in Figure 17. In RIT strands the CG Nb_3Sn (including the disconnected Nb_3Sn particles, see Figure 16 c) area fraction is much lower. This leaves the fraction of FG Nb_3Sn at around 60%, with the rest composed of a core (~30%) and remaining Nb (5-10%), which serves as a barrier against the contact between the Nb_3Sn layer and the Cu matrix. In contrast, in a typical tube type or PIT strands, the FG region is only ~40%, the core region is ~20%, the CG region is 15-20%, and the unreacted Nb region occupies ~25%. It is clear that to improve the FG Nb_3Sn fraction in a tubular strand, both the unreacted Nb and the CG Nb_3Sn areas must be reduced. In the following two sections these two aspects will be addressed, respectively.

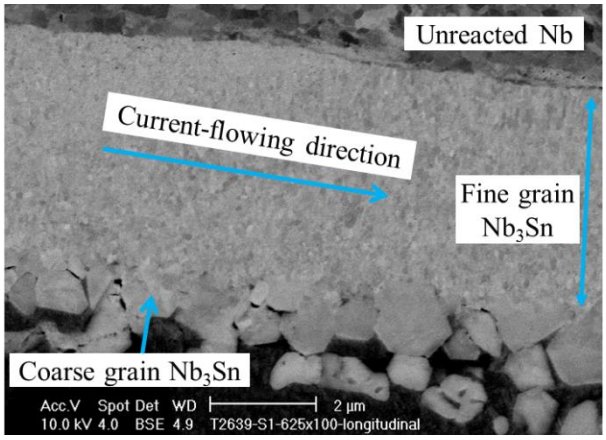

Figure 17. BSE image of a longitudinal section of a reacted tube type Nb_3Sn subelement.

3.2. Methods to reduce the unreacted Nb area

For normal tube type strands, reducing the Nb/Sn ratio in the starting strand would certainly decrease the remaining Nb area fraction in the fully reacted subelements. However, continued growth of the Nb_3Sn layer carries with it the risk that as the Nb layer is reacted through, Sn will diffuse out of the subelement and poison the surrounding Cu stabilizer, forming bronze, which has much lower electrical and thermal conductivities than pure Cu. As discussed in section 1.3, this would markedly undermine the stability of superconducting Nb_3Sn strands.

RIT, PIT, and tube type Nb_3Sn strands all have hexagonal subelements, however, as can be seen from Figure 16 (a) and (b), the remaining Nb in a RIT subelement is a thin, uniform layer protecting the Cu matrix effectively. On the other hand, the thickness of the unreacted Nb layer in a tubular subelement varies markedly from the subelement corner to its edge. The reasons for this difference are as follows. In RIT subelements Cu channels are distributed among Nb (or Nb-Ta) filaments and can extend to the Nb barrier; these Cu channels provide shortcuts for Sn diffusion because the diffusion rate of Sn in Cu-Sn is much higher than the Nb_3Sn layer growth rate, and thus allow a complete reaction of the filaments area which is hexagonal, making the unreacted Nb layer more or less uniform. On the other hand, in each tube-type subelement there is only one master Cu layer (between the central Sn core and the Nb alloy tube). Due to the absence of the Cu channels in a tubular subelement, the Nb_3Sn layer grows outwards in the Sn source/Nb_3Sn/Nb diffusion reaction couple in the cylindrical geometry and is thus

uniform in thickness. Sited within a hexagonal subelement, this cylindrical Nb_3Sn layer can touch the edges of the Nb layer while remaining far from its corners. Thus, a way to reduce the unreacted Nb fraction in tubular strands is to use round, instead of hexagonal, subelements. A BSE image of a green-state tube-type, round subelement is shown in Figure 18. In such an architecture, by starting with a proper Nb/Sn ratio, the Nb can be reacted to just (but safely) below the penetration threshold, as with the RIT strands.

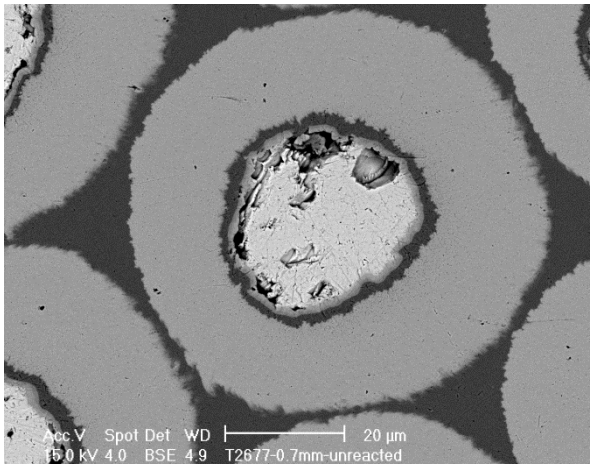

Figure 18. BSE image of a green-state tube type round subelement, fabricated by Hyper Tech Research Inc.

In reality this ideal situation is usually limited by the fact that the subelements, which are Sn/Cu/Nb composites, become distorted and eccentric after many courses of drawing. As a consequence, it is frequently observed that Nb barrier has been reacted through in some local spots allowing Sn leakage into the Cu matrix while the barrier is still thick elsewhere. An example is shown in Figure 16 (b), in which the local Sn leakage spots are marked by red ovals. Thus, the quality of a wire (e.g., regularity, homogeneity along the wire length, etc.), which highly depends on the quality of the starting materials (e.g.,

uniformness of hardness of the Nb alloy tube) and the wire-processing technique of a manufacturer, can significantly influence the balance between the remaining Nb area fraction and RRR of the reacted strands.

Another possible route towards reducing the barrier material area fraction without sacrificing RRR is to use barrier materials other than Nb. For example, Ta is used in bronze-process and single-barrier internal-tin strands. The reaction rate between Ta and Sn is much lower, so theoretically a much thinner Ta layer is required to prevent penetration. However, the chosen barrier materials must possess excellent ductility to allow for significant reduction without breakage; otherwise, another important parameter, d_{eff}, has to be sacrificed due to the difficulty to obtain small subelements. At present the possibility to improve the ductility of Ta by refining Ta grain size is being explored [76].

3.3. What is the FG Nb_3Sn fraction limit in a subelement

In order to find out what determines the CG Nb_3Sn content of a strand, one needs to know how the precursors Sn, Cu, and Nb metals or alloys transform to Nb_3Sn phase during heat treatments. Here we study this using a tube type strand, because tube type subelements have a standard structure of Sn/Cu/Nb precursors, while the structures in RIT and PIT strands are more complex. For a normal tube type strand, a typical heat treatment schedule is, the temperature is ramped up from room temperature to the

reaction temperature (typically 625-675 °C) at a certain ramp rate without intermediate heat treatments, and then kept at the reaction temperature for a certain duration for Nb_3Sn layer to grow. The process of Nb_3Sn layer formation and growth has been studied on tube-type strands with large subelement diameters in [25,65], where emphasis was placed on the stage when the temperature had been ramped to the final reaction temperature, while the phase transformations at low temperatures (i.e., during temperature ramping) were not addressed. However, it will be seen that low-temperature transformations are critical to the final phase fractions. Furthermore, large subelements in practical strands may have different phase transformation routes from those of small subelements in practical strands. This is because the larger diffusion distance in large subelements requires longer time for some transformations to occur and finish; as a standard temperature ramp rate (e.g., 50 °C/hour) is used, the temperature may have passed the window for the formation and growth of a phase (e.g., ~300-500 °C for the Cu-Nb-Sn ternary phase [74,77]) before it is fully formed. Apparently, the low-temperature phase transformations in a subelement are determined by both the subelement size and temperature ramp rate.

To examine the phase transformations taking place in the subelements of practical strands during heat treatment, the following study was carried out. Segments from a tube type strand with a subelement diameter of ~35 μm were sealed in quartz tubes, which were then pumped to high vacuum and backed up with argon, and then transferred to a single furnace for heat treatment. The heat treatment schedule was: the temperature was ramped from room temperature to 650 °C at a rate of 50 °C/hour, and then kept at 650 °C

for 512 hours. The samples were withdrawn from the furnace at different stages and quenched in water to preserve the phases at high temperatures, and then polished to obtain the BSE images and phase compositions via EDS. BSE images of the subelements at various heat treatment stages are shown in Figure 19.

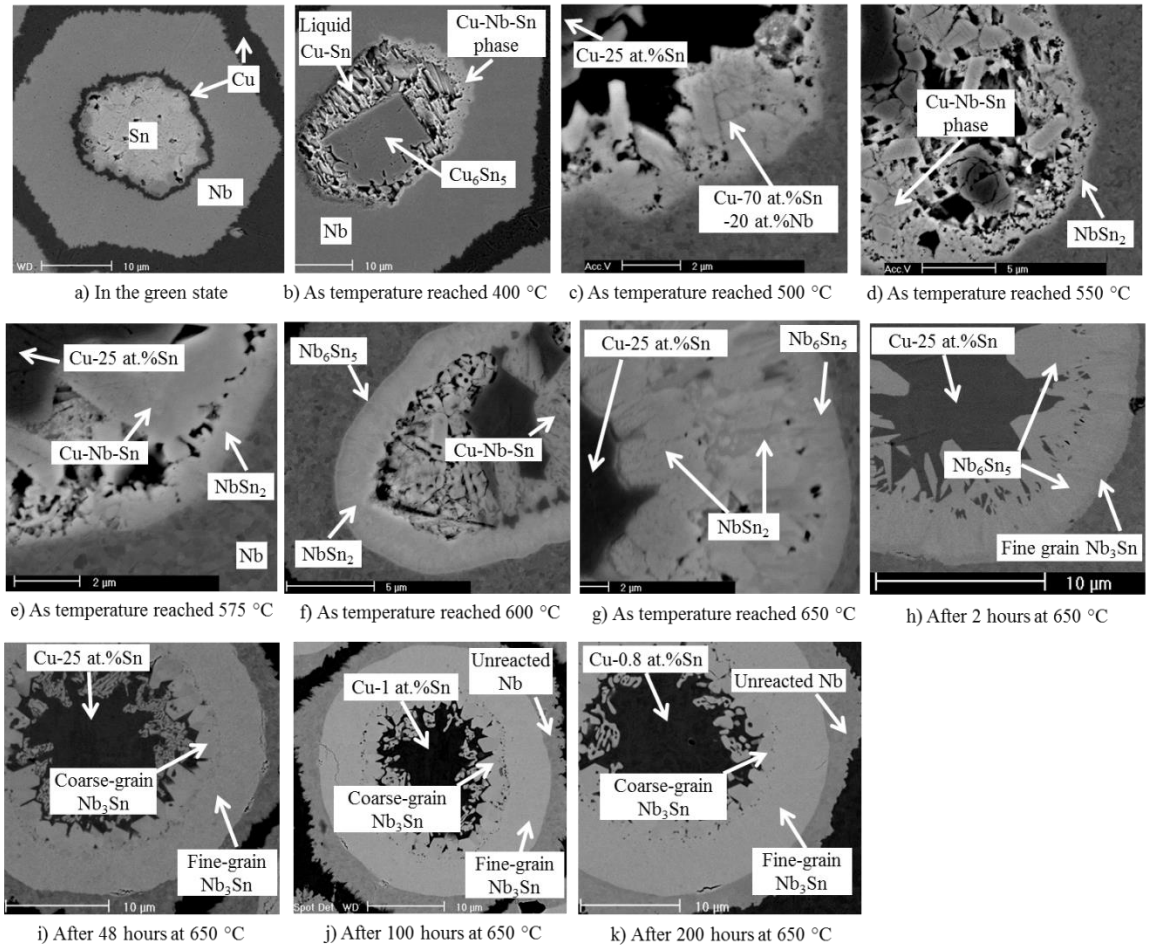

Figure 19. BSE images of a tube type subelement at different stages during heat treatment (with a temperature ramp rate of 50 °C/h).

As can be seen in Figure 19 (b), as the temperature reached 400 °C, what occurred was mainly a mixing of Cu and Sn. Since the amount of Sn was large relative to Cu, they

mainly formed liquid Cu-Sn phase and η-Cu_6Sn_5, with the Cu-Sn liquid directly contacting the Nb alloy tube and η phase masses flowing in the Cu-Sn liquid. In the meantime, there had been a thin layer of Cu-Nb-Sn phase formed on the inner surface of the Nb tube. According to [74,77], the Cu-Nb-Sn phase is first detected when the temperature reaches around 345 °C. As the temperature reached 500 °C (Figure 19 c), all of the liquid Cu-Sn and η-Cu_6Sn_5 had transformed to ε-Cu_3Sn phase, with the extra Sn used to form the ternary Cu-Nb-Sn phase with a composition of Cu-70 at.%Sn-20 at.%Nb as determined by the EDS. At 550 °C, a thin layer of $NbSn_2$ formed between the Cu-Nb-Sn layer and Nb, while the ε-Cu_3Sn phase still remained. As the temperature reached 575 °C, the $NbSn_2$ layer grew thicker. As the temperature reached 600 °C, while the Cu-Nb-Sn phase had not yet fully transformed to the $NbSn_2$ phase, a thin layer of Nb_6Sn_5 had formed between $NbSn_2$ and Nb, indicating that $NbSn_2$ had started to transform to Nb_6Sn_5. As the temperature reached 650 °C the ε-Cu_3Sn phase still remained, while all of the Cu-Nb-Sn had transformed to $NbSn_2$; meanwhile, at the outer layer, the Nb_6Sn_5 layer was growing. After two hours at 650 °C $NbSn_2$ had all transformed to Nb_6Sn_5, and a thin Nb_3Sn layer had formed between Nb_6Sn_5 and Nb. It seemed there were two types of Nb_6Sn_5: one was well connected to the Nb_3Sn layer and had columnar grain morphology (which could be observed from the SE images of fractured samples), while the other type was embedded in the Cu-Sn core and separated from the well-connected Nb_6Sn_5 layer by a series of pores filled by Cu-Sn. After 48 hours at 650 °C all the Nb_6Sn_5 had transformed to Nb_3Sn. It was found that Nb_6Sn_5 itself transformed to the coarse-grain Nb_3Sn (i.e., Nb_6Sn_5 => 2 CG-Nb_3Sn + 3Sn), with the free Sn diffusing across the formed Nb_3Sn layer

to the Nb_3Sn/Nb interface for the formation of new fine-grain Nb_3Sn. After the complete transformation of Nb_6Sn_5, the ε-Cu_3Sn phase began to release Sn for further fine-grain Nb_3Sn layer growth. From 100 to 200 hours at 650 °C, the Nb_3Sn layer almost stopped growing, with the Cu-Sn alloy in the core ended up with a composition of Cu-0.8at.%Sn.

From the observation of the above phase transformation process during heat treatments, the reaction between Cu-*x* at.% Sn and Nb can be summarized as follows: if *x* > 25 at.%, Cu-25 at.% Sn is first forms, while all the extra Sn is used to form Cu-Nb-Sn phase, which transforms later to $NbSn_2$, then Nb_6Sn_5, which transforms to the coarse-grain Nb_3Sn, releasing the extra Sn for fine-grain Nb_3Sn layer growth. After Nb_6Sn_5 is depleted, Cu-25 at.% Sn then supplies Sn for further FG Nb_3Sn layer growth until the Sn content in the Cu-Sn source decreases to the point at which the chemical potential of Sn equals to that of Nb-17 at.%Sn, which will be discussed in chapter 5. It can be inferred that if $x \leq 25$ at.%, then only fine-grain Nb_3Sn forms due to the absence of intermediate phases. This is consistent with the fact that no CG Nb_3Sn forms in bronze-process and single-barrier internal-tin strands.

Based on the above observations and analysis, an analytical model was developed to predict the coarse-grain and fine-grain Nb_3Sn amounts for a fully-reacted tube type strand based on the starting Sn, Cu, and Nb amounts in the green state (see Figure 19 a). Since Nb is in excess for any subelement, such that after reaction there is a remaining Nb layer for protecting the Cu matrix, there are only two variables: the radius of the Sn core, R_1, and the radius of the outer boundary of the Cu layer, R_2. The most important assumption for this model is that Cu and Sn have been homogeneously mixed before reacting with

Nb. Thus, a high Sn/Cu ratio that makes the Sn content of Cu-Sn alloy higher than 25 at.% leads to formation of CG Nb_3Sn, while a low Sn/Cu ratio does not. For the derivations of this model, it is also assumed that there is no expansion in the filament area. In fact, there is indeed a 2-4% expansion, but it doesn't change the results much. The details of the derivations for the model, which are based on mass conservation (i.e., assuming there is no Sn loss during heat treatment), can be found in paper [78]. The results of the outer radius of Nb_3Sn area (R_{4f}), the FG and CG amounts (A_{FG} and A_{CG}) are shown in Equations 3.1-3.3, respectively.

$$R_{4f} = \sqrt{\left[3.3\frac{V_m^{Nb}}{V_m^{Sn}} - \frac{1}{5}\left(\frac{X}{1-X}\right)\frac{V_m^{Nb}}{V_m^{Cu}}\right]R_1^2 + \left[1 + \frac{1}{5}\left(\frac{X}{1-X}\right)\frac{V_m^{Nb}}{V_m^{Cu}}\right]R_2^2} \tag{3.1}$$

$$A_{FG} = \pi\left[\frac{3}{5}\frac{V_m^{FG}}{V_m^{Sn}} - \frac{2}{5}\left(\frac{X}{1-X}\right)\frac{V_m^{FG}}{V_m^{Cu}}\right]R_1^2 + \frac{2}{5}\pi\left(\frac{X}{1-X}\right)\frac{V_m^{FG}}{V_m^{Cu}}R_2^2 \tag{3.2}$$

$$A_{CG} = \frac{2}{5}\pi\left[\frac{V_m^{CG}}{V_m^{Sn}} + \left(\frac{X}{1-X}\right)\frac{V_m^{CG}}{V_m^{Cu}}\right]R_1^2 - \frac{2}{5}\pi\left(\frac{X}{1-X}\right)\frac{V_m^{CG}}{V_m^{Cu}}R_2^2 \tag{3.3}$$

In equations 3.1-3.3, V_m^{Nb}, V_m^{Sn}, V_m^{Cu}, V_m^{FG}, V_m^{CG} represent the molar volumes of Nb, Sn, Cu, FG Nb_3Sn and CG Nb_3Sn, respectively, and X represents the Sn content in Cu-Sn alloy as Nb_6Sn_5 serves as Sn source (e.g., X is around 0.25 according to Figure 19). From the Equation (3.3), it is clear that A_{CG} decreases with A_{Cu}/A_{Sn}, reaching zero as A_{Cu}/A_{Sn} is equal to 1.18, which is equivalent to Cu-25 at.% Sn, because there would be no intermediate phases formed as the Sn content in the starting Cu-Sn alloy is below 25 at.%. To test the model, tube type wires of various Cu/Sn ratios were fully reacted, and

the FG and CG Nb_3Sn area fractions were calculated, and it was found that the results agreed very well with the predictions of equations 3.1-3.3 [78].

Previously the phase transformations were usually predicted based on the phase diagrams at the final reaction temperature. The isothermal cross section of the ternary Cu-Nb-Sn phase diagram at 675 °C [26,79] is reprinted in Figure 20. According to this phase diagram, as long as the composition of the core (the cores of PIT strands contain three elements - Nb, Sn, Cu) is located to the left of the dashed line in Figure 20, there would be no CG formed because the formation of Nb_6Sn_5 is prevented due to thermodynamic instability. From this perspective, the X value for equations 3.1-3.3 should be 0.27, according to Figure 20. Furthermore, since the X value for the Cu-Nb-Sn ternary phase diagram changes with temperature, it is expected that the FG and CG fractions should depend heavily on the final reaction temperature. This may apply to large subelements or relatively large temperature ramp rates. For small subelements, however, the phase transformations at low temperatures, which cannot be predicted by the high-temperature phase diagrams, can lead to different results. For example, it turns out that the FG and CG fractions are almost not influenced by reaction temperature.

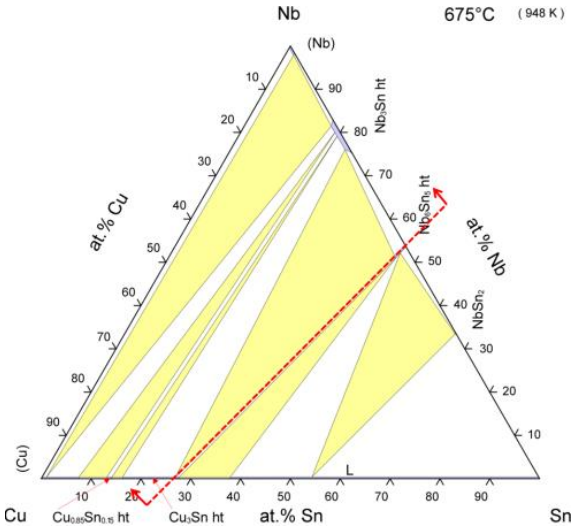

Figure 20. The 675 °C isothermal section of the ternary Cu-Nb-Sn phase diagram [26]. The red dashed line marks the boundary of the composition of the core in a PIT strand to the left of which no CG would form.

Figure 21 shows the fractions of fine-grain Nb_3Sn, coarse-grain Nb_3Sn, and core area to πR_{4f}^2 as a function of Cu/Sn ratio, calculated from equations 3.1-3.3. It can be seen that as more Cu is added relative to Sn, the CG amount decreases. Although the increase of Cu/Sn ratio leads to a marked increase in the core area, the FG Nb_3Sn fraction can still increase by over 10%. According to this figure, the fine-grain Nb_3Sn fraction is at its maximum when the Cu/Sn ratio reaches the point where the coarse-grain Nb_3Sn ratio drops to zero. A larger Cu/Sn ratio relative to this point simply increases the core area and dilutes the fraction of Nb_3Sn area.

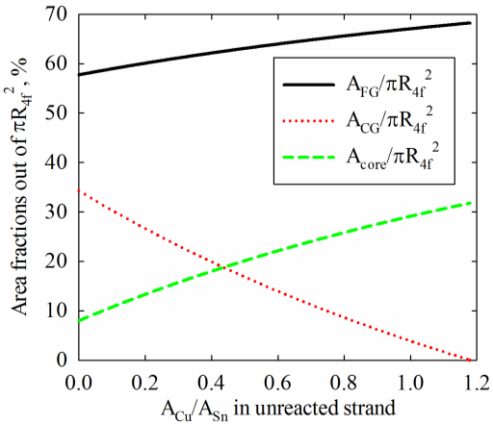

Figure 21. Fractions of FG Nb_3Sn, CG Nb_3Sn, and the core relative to πR_{4f}^2 as functions of Cu/Sn ratio, calculated from equations 3.1-3.3.

Assuming that tube type strands can achieve the same unreacted Nb fraction (5-10%) with RIT strands, then according to Figure 21, it can be estimated that the limit of the fine-grain Nb_3Sn fraction in a subelement is about 62 - 65 %.

The Cu/Sn ratios in RIT strands (typically 3:2 to 1:1) are between those of single-barrier internal-tin strands (typically 5:1 to 9:1) and tube type strands (typically 4:5 to 1:2). Typical heat treatment schedules for RIT strands are: the temperature ramped up to 210 °C, and kept at 210 °C for 48 hrs, and then ramped up to 400 °C, and kept at 400 °C for 48 hrs, and then ramped up to the final reaction temperature (e.g., 650 °C), and kept at that temperature for a certain duration (e.g., 50 hours) for Nb_3Sn layer growth. The pre-heat treatments at 210 °C and 400 °C are intended to make Sn spread uniformly in the Cu network before reaching the temperature for Nb_3Sn formation. However, whether the stage at 400 °C is truly needed still requires further verification [80]. The BSE images showing the phase transformations in a RIT subelement during heat treatments are shown

in Figure 22. Samples were quenched at different stages, similar to those of tube type strands.

As can be seen, after 210°C/48 h+400°C/50 h (Figure 22 b), the Sn core had mixed with the Cu channels among the filaments in the several inner rows of Nb alloy filaments, and had formed η phase (Cu_6Sn_5), and a thin layer of Cu-Nb-Sn ternary phase had formed, with the composition of 13.1at.%Cu-2.1at.%Ta-20.7at.%Nb-64.1at.%Sn. However, Sn had not diffused to the several outer rows. During the inter-diffusion between Cu and Sn, since the diffusivity of Cu is higher than that of Sn, Kirkendall voids formed in the original Cu channels. By the time the temperature reached 500 °C (Figure 22 c), the η phase had decomposed, the ε phase had formed and the extra Sn had been used to form more Cu-Nb-Sn phase, which is localized in the first one or two rows. As the temperature reached 650 °C (Figure 22 e), the Cu-Nb-Sn phase had transformed to $NbSn_2$ phase, which had partly transformed to Nb_6Sn_5 after 10 minutes at 650 °C (Figure 22 f). The Nb_6Sn_5 phase had almost disappeared after 30 minutes at 650 °C (Figure 22 g). From Figure 22 (h) it can be seen that due to volume expansion as Nb-7.5wt.%Ta filaments transformed to Nb_3Sn, the filaments merged and the voids in the original Cu channels shrank and became Cu-rich regions.

Similar to the observations by Pong et al. [80], we can see from Figure 22 that: i) the intention of diffusing Sn to Cu channels among Nb alloy filaments using pre-heat treatments does not work very well, and due to the high Sn content in the Cu-Sn mixture in the core, Cu-Nb-Sn phase form locally in the first one or two filament rows, which is similar to the case of tube type strands; ii), however, the Cu channels among Nb

filaments do work well as shortcuts for Sn diffusion perhaps because Sn can diffuse along the edges of the pores.

It should be mentioned that due to the fast temperature ramp rate, the phase transformations from Cu-Nb-Sn to $NbSn_2$, then to Nb_6Sn_5, and then to Nb_3Sn were delayed to higher temperatures because all of these transformations required incubation time (e.g., for nucleation). In fact, as the temperature just reached 650 °C, FG Nb_3Sn had formed at the periphery of the filaments, as shown by the SE images of the fractured samples in Figure 23.

As can be seen, the Cu-Nb-Sn phase formed at the intermediate temperatures (400-500 °C) finally transformed to CG Nb_3Sn and disconnected Nb_3Sn chunks or particles in the core after reaction, which was also reported in [81]. Thus, by increasing the Cu/Sn ratio in RIT strands, the amount of the disconnected Nb_3Sn particles in the core can still be reduced. However, further increase in FG area fraction is expected to be inconsiderable for the present state-of-the-art RIT strands because the CG Nb_3Sn area fraction is low (typically < 10%). Thus, it can be concluded that the FG area fraction in a subelement of present RIT strands (60-62 %) is quite close to the limit value in Nb_3Sn subelements predicted based on the above model, indicating that there is little room for the improvement of the J_c of RIT strands by way of further improvement of the Nb_3Sn area fraction in the subelements. On the other hand, there is still significant room for improving tube type and PIT strands via reduction of the remaining Nb area and optimization of the precursor compositions to reduce the CG area fractions.

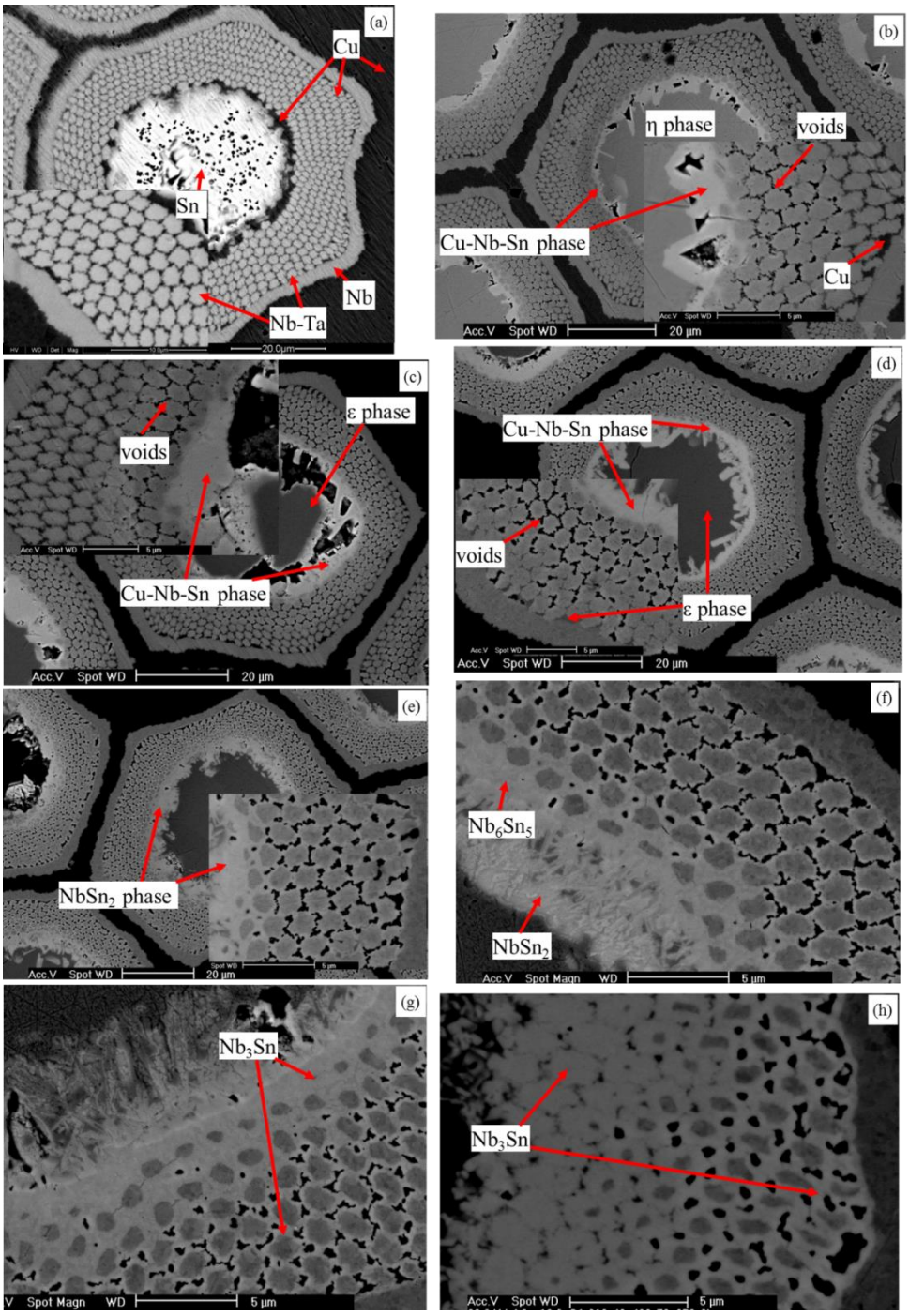

Figure 22. BSE images of a RIT subelement (a) before heat treatment, and (b) after 210°C/48 h+400°C/50 h, (c) reaching 500 °C, (d) reaching 600 °C, (e) reaching 650 °C, (f) after 10 min at 650°C, (g) after 30 min at 650 °C, and (h) after 6 hours at 650 °C.

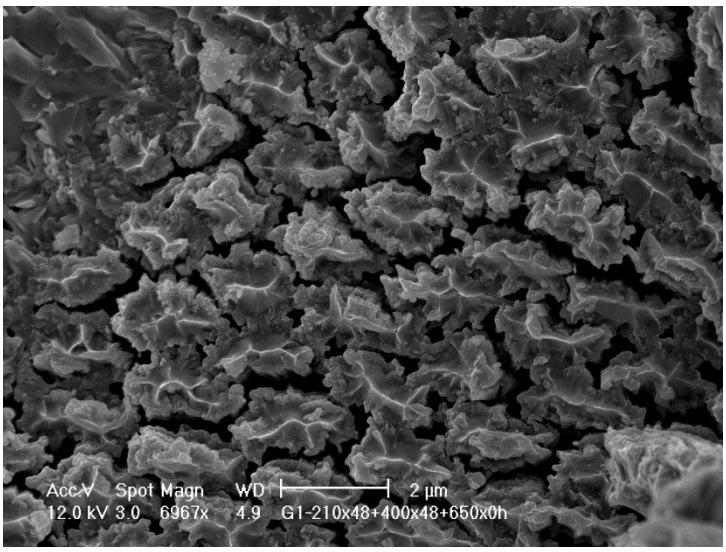

Figure 23. SE image of a fractured subelement as the temperature just reached 650 °C.

That an increase in the Cu/Sn ratio can boost the FG Nb_3Sn area fraction for present tube type strands has been verified by experiments [70]. On the other hand, after measuring the J_cs of two control strands with different Cu/Sn ratios, both reacted at 625 °C, it was found that the one with the higher Cu/Sn ratio had a much lower J_c [70]. This indicates that higher Cu/Sn ratio caused fine-grain Nb_3Sn amount to increase but Nb_3Sn phase quality to drop. As mentioned in section 1.3, the Nb_3Sn layer J_c is mainly determined by the $F_{p,max}$ and B_{irr}, which are further determined by its grain size and composition, respectively. Thus, these properties of the two strands were compared to find out which one was affected by the increased Cu/Sn ratio. The grain sizes of the samples with less Cu and more Cu were almost the same, both around 100-110 nm. On the other hand, it was found that the sample with more Cu had a much lower B_{c2} value, 21.8 T compared with 25.1 T for the sample with less Cu. Since the B_{c2} of Nb_3Sn is

mainly determined by its Sn content, the Sn contents of both samples were measured using EDS, and it turned out that the sample with more Cu indeed had a lower Sn content and a larger Sn at.% gradient [70]. So the reason for the difference in layer J_cs of the two strands could be: higher Cu/Sn ratio led to lower Sn content in the formed Nb_3Sn, which caused lower B_{c2}, which further led to a lower J_c. This brings out another question, why do higher Cu/Sn ratios cause lower Sn content in Nb_3Sn? Or furthermore, what determines the Sn content in the Nb_3Sn formed in a Sn source/Nb_3Sn/Nb diffusion reaction couple? These questions will be answered in chapter 4.

Chapter 4: What determines B_{irr} of Nb_3Sn strands

As discussed in chapter 1, the irreversible field B_{irr} is one of the two major factors deciding the Nb_3Sn-layer J_c of a Nb_3Sn strand, and is especially important for extending the application range of Nb_3Sn conductors to high fields (e.g., 20 T). It is the goal of this chapter to study how to improve the B_{irr} of a Nb_3Sn strand. It has been mentioned in section 1.5 that the most important factor influencing the B_{irr} of Nb_3Sn is its composition. This is critical especially considering that the Nb_3Sn phase formed in a Sn source/Nb_3Sn/Nb diffusion reaction couple during a heat treatment at typically 615-700 °C always has some Sn content gradients [38]. A model is developed in this chapter to explore what determines the Sn content of the Nb_3Sn layer formed in a Sn source/Nb_3Sn/Nb diffusion reaction couple.

4.1. The route to reach the highest B_{irr} of Nb_3Sn

The factors influencing B_{c2} or B_{irr} of Nb_3Sn superconductors have been summarized in section 1.5: apart from the strain state that can hardly be manipulated for B_{c2} improvement, there are two factors that can be optimized via strand design and heat

treatment: doping and Sn content. The questions are, what is the best combination of these factors in order to maximize B_{irr}? And what is the maximum B_{c2}(0 K) of Nb_3Sn?

For binary Nb_3Sn samples, Zhou reported B_{c2}(0.3 K) of 29.2-29.4 T on highly homogeneous bulk samples [55,56], and Orlando reported around 30 T for stoichiometric thin films [48,49]. While Jewell reported 31.4 T on a Cu-free binary bulk sample fabricated via hot isostactic pressing (HIP), this value was obtained from extrapolation of 0-14 T data using the Maki-De Gennes (MDG) relation [82]. Direct resistivity measurements up to 30 T at different temperatures by Godeke gave an onset B_{c2}(0 K) of 29.3 T [1], which is consistent with the direct measurements by J. Zhou. Thus, it can be seen that the B_{c2}(0 K) values of these binary Nb_3Sn samples with optimal Sn contents are 29-30 T, and as pointed out in section 1.5, the optimal Sn content is typically around 24.5 at.%. Godeke's measurement on a binary PIT strand reacted at 675 °C gave a lower onset B_{c2}, 27.8 T [1], which should be due to the sub-stoichiometry of the Nb_3Sn phase in this sample.

Godeke also measured the B_{c2} values of ternary PIT strands reacted at 675 °C and bronze-process strands reacted at 650 °C. The results showed that the onset B_{c2}(0 K) of all the ternary strands were 29-30 T, although the transition width is larger for bronze-process strands and under-reacted PIT strands [1]. Meanwhile, B_{irr} values of Nb_3Sn strands can also be obtained by extrapolating the Kramer plots of transport $J_c(B)$ (after self-correction) to zero, which are 25-26 T for ternary tube type and PIT strands reacted at 615-625 °C [29,70]. Suppose T_c is 17.2 K, then using the MDG relation, it can be estimated that B_{irr}(4.2 K) of 25-26 T corresponds to B_{irr}(0 K) of ~29 T, which is close to

the B_{c2}(0 K) values obtained by Godeke via direct resistivity measurements. It is also worth pointing out that the B_{irr} of Nb_3Sn in those strands mentioned above is somewhat supressed by pre-strain – that is, the intrinsic B_{irr} is expected to be higher than those values.

It is clear that the onset B_{c2}(0 K) values of the ternary strands reacted at 650-675 °C are more or less the same with the binary bulk samples with optimal Sn content, which are 29-30 T. It should be noted, however, that although the two cases attain similar B_{irr} or B_{c2} values, they are different: the Nb_3Sn phase of the tube type and PIT strands reacted at 625-675 °C is sub-stoichiometric (the Sn contents are only 22-23 at.% measured by EDS [1,70]) but with proper ternary additions, while the Nb_3Sn phase of the binary bulk or thin film samples is binary but with optimum Sn content (around 24.5 at.%). A question is, can the B_{irr} or B_{c2} be further increased if the Sn content of ternary or quarternary Nb_3Sn is pushed from 22-23 at.% to stoichiometry? The answer is positive. In fact, as the reaction temperature of ternary RRP or PIT strands was increased to 750 or 800 °C (because increasing reaction temperature is well known to improve Sn content of Nb_3Sn), the 4.2 K B_{irr}s can be pushed up to 28.1 T [57,74], which corresponds to ~32 T for B_{irr}(0 K). B_{c2}(4.2 K) of nearly 29 T, which was measured in a direct magnetic field, was reported on a Ta-doped, RIT mono-element wire with high Sn/Cu ratio reacted at 700 °C [83]. That is to say, there is still room for improvement of B_{irr} for ternary strands by increasing their Sn contents.

So what is the maximum B_{c2} value that Nb_3Sn superconductors can possibly reach? Some high values have been reported before. A B_{c2} value of 31.5 T at 4.2 K (measured in

a direct current field) was reported for a Ga-doped Nb_3Sn thin film fabricated by electron-beam co-evaporation deposition at 700 °C, with a composition of 22.5 at.% Sn and 1.5 at.% Ga addition [7]. In contrast, a control sample with Sn content of 24.8 at.% without Ga addition only had a B_{c2} of 25.4 T at 4.2 K [7]. Another high B_{c2} (0 K) values of up to 35.7 T were achieved on binary bulk samples which were fabricated by reacting ball-milling Nb and Sn powders at 600 °C for 24 hours [8]. Such samples have low T_c (15.1 K), but very large $B_{c2}(T)$ slope (3.34 T/K) [8]. However, these B_{c2} (0 K) values were obtained by extrapolating the B_{c2}-T data from 0-9 T to high fields using the MDG relation.

Here two Ta-doped tube type strands were heat treated at very high temperatures (825 and 875 °C, respectively) to find out the maximum B_{irr} for Nb_3Sn strands. Their transport J_cs at 4.2 K were measured on 5-cm segments, and the B_{irr} values were obtained from their kramer plots shown in Figure 24. For the samples reacted at 825 °C and 875 °C, the Kramer extrapolations gave B_{irr} values of 28.1 T and 30.5 T at 4.2 K, corresponding to 32 and 35 T at 0 K (assuming the T_c is 17.2 K), respectively. However, such B_{irr} values were obtained via extrapolation, and require verification by direct measurements at high fields.

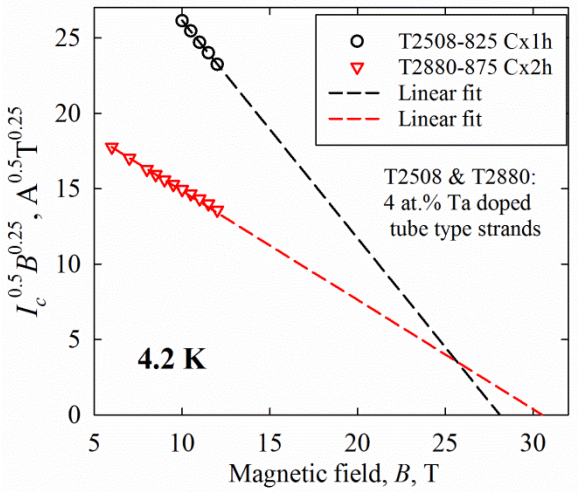

Figure 24. Kramer plots at 4.2 K of tube type strands reacted at very high temperatures.

As discussed in section 1.5, B_{c2}(0 K) of Nb_3Sn is determined by equation 1.11, from which it can be seen that the way to improve B_{c2} of clean Nb_3Sn is to increase the normal state resistivity, which, on the other hand, would decrease the specific heat coefficient γ and critical temperature T_c, so there must be an optimum resistivity and a maximum B_{c2}. Common ways of increasing ρ include off-stoichiometry and doping. A question is, do different disorders have the same influence on B_{c2}? Orlando showed that some disorders follow a universal behavior: there is an optimal ρ_n (which is 20-30 μΩ-cm) that leads to the maximum B_{c2} of ~30 T [49]. If it is true that B_{c2} changes with ρ in a universal way regardless of the types of disorders, then ~30 T must be the maximum B_{c2}(0 K) of Nb_3Sn, judging from the binary samples. However, the extraordinarily high B_{irr} values at 4.2 K (nearly 29 T [83], or even 31.5 T [7]) obtained in the ternary strands or thin films indicate that in fact some disorders (e.g., Ta, Ti, or Ga doping) may have less negative effects on T_c and γ than others (e.g., sub-stoichiometry). For instance, as Sn content of a binary

Nb_3Sn phase is below 24 at.%, its ρ_n is larger than the optimal value and increases as Sn content drops, which explains the decrease in B_{c2} as Sn content drops. However, even in this Sn content regime, Ta or Ti doping, which increases ρ_n, still works very well to improve B_{c2}. For example, Fischer's study on a PIT strand reacted at 675 °C (which is apparently sub-stoichiometric) showed that addition of proper amount of Ta would lead to an increase of B_{irr} by 2 T [57]. This is perhaps because a proper amount of Ta or Ti doping can increase ρ_n without decreasing T_c or γ regardless of the original ρ_n. If this is the case, then a possible route to achieve the highest B_{c2} is to keep Nb_3Sn phase stoichiometric, and let doping do the work of increasing ρ.

In summary, the route to reach the highest B_{irr} of Nb_3Sn is to add proper dopants to stoichiometric Nb_3Sn phase. Present Nb_3Sn strands generally have proper additions because doping can be easily controlled via the additions to the precursors (e.g., Nb-Ta, Nb-Ti, or Sn-Ti); however, all present Nb_3Sn strands reacted at 615-675 °C are sub-stoichiometric. Apparently a fundamental understanding of what controls the Sn content of Nb_3Sn formed in Sn source/Nb_3Sn/Nb diffusion couples is essential so that measures can be worked out to push the Nb_3Sn phase to stoichiometry. Nevertheless, there still lacks such a theory. In the past several decades, the improvement of Sn content has been in a semi-empirical way through experimental studies. It has been found by experiments that the Sn content can be markedly influenced by a few factors, which are summarized below.

First, the starting Sn/Cu ratio can significantly influence the B_{irr}, with lower Sn/Cu ratio leading to smaller B_{irr}s. One of such examples has been shown in Chapter 3.

Another example is that bronze process strands tend to have lower B_{irr} values than RIT and tube type strands. Examples of Sn content profiles for bronze-process and rod-in-tube (RIT) strands are shown in Figure 25.

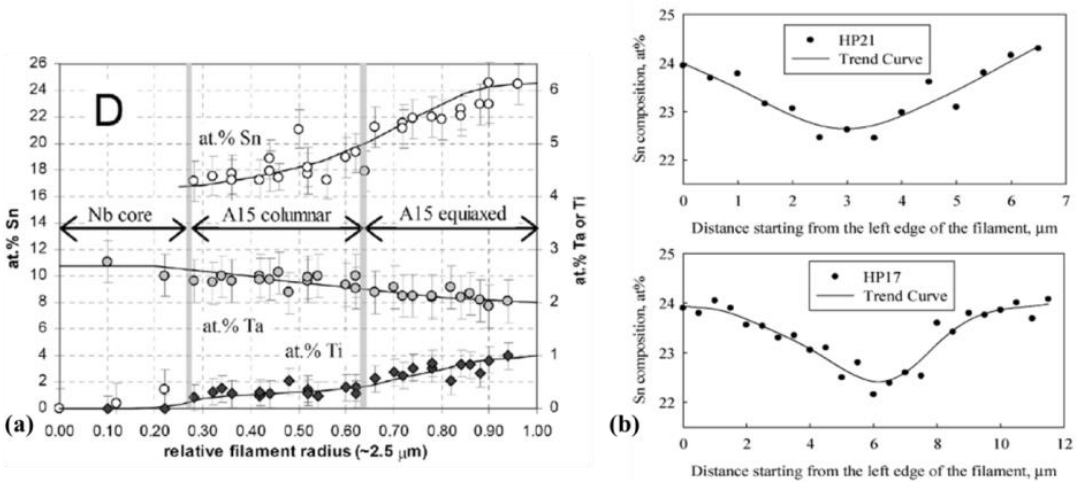

Figure 25. Sn content profiles for Nb_3Sn layers in (a) bronze-process [84] and (b) RIT strands [45].

Previous measurements [1,45,70,84] show that all Nb_3Sn wires have Sn contents above 24 at.% for the Nb_3Sn layer next to the Sn source; however, they have distinct Sn content gradients as the Nb_3Sn layers grow thicker: the bronze-process wires generally have Sn content gradients above 3 at.%/μm [84], while those of the tube type and PIT strands are 0.1-0.2 at.%/μm [1,24,70]. For RRP strands in which original Nb-Ta filaments in each subelement merge to a single Nb_3Sn annulus after reaction, it was found that the Sn content gradients from inner-row filaments to outer-row filaments are quite small (<0.1 at.%/μm) [38]; however, the Sn content gradient within each original filament may be as high as 0.4-0.5 at.%/μm [45]. Such a difference in the Sn content gradients leads to

distinct grain morphologies and superconducting properties. Larger Sn content gradient tends to lead to grains with larger aspect ratio [84]. For instance, the grains in bronze-process wires are generally columnar. Experimental facts indicate that grain boundaries of grains with larger aspect ratios tend to have less pinning efficiency than those of equaixed grains [38,39]. Moreover, experiments also reveal that high-Sn Cu-Sn leads to much higher Nb_3Sn layer growth rate than low-Sn Cu-Sn does [85]. This phenomenon will also be addressed later.

Second, the heat treatment temperature is well known to influence the B_{irr} markedly, with higher Nb-Sn reaction temperature leading to higher Sn content and thus higher B_{irr}. In addition, close analysis indicates that such an influence is not to the same extent for all types of Nb_3Sn strands. The correlation between reaction temperature and Sn content is the most significant for bronze-process strands, and less obvious for rod-restack-process strands, while the influence is the least obvious for tube type and powder-in-tube strands. Figure 26 shows the variation of B_{irr} values obtained by extrapolating the Kramer plots of either transport J_c (after self-correction) or magnetic J_c to zero with heat treatment temperature for RRP strands and tube type and PIT strands.

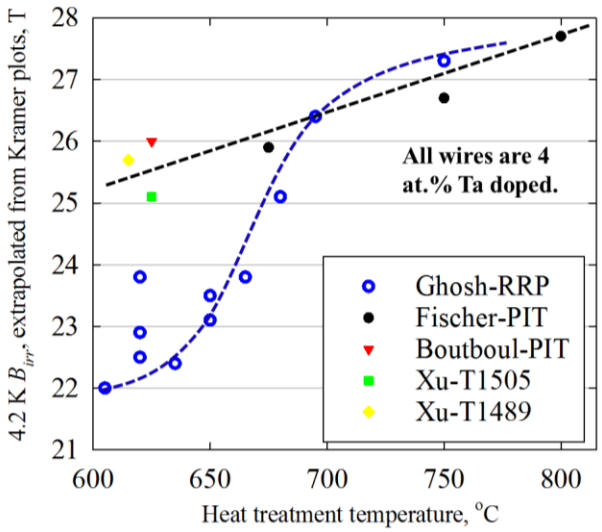

Figure 26. Variation of B_{irr} values with heat treatment temperature for RRP strands [69] and tube type [70] and PIT [29] strands. Except Fischer's PIT strands whose magnetic J_cs were used, the B_{irr}s of other samples were obtained by extrapolating the Kramer plots of transport J_cs (after self-correction) to zero.

As can be seen, for a Ta-doped RRP strand, which starts with much higher Sn/Cu ratio (e.g., 2/3 in molar ratio), the B_{irr} values (which were measured) at 4.2 K increased from 23 T to 25.1 T to 27.3 T as the heat treatment temperature was increased from 620 °C to 680 °C to 750 °C [69]. For tube type and PIT strands, in which Nb_6Sn_5 serves as Sn source before Cu-Sn alloy takes over, 4.2 K B_{irr}s of 25 - 26 T (after self correction) were achieved at a reaction temperature of 615 or 625 °C [29,70], although even higher reaction temperatures could lead to higher B_{irr} (28.1 T for 800 °C) [57]. It can be seen that the B_{irr}s of all Nb_3Sn strands reacted at high temperatures (750-800 °C) are similar (27-28 T at 4.2 K), including bronze-process strands of which the Sn source is bronze with Sn content lower than 10 at.%: for example, the resistivity measurements by Suenaga et al. on Ta or Ti doped bronze-process strands reacted at 725 °C gave 27 T for

the mid-point B_{c2}(4.2 K) values [60]. However, those strands with low-Sn Cu-Sn source tend to have much lower B_{irr}s at low reaction temperatures.

Third, the reaction time can also influence the B_{irr} of a strand, with B_{irr} increasing with reaction extents. Many studies have demonstrated this. For example, Fischer's study on powder-in-tube strands showed that highly under-reacted samples (for both binary and Ta-doped ternary) have B_{irr}s that are only 70-80% of those fully-reacted ones [57]. Experiments on tube type strands also showed a similar increase of B_{irr} with reaction time. One cause for this increase is relief of pre-strain (which is induced by the mismatch in thermal contraction coefficients of different components in the composite wire as it is cooled from the reaction temperature to liquid helium temperature) with reaction time due to increase in the Nb_3Sn layer thickness. Numerous previous experiments have proved that removing the Cu matrix can increase the B_{irr} and T_c of a Nb_3Sn strand markedly [60,74]. On the other hand, Rupp's measurements [86] of intrinsic B_{irr} values, which were obtained by extrapolating the Kramer plots of I_cs at zero intrinsic strain (i.e., the applied tensile strain just balanced the pre-strain) at each field to zero, showed that intrinsic B_{irr} values still increased with reaction time, indicating that relief of the pre-strain with reaction time may not be the only cause for this improvement of superconducting properties with reaction time. Moreover, Smarthers and Larbalestier found that even the bronze is etched off so that the measured samples were solely composed of Nb_3Sn and residual Nb, T_c values still increased significantly with reaction time [87]. Thus, improvement of either the stoichiometry or the long-range order must also contribute to such an increase [34].

Moreover, some other factors have also been found to influence Sn content, too. For example, it was found that Ti doping tends to make decrease Sn content gradient across the Nb_3Sn layer [88]. It was also demonstrated that Zn addition to the Sn source not only enhanced Nb_3Sn layer growth rate, but also increased B_{irr} of the Nb_3Sn strands [89]. Since Zn does not dissolve in Nb_3Sn lattice, it can be speculated that this effect is due to increase in Sn content of Nb_3Sn as Zn is added to the Sn source.

In the above the influence of some factors on the B_{irr} of Nb_3Sn has been discussed. A more fundamental understanding of the diffusion reaction process is, however, required to explore what essentially controls the Sn content of Nb_3Sn in a strand. This theory should of course be able to explain the known facts discussed above. A model will be developed in section 4.2 to address this problem.

4.2. A model for compositions of non-stoichiometric compounds formed in diffusion reactions, and its application to Nb_3Sn

Intermediate phases with finite composition ranges represent a large class of materials, and their compositions may influence their performance in application, as demonstrated in a variety of materials, such as electrical conductivity of oxides (e.g., TiO_{2-y} [90]), electromagnetic properties of superconductors (e.g., Nb_3Sn and $YBa_2Cu_3O_{7-y}$ [91]), and mechanical properties of some intermetallics (e.g., Ni-$Al_{0.4-0.55}$ [92]), etc. For

instance, as discussed in section 1.5, for the superconducting Nb_3Sn phase, which has a composition range of ~17-26 Sn at.% [3,56], the T_c and B_{c2} decrease dramatically as Sn content drops from 24.5 at.% [1,56]. The Nb_3Sn phase, which is formed from Cu-Sn and Nb precursors through reactive diffusion processes, is always found to be Sn-poor (e.g., 22-24 at.% for RIT and PIT strands and 17-24 at.% for bronze-process strands, see Figure 25), making composition control one of the primary concerns in Nb_3Sn development since the 1980s [93]. Although a large number of previous experiments (e.g., [1,38,70]) have uncovered some factors that influence the Sn content, it is still a puzzle what fundamentally determines the Nb_3Sn composition. This work aims to fill that gap. Here it is worth mentioning that the composition interval of a compound layer does not necessarily coincide with its equilibrium phase field ranges – the former can be narrower (e.g., the Nb_3Sn example above) if the inter-phase interface reaction rates are slow relative to the diffusion rate across the compound, which results in discontinuities in chemical potentials at the interfaces.

There have been numerous studies regarding diffusion reaction processes, most of which focused on layer growth kinetics (e.g., [94-98]), compound formations and instabilities (e.g., [96-98]), phase diagram determination (e.g., [99]), and inter-diffusion coefficient measurements (e.g., [100]), while a systematic model exploring how to control the compound compositions is still lacking. We find it indeed possible to modify the model developed by Gosele and Tu [95] for deriving the layer growth kinetics of compounds to calculate their compositions; however, certain assumptions (e.g., steady-state diffusion and first-order interface reaction rates) that the model was based on may

limit the accuracy of the composition results. This section aims to develop a more rigorous, systematic mathematical framework for the compositions of intermediate phases.

Similar to the case of Nb_3Sn, let us consider that a non-stoichiometric A_nB compound is formed in a system of M-B/A, where M is a third element that does not dissolve in A_nB lattice [21]. Here for Nb_3Sn, A stands for Nb, B for Sn, and M for Cu. The use of the third element M is to decrease the chemical potential of B, so that unwanted high-B A-B compounds (e.g., $NbSn_2$ and Nb_6Sn_5 in the Nb-Sn system [3]) that would form in the B/A binary system can be avoided. With the M-B, A_nB, and A-rich phases denoted as α, β, and γ, respectively, a schematic of the α/β/γ system for a planar geometry is shown in Figure 27.

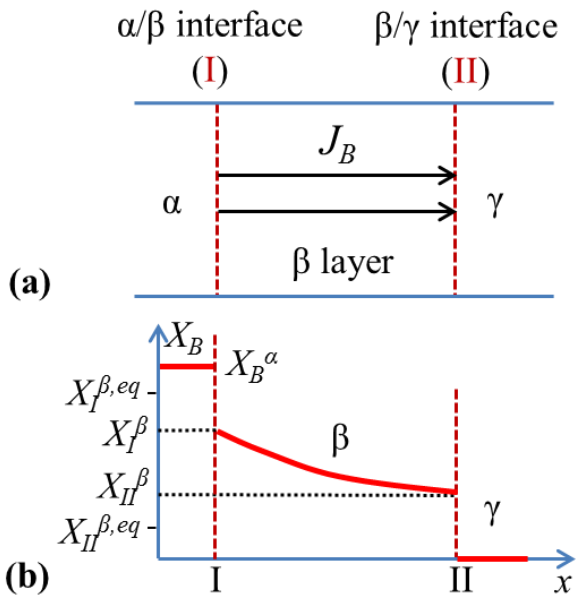

Figure 27. Schematics of (a) an α/β/γ system in the planar geometry, and (b) X_B profiles of the system.

Let us denote the α/β and β/γ inter-phase interfaces as I and II, respectively, and the mole fractions, chemical potentials, activities, and diffusion fluxes of B in the β phase at interfaces I and II as X_I^{β}, μ_I^{β}, a_I^{β}, J_I^{β}, and X_{II}^{β}, μ_{II}^{β}, a_{II}^{β}, J_{II}^{β}, respectively. The maximum and minimum mole fractions of B in the β phase (i.e., A_nB compound) from the phase diagram are set as $X_I^{\beta,eq}$ and $X_{II}^{\beta,eq}$, respectively. Let us also denote the μ_Bs and a_Bs of α and γ as μ_B^{α}, a_B^{α}, and μ_B^{γ}, a_B^{γ}, respectively. Let us assume that the solubility of B in γ phase is negligible, which is the case for Nb_3Sn. An isothermal cross section of such an M-A-B phase diagram at a certain temperature is shown in Figure 28. This is the case we see for the Nb_3Sn example above, but the model below can be modified for other cases. Similar to the Cu-Nb-Sn system, let us assume B is the primary diffusing species in the β phase [101] and that the α phase can act as an intensive sink for B vacancies in order for it to be an efficient source of B atoms for β layer growth, and that the diffusivity of B in α is high so that the α phase remains homogeneous during the growth of β layer [93].

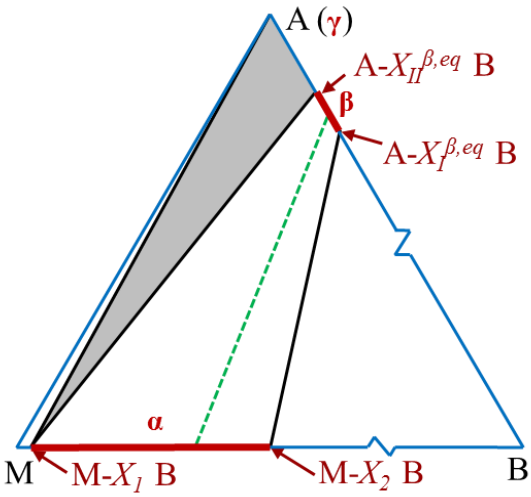

Figure 28. Schematic of an isothermal cross section of the M-A-B ternary phase diagram. The shaded region shows the equilibria among M-X_1 B, A-$X_{II}^{\beta,eq}$ B, and A, and the dashed line shows the equilibrium between α and β (i.e., $\mu_B^{\alpha} = \mu_B^{\beta}$).

Here we assume that diffusion occurs by vacancy mechanism and the total atomic flux is balanced by the vacancy flux. As discussed in the papers by Svoboda and Fischer et al. [102-104], the presence of various types of sinks or sources for vacancies may lead to quite different diffusional and conservation laws and equations. For this model, we assume that B vacancies are generated by the reaction at interface II (as will be discussed in detail later), and then diffuse across the β layer to interface I, where they are annihilated by B atoms from α phase (the B source). For the simplicity of the model, we assume that there are no sinks or sources for vacancies in the bulk or grain boundaries of β phase, while the only sink in the system for B vacancies is the α phase. The following model can be modified for cases with other types of sinks or sources for vacancies using the models by Svoboda and Fischer et al. [102-104].

In this work let us assume the diffusivity of B in β phase, D, and the molar volume of β phase, V_m^{β}, do not vary with X_B, in which case the continuity equation in the β layer is given by:

$$\frac{\partial X_B}{\partial t} = D\frac{\partial^2 X_B}{\partial x^2} \tag{5.1}$$

According to mass conservation, in a unit time the amount of B transferring across interface I should equal to that diffusing into the β layer from interface I, and the amount arriving at interface II should equal to that transferring across it, i.e., $dn/dt|_{\mathrm{I}} = J_I^{\beta}\cdot A_I$, and $dn/dt|_{\mathrm{II}} = J_{II}^{\beta}\cdot A_{II}$, where A_I and A_{II} are the areas of interfaces I and II, respectively. The molar transport rate dn/dt across an interface equals to $r\cdot A_{int}\cdot\exp(-Q/RT)\cdot[1-\exp(-\Delta\mu/RT)]$, where r is the transfer rate constant for this interface with the unit of mol/(m^2·s), A_{int} is the interface area, Q is the energy barrier, R is the gas constant, T is the temperature in K, and $\Delta\mu$ is the driving force for atom transfer. For interface I, $\Delta\mu|_{\mathrm{I}} = \mu_B^{\alpha} - \mu_I^{\beta}$. For interface II, $\Delta\mu|_{\mathrm{II}} = \mu_{II}^{\beta} - \mu_B^{\gamma}$, and $\mu_B^{\gamma} = \mu_B(\mathrm{A}\text{-}X_{II}^{\beta,eq}\ \mathrm{B})$. With $J_B = -(D/V_m)\cdot(\partial X_B/\partial x)$, we have:

$$r_I \exp\left(-\frac{Q_I}{RT}\right)\left[1-\exp\left(-\frac{\mu_B^{\alpha}-\mu_I^{\beta}}{RT}\right)\right] = -\frac{D}{V_m^{\beta}}\frac{\partial X_B}{\partial x}\Big|_I \tag{5.2}$$

$$r_{II} \exp\left(-\frac{Q_{II}}{RT}\right)\left[1-\exp\left(-\frac{\mu_{II}^{\beta}-\mu_B^{\gamma}}{RT}\right)\right] = -\frac{D}{V_m^{\beta}}\frac{\partial X_B}{\partial x}\Big|_{II} \tag{5.3}$$

Eqs. (5.2) and (5.3) are the boundary conditions for Eq. (5.1). Note that X_B in α phase, X_B^{α}, drops with annealing time as B in α is used for β layer growth, so μ_B^{α} drops with t:

$$\frac{d\mu_B^{\alpha}}{dt} = \frac{d\mu_B^{\alpha}}{dX_B^{\alpha}}\frac{dX_B^{\alpha}}{dt} = -\frac{d\mu_B^{\alpha}}{dX_B^{\alpha}}\frac{n_M}{\left(n_M + n_{B0} - \int_t dn/dt\big|_I\right)^2}\frac{dn}{dt}\Big|_I \tag{5.4}$$

where n_M and n_{B0} are the moles of M and B in the M-B precursor. For those systems without the third element or μ_B^{α} is constant (for example, as Nb_6Sn_5 serves as Sn source), and Eq. (5.4) is not needed. In addition, since the B atoms diffusing to interface II are used to form new β layers, we have:

$$\frac{dl}{dt} = \frac{J_{II}^{\beta} V_m^{\beta}}{X_{II}^{\beta}} = -\frac{D}{X_{II}^{\beta}} \frac{\partial X_B}{\partial x}\Big|_{II} \tag{5.5}$$

Eqs. (5.1)-(5.5) are the governing equations for the system set up above, solutions to which give both the $X_B(x, t)$ and the $l(t)$ of a growing A_nB layer. It should be noted that for the systems with large volume expansion associated with transformation from γ to β, stress effects need to be considered [105].

To simplify Eqs. (5.2) and (5.3), we notice that $1\text{-}\exp[-(\mu_B^{\alpha}-\mu_I^{\beta})/RT] = 1-a_I^{\beta}/a_B^{\alpha}$, since $\mu_B^{\alpha}-\mu_I^{\beta} = RT\ln(a_B^{\alpha}/a_I^{\beta})$; similarly, $1\text{-}\exp[-(\mu_{II}^{\beta}-\mu_B^{\gamma})/RT] = 1-a_B^{\gamma}/a_{II}^{\beta}$. Let us also denote $D/[V_m \cdot r_I \cdot \exp(-Q_I/RT)]$ as φ_I, and $D/[V_m \cdot r_{II} \cdot \exp(-Q_{II}/RT)]$ as φ_{II}: clearly φ_I and φ_{II} represent the ratios of diffusion rate over interface reaction rates, and have a unit of meter. Then Eqs. (5.2) and (5.3) can be respectively written as:

$$1-\frac{a_I^{\beta}}{a_B^{\alpha}} = -\varphi_I \frac{\partial X_B}{\partial x}\Big|_I \tag{5.6}$$

$$1-\frac{a_B^{\gamma}}{a_{II}^{\beta}} = -\varphi_{II} \frac{\partial X_B}{\partial x}\Big|_{II} \tag{5.7}$$

To solve the equation set, let us first consider two extreme cases. First, for the case that the interface reaction rates are much higher than the diffusion rate across the β layer (i.e., diffusion-rate limited), φ_I and φ_{II} are near zero; according to Eqs. (5.2)-(5.3), μ_Bs are continuous at both interfaces, so $X_{II}^{\beta} = X_{II}^{\beta,eq}$. Suppose μ_B^{α} and the position of interface I,

x_I, are both constant with time, then X_I^{β} is also constant, and the solutions to Eqs. (5.1) and (5.5) are respectively $X_B(x, t) = X_I^{\beta}-(X_I^{\beta}-X_{II}^{\beta,eq})\cdot\mathrm{erf}\{(x-x_I)/[2\sqrt{(Dt)}]\}/\mathrm{erf}(k/2)$ and $l=k\sqrt{(Dt)}$ for the β layer, where k can be numerically solved from $k\cdot\exp(k^2/4)\cdot\mathrm{erf}(k/2) = 2/\sqrt{\pi}\cdot(X_I^{\beta}-X_{II}^{\beta,eq})/X_{II}^{\beta,eq}$. For instance, for $X_I^{\beta} = 0.26$ and $X_{II}^{\beta,eq} = 0.17$, k=0.953. On the other hand, if the interface reaction rates are much lower than the diffusion rate across β (e.g., as the β layer is thin), φ_I and φ_{II} are large; according to Eqs. (5.2)-(5.3), X_B and J_B are nearly constant in the entire β layer. Thus, $(1-a_B/a_B^{\alpha})/\varphi_I = (1-a_B^{\gamma}/a_B)/\varphi_{II}$, from which a_B can be calculated. Integration of Eq. (5.5) gives: $l \propto t$, and the pre-factor depends on the interface reaction rates.

For a general case between these two extremes, the equations can only be solved with the $\mu(X)$ relations of α and β provided. Next, let us consider a compound with a narrow composition range, so that as a Taylor series expansion is performed around $X_{II}^{\beta,eq}$ for its $a(X_B)$ curve, high-rank terms can be neglected because $|X- X_{II}^{\beta,eq}| \le (X_I^{\beta,eq} - X_{II}^{\beta,eq})$ is small. Because the γ phase is in equilibrium with A-$X_{II}^{\beta,eq}$B, we have $a_B^{\gamma} = a_B$(A-$X_{II}^{\beta,eq}$B); thus, $a_X \approx a_B^{\gamma} + \kappa(X- X_{II}^{\beta,eq})$, where κ is the linear coefficient of the $a(X)$ curve. Given the complex boundary conditions for Eq. (5.1), to obtain the analytic solutions we introduce a second approximation if the β composition range is narrow: the $X(x)$ profile of the β layer is linear so that at a certain time J is constant with x, such that $-(\partial X_B/\partial x)|_I \approx -(\partial X_B/\partial x)|_{II} \approx (X_I^{\beta}-X_{II}^{\beta})/l$. With these two approximations, we can solve Eqs. (5.6)-(5.7) and obtain that:

$$a_{II}^{\beta} = \frac{\sqrt{(\varphi_I a_B^{\alpha} + \kappa l - \varphi_{II} a_B^{\alpha})^2 + 4\varphi_{II} a_B^{\gamma}(\varphi_I a_B^{\alpha} + \kappa l)} - (\varphi_I a_B^{\alpha} + \kappa l - \varphi_{II} a_B^{\alpha})}{2\varphi_{II}}$$
$$= \frac{2a_B^{\gamma}}{1-\eta+\sqrt{(1-\eta)^2 + 4\eta\, a_B^{\gamma}/a_B^{\alpha}}} \qquad (5.8)$$

where $\eta=\varphi_{II}a_B{}^{\alpha}/(\varphi_I a_B{}^{\alpha}+\kappa l)$. Then $a_I{}^{\beta}$ can be calculated from $a_{II}{}^{\beta}$, and $X_I{}^{\beta}$ and $X_{II}{}^{\beta}$ can be calculated from $a_I{}^{\beta}$ and $a_{II}{}^{\beta}$ using $X = X_{II}{}^{\beta,eq} +(a_X- a_B{}^{\gamma})/\kappa$.

To verify the results, the equations are solved for a hypothetical system analytically and numerically, with and without the assumption that $X(x)$ profile of the A_nB layer is linear, respectively. The obtained composition profiles are shown in Figure 29. For simplicity, $\mu_B{}^{\alpha}$ of the system is set as μ_B(A-$X_I{}^{\beta,eq}$ B) and is constant (for Nb_3Sn systems, this means that Nb_6Sn_5 serves as Sn source), and the other parameters are specified in the figure. The difference between the analytic and numerical solutions is <0.1%, showing that the approximation of linear $X(x)$ is good if the composition range is small (2 at.% in this case).

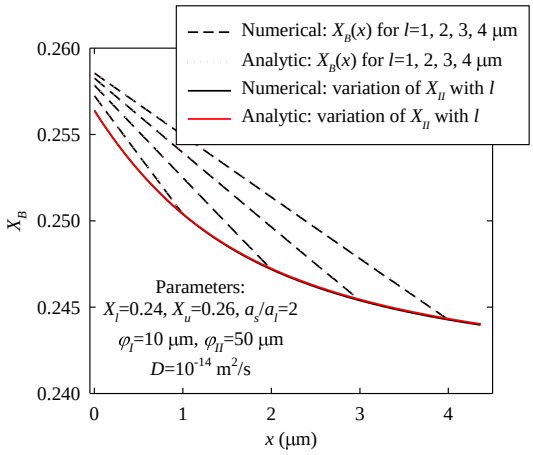

Figure 29. The calculated $X_B(x)$ profiles of the hypothetical system for the analytic and numerical solutions, with and without the assumption that $X_B(x)$ is linear, respectively.

The $l(t)$ result (where t is the annealing time after the incubation period) from the numerical calculations is shown in Figure 30. While the analytic $l(t)$ solution is complicated, some $l(t)$ relations with simple forms can be used as approximations. The most widely used $l(t)$ relation for the case of constant μ_B^{α} is $l=bt^m$, in which m=1 for reaction-rate limited and m=0.5 for diffusion-rate limited; however, a defect with this relation is that as l increases from zero, it may shift from reaction-rate limited to diffusion-rate limited, so m may vary with t. Here a new relation $l=q[\sqrt{(t+\tau)}-\sqrt{\tau}]$, which also has only two fitting parameters (q is a growth constant and τ is a characteristic time), is proposed. Such a relation is consistent with $l^2/v_1+l/v_2=t$ (where v_1 and v_2 are constants related to diffusion rate and interface reaction rates, respectively) proposed by previous studies [95,96]. This relation overcomes the above problem because as $t << \tau$, $l=[q/(2\tau)]\cdot t$ and as $t >> \tau$, $l=q\sqrt{t}$. As can be seen from Figure 30, a better fit to the numerical $l(t)$ curve in the whole range is achieved by $l=q(\sqrt{(t+\tau)}-\sqrt{\tau})$.

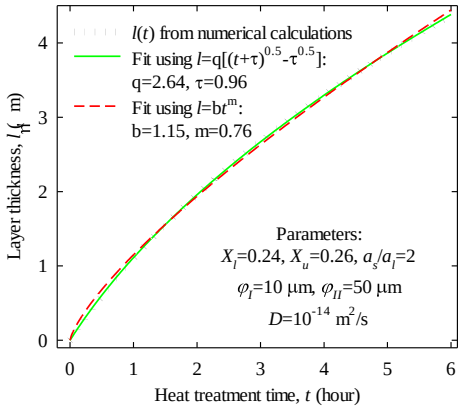

Figure 30. The $l(t)$ results for the hypothetical system from the numerical calculations, with the fits of $l=q[\sqrt{(t+\tau)}-\sqrt{\tau}]$ and $l=bt^{m}$.

Before discussing the application of this model to a specific material system, it must be pointed out that all of the analysis and calculations above are for the case that B diffuses through the β layer via bulk diffusion. In such a case, for an α/β/γ system, as μ_B^{α} drops with the growth of β layer, $X_B(x)$ of the entire β layer should decrease with μ_B^{α}, because $\mu_B^{\alpha} \geq \mu_I^{\beta} \geq \mu_{II}^{\beta} \geq \mu_B^{\gamma}$. Finally, one of two cases will occur: if γ is in excess in the α/β/γ diffusion reaction system, μ_B^{α} drops to μ_B^{γ} (the μ_B profile of the system is shown in Figure 31 a), so the system ends up with the equilibrium among γ, A-$X_{II}^{\beta,eq}$ B, and M-X_1 B (as shown by the shaded region in the isothermal M-A-B phase diagram in Figure 28); if the B source (i.e., α is in excess), then γ would eventually be consumed up and β gets homogenized with time and finally $\mu_B(\beta)=\mu_B(\alpha)$ (the μ_B profile of the system is shown in Figure 31 b), with the phase equilibrium shown by the dashed line in Figure 28. In either case, β layer eventually reaches homogeneity.

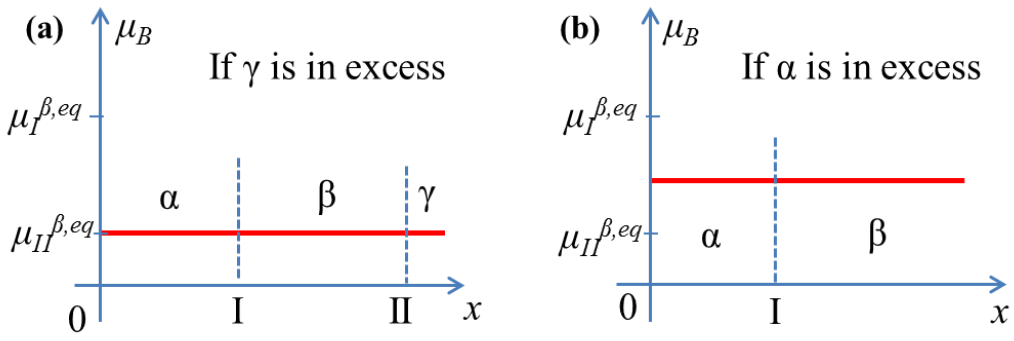

Figure 31. Schematics of μ_B profiles for the α/β/γ diffusion reaction system after reaching equilibrium for the case (a) γ is in excess and (b) B source is in excess.

However, it is found that the composition could be different for a compound in which the bulk diffusion is low while grain boundary diffusion dominates. One such example is Nb_3Sn, the composition of which displays some extraordinary features. As an illustration, the X_{Sn}s of a single-barrier internal-tin strand after annealing times of 65 h, 130 h, 320 h, and 600 h at 650 °C are shown in Figure 32. The initial composition of Cu-Sn alloy after the mixing heat treatment was Cu-12 at.% Sn. Clearly, as the X_{Sn} (and μ_{Sn}) of Cu-Sn drop with time, the X_{Sn}s of Nb_3Sn do not drop accordingly; instead, they more or less remain constant with time. In addition, from 320 hours to 600 hours, although Nb has been fully consumed, the X_{Sn} of Nb_3Sn does not homogenize (i.e., the X_{Sn} gradient does not decrease) with annealing time.

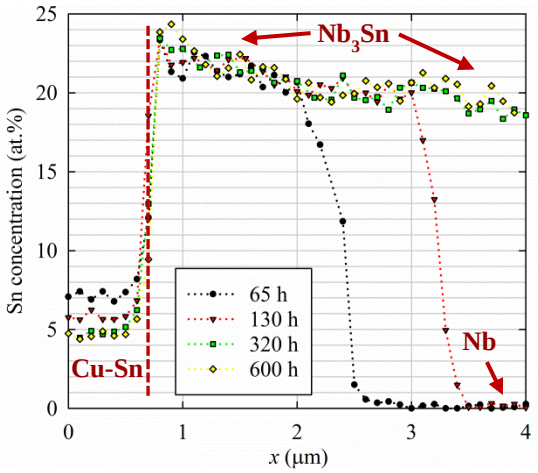

Figure 32. The X_{Sn}s of a Cu-Sn/Nb_3Sn/Nb system after various annealing times at 650°C. The measurement error in the Sn content is around 0.5 at.%.

In many other studies on PIT and tube type subelements in which Nb is in excess (e.g., [1,70]), even after extended annealing times after the Nb_3Sn layers have finished growing (which indicates that the Sn sources have been depleted, i.e., μ_{Sn}s have dropped to μ_{Sn}^{γ}, as shown in Figure 31 a), X_{Sn}s of Nb_3Sn remain high above $X_{II}^{\beta,eq}$, without dropping with annealing time. An example of a PIT strand reprinted from [1] is shown in Figure 33. As can be seen, as the reaction time was extended from 64 to 768 hours, the Nb_3Sn layer thickness did not grow, indicating that μ_{Sn}s have dropped to μ_B^{γ}; however, the Sn content of Nb_3Sn remained at around 22 at.%, far above the $X_{II}^{\beta,eq}$ of ~17 at.%.

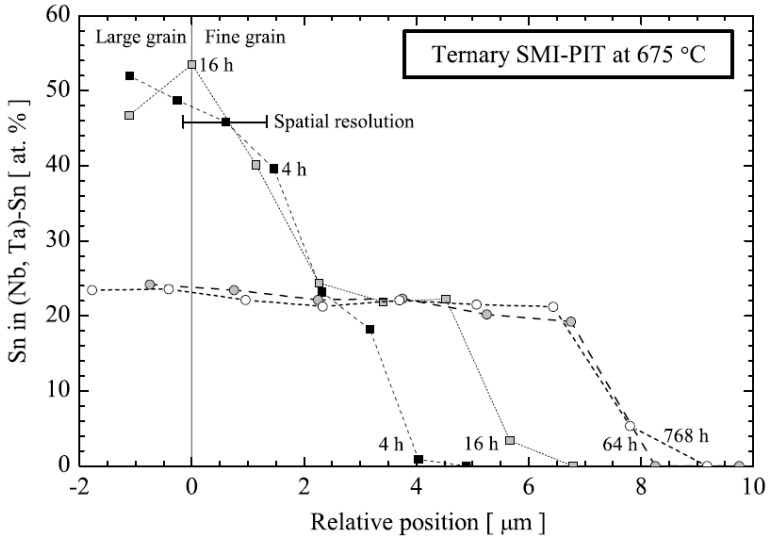

Figure 33. Compositions of a PIT strand reacted at 675 C for various times [1].

The reason for these peculiarities is that grain boundary diffusion in Nb_3Sn dominates due to extremely low bulk diffusivity and small Nb_3Sn grain size (~100 nm). For example, it was reported in [106] that the bulk diffusivity of Sn in Nb_3Sn is lower than 10^{-23} m^2/s at 650 °C. Using the relation $l \approx \sqrt{DT}$ to estimate the diffusion distance, it can be seen that the diffusion distance is less than 0.1 nm even for a duration of 1000 hours at 650 °C. Instead, the diffusivity of Sn along Nb_3Sn grain boundaries is several magnitudes higher than that in the bulk [106]. In this case, the above model and equilibrium-state analysis apply only to the diffusion zones (i.e., the grain boundaries and the inter-phase interfaces) instead of the bulk. To clarify this point more clearly, a schematic of the diffusion reaction process is shown in Figure 34.

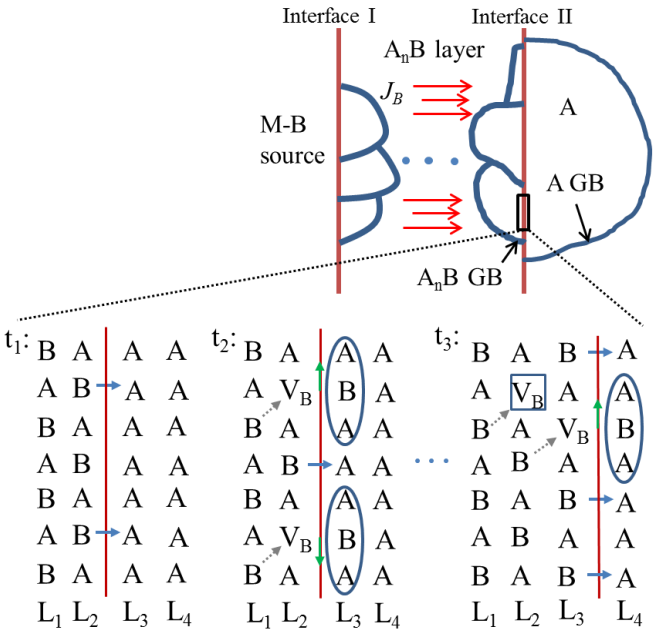

Figure 34. A schematic of the diffusion reaction process for grain boundary diffusion.

At time t_1, at the β/γ interface, high-B A_nB (L_2 layer) reacts with γ (L_3 layer) to form some new A_nB cells, leaving B vacancies (noted as V_Bs) in L_2 layer (time t_2). If bulk diffusivity is high, V_Bs simply diffuse through bulk (e.g., from L_2 to L_1, as shown by grey dotted arrows) to the B source. If bulk diffusion is frozen, the V_Bs diffuse first along β/γ inter-phase interface (as shown by green solid arrows), and then along β grain boundaries to the B source. This process continues until this L_3 layer entirely becomes A_nB (time t_3), so the reaction frontier moves ahead to L_3/L_4, while the L_2/L_3 interface now becomes an inter-plane inside A_nB lattice. If bulk diffusion is completely frozen, the V_Bs in the L_2 layer that have not diffused to the B source will be frozen in this layer forever, and will perhaps transform to A-on-B anti-site defects later (e.g., for Nb_3Sn, Nb-on-Sn anti-sites are more stable than Sn vacancies [107]). Since these point defects determine the A_nB

composition, the X_B in this L_2 layer cannot change anymore regardless of μ_B variations in grain boundaries. That is to say, X_B of any point is just the X_{II}^{β} of the moment when the reaction frontier sweeps across this point, i.e., the $X_B(x)$ of the β layer is simply an accumulation of X_{II}^{β}s with l increase. Returning to Figure 29, the dashed lines display the evolution of $X_B(x)$ with l increase for bulk diffusion, while that for grain boundary diffusion is shown by the solid lines. Since the EDS attached to scanning electron microscopes (SEM) that is used to measure the compositions typically has a spatial resolution of 0.5-2 μm, and thus mainly reflects the bulk composition, the unique composition characteristics of Nb_3Sn layers as described above can be explained.

It should be noted that awareness of the influence of frozen bulk diffusion and of the difference between bulk diffusion and grain boundary diffusion on the bulk composition is important in controlling the final composition of a compound. For instance, if bulk diffusivity is high, one method to form high-B A_nB is increasing the starting B/A ratio so that after long annealing time for homogenization subsequent to the full consumption of γ, μ_B(M-B)=μ_B(A-$X_{II}^{\beta,eq}$B). To realize this for Nb_3Sn, first a subelement needs to start with sufficient Sn to make its Sn/Nb ratio much larger than 1/3. Second, measures must be taken to avoid Sn leaking to the outside Cu matrix after Nb is reacted through – for example, a Ta barrier between the Nb and the outside Cu can impede Sn leakage to a certain extent. To verify whether this method can really form high-Sn Nb_3Sn, a tube type monofilament with very high Sn/Nb ratio (1/2.6 in atomic ratio) was fabricated, BSE image of which is shown in Figure 35. The outside Cu matrix was etched off so that it would not consume the excess Sn. After a reaction at 650 °C for 170 hours, all the Nb-Ta

had been transformed to Nb_3Sn, while there was still Nb_6Sn_5 phase in the core, as shown in Figure 35 (b). However, by further prolonging the reaction time to 300 hours, we found that the Sn content of Nb_3Sn did not increase with reaction time, that is, it was not enriched by the excess Nb_6Sn_5. Furthermore, it turned out that the final Sn content of this Sn-excess strand was of no difference with a control strand with small Sn/Nb ratio such that Nb was in excess. This experiment demonstrates that for compounds with low bulk diffusivity (e.g., Nb_3Sn), once a compound layer has formed, it is impossible to change its composition afterwards anymore; instead, controlling the X_{II}s during the growth of the compound layer is the only way. For those compounds with low but non-negligible bulk diffusivities, their compositions would be between these two extremes.

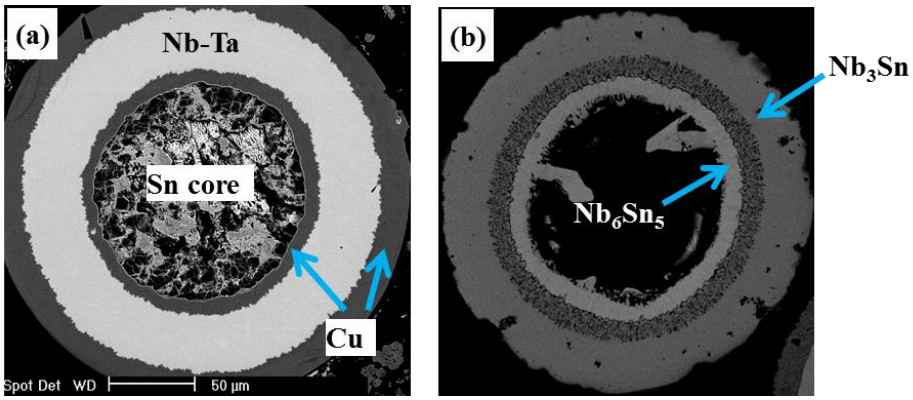

Figure 35. The Sn-rich monofilament: (a) in the green state and (b) after being fully etched and reacted at 650 °C for 170 hours. Note that the smears in the Sn core of the green-state wire were from polishing.

Then what determines the bulk composition as grain boundary diffusion dominates? From Figure 34, it can be clearly seen that there is a competition deciding the V_B fraction in the frontier A_nB layer: at t_2 the reaction across the β/γ interface produces V_Bs in L_2

layer, while the diffusion of B along β grain boundaries and α/β interface fills these V_Bs. Thus, if the diffusion rate is slow relative to the reaction rate at interface II (i.e., φ_{II} is low), a high fraction of V_Bs would be left behind as the interface II moves ahead, causing low B content; if, on the other hand, the diffusion rate is high relative to the reaction rate at interface II, the A_nB layer has enough time to get homogenized with the B source, causing low X_B gradient. In this case, the μ_B of B source and the reaction rate at interface I together set a upper limit for μ_B of β.

Next, we will modify the above model for the case of grain boundary diffusion for quantitative analysis. As pointed out earlier, the chemical potentials of grain boundaries can change with μ_B^{α} and l, while those of the bulk cannot. In such a case, μ_I^{β} and μ_{II}^{β} (suppose the diffusivities along the inter-phase interfaces are large) can still be calculated using the above model, provided that the $\mu(X)$ relation and D of the β grain boundary (instead of the bulk) are used in all of the equations, and that φ_I and φ_{II} are multiplied by a factor of $\sum A_{GB}/A_{int}$ (where $\sum A_{GB}$ is the sum of the cross section areas of the grain boundaries projected to the inter-phase interfaces), because B diffuses only along β grain boundaries while reactions occur at the entire interfaces. Approximately, $\sum A_{GB}/A_{int} \approx [1-d^2/(d+w)^2] \approx 2w/d$ (where w is the β grain boundary width, and d is the grain size). Apparently, grain growth with annealing time reduces the diffusion rate.

According to equation (5.8), a_{II}^{β} is determined by η and a_B^{α}, and increases with them, as shown by Figure 36. Since $\eta=\varphi_{II}a_B^{\alpha}/(\varphi_I a_B^{\alpha}+\kappa l)= 1/[\varphi_I/\varphi_{II}+\kappa l/(\varphi_{II}a_B^{\alpha})]$, clearly η decreases as φ_I/φ_{II} and l increase. As l=0, $\eta=\varphi_{II}/\varphi_I$; thus, to improve a_{II}^{β} of A_nB at l=0, one should increase μ_B^{α} and the reaction rate at interface I, and reduce the reaction rate at

interface II. At a certain l, it is clear that increase in φ_{II} or decrease in φ_I (which means improving the diffusion rate, or improving the reaction rate at interface I, or reducing the reaction rate at interface II) leads to increase in a_{II}^{β}, which means reduction in a_B^{β} gradient. Apparently, these quantitative conclusions are consistent with the above qualitative analysis. Meanwhile, from equation (5.8) and Figure 36, it can be calculated that at a certain l and φ_{II}/φ_I, increase in a_B^{α} leads to increase in both (a_B^{α} - a_{II}^{β}) and (a_{II}^{β}-a_B^{γ}), which means that increase in activity of B in B source causes increase in both diffusion rate across the β layer and increase in reaction rate at β/γ interface.

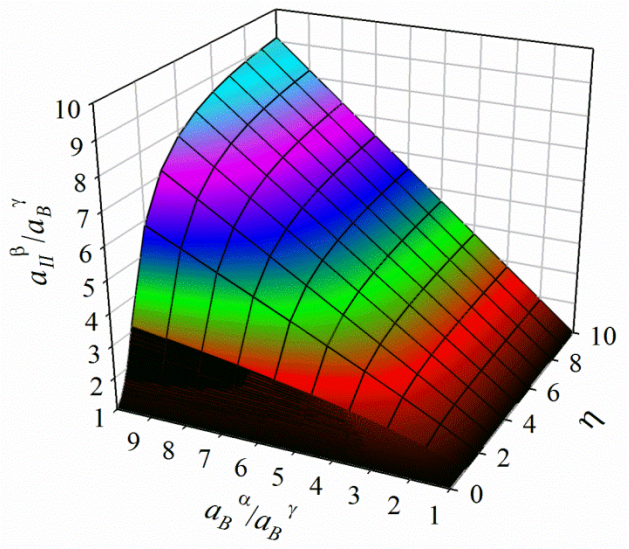

Figure 36. The variation of a_{II} with η and a_B^{α}, according to Equation 5.8.

Next let us compare this model with the example of Nb_3Sn, and use it to explain the empirical factors that influence the Sn content of Nb_3Sn strands, as discussed in section 5.1. It has been mentioned in section 5.1 that there are mainly three factors that can

significantly influence the Sn content of Nb_3Sn in a Sn source/Nb_3Sn/Nb diffusion reaction couple: Cu-Sn source, heat treatment temperature and time.

For the first factor, Cu-Sn source, as mentioned in section 5.1, all types of strands have Sn contents above 24 at.% for the Nb_3Sn layer next to the Cu-Sn source; however, they have distinct Sn content gradients as the Nb_3Sn layers grow thicker: bronze-process strands with low-Sn Cu-Sn as Sn source generally has Sn content gradients above 3 at.%/μm [84], while those of RRP, PIT, and tube type strands are below 0.5 at.%/μm [45]. Such a difference in the Sn content gradients leads to distinct grain morphologies and superconducting properties. To explain the phenomenon that different wires have similar X_{Sn} in the Nb_3Sn layer next to the Cu-Sn source, the relation between μ_{Sn}(Cu-Sn) and μ_{Sn}(Nb-X_{Sn} Sn) is required. The Cu-Sn system has been well studied, and the phase diagram calculated by the CALPHAD technique using the thermodynamic parameters given by [108] is well consistent with the experimentally measured diagram [109]. Thus, the parameters from [108] are used to calculate μ_{Sn} of Cu-Sn, which is shown in Figure 37. On the other hand, although thermodynamic data of Nb-Sn system were proposed by [108] and [110], in these studies Nb_3Sn was treated as a line compound. However, some information about μ_{Sn} of Nb_3Sn can be inferred from its relation with μ_{Sn} of Cu-Sn: since Cu-7 at.% Sn leads to the formation of Nb-24 at.% Sn near the Cu-Sn source [84], we have μ_{Sn}(Cu-7 at.% Sn) $\geq$ μ_{Sn}(Nb-24 at.% Sn). Thus, the expected approximate μ_{Sn}(Nb-X_{Sn} Sn) curve in a power function is shown in Figure 37. Furthermore, it can also be inferred that the Sn transfer rate at the Cu-Sn/Nb_3Sn interface must be much faster than that at the Nb_3Sn/Nb interface, so μ_{Sn} discontinuity across the interface I is small. These

explain why low-Sn Cu-Sn can lead to the formation of high-Sn Nb_3Sn. It is worth mentioning that from Figure 37, it is clear that the Taylor series for the true $a(X)$ relation of Nb_3Sn have more high-rank terms than $a(X) \approx a_B^{\gamma} + \kappa(X\text{-}X_{II}^{\beta,eq})$; however, our numerical calculations show that adding high-rank terms to the $a(X)$ relation does not lead to different conclusions regarding the influences of a_B^{α}, φ_I, φ_{II}, and l on X_{II}^{β}. Thus, the above qualitative and quantitative analysis still applies.

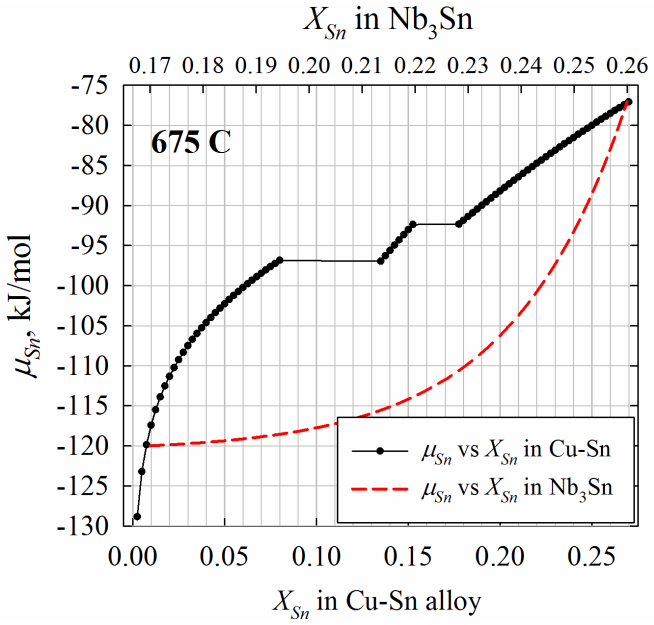

Figure 37. The variation of μ_{Sn} with X_{Sn} for Cu-Sn calculated based on thermodynamic data given in [108], and a rough $\mu_{Sn}(X_{Sn})$ relation for Nb_3Sn speculated according to the phase formation relation between Cu-Sn and Nb_3Sn.

The other phenomenon, the different X_{Sn} gradients in the strands with high-Sn and low-Sn Cu-Sn sources, can also originate from the unique μ_{Sn}-X_{Sn} relation for Nb_3Sn. A schematic of the μ_B profiles of the α/β/γ system for two different B sources is shown in

Figure 38 (a). It has been mentioned earlier that larger μ_B in the B source causes both larger $\Delta\mu_B$ across the β layer and larger (μ_{II}^{β}–μ_B^{γ}), which cause larger diffusion rate and larger reaction rate, respectively. This explains why the Nb_3Sn layer growth rate in high-Sn strands (e.g., RRP, PIT, and tube type strands) is much higher than that in low-Sn strands (e.g., bronze-process strands). Figure 38 (b) shows a schematic of the X_{Sn}-μ_{Sn} plot of Nb_3Sn from Figure 37, and the X_{Sn} width caused by the μ_{Sn} width across the Nb_3Sn layer for the two cases shown in Figure 38 (a). As can be seen, although higher μ_B^{α} causes higher $\Delta\mu_{Sn}$ across the Nb_3Sn layer, ΔX_{Sn} is smaller due to the unique X_{Sn}-μ_{Sn} relation of Nb_3Sn, explaining why low-Sn strands have high Sn at.% gradient. It may also need further investigation regarding whether Cu-Sn source can also influence diffusion rates in Nb_3Sn layer (e.g., via thermodynamic factor), because greater D leads to greater φ_{II}, which helps decreasing X_{Sn} gradients.

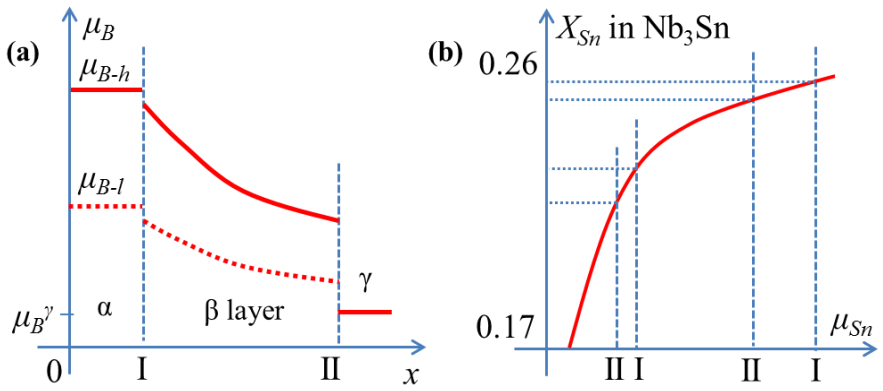

Figure 38. (a) Schematic of the μ_B profiles of the system for two different B sources, and (b) schematic of the X_{Sn} width caused by the μ_{Sn} width across the Nb_3Sn layer.

The second factor, heat treatment temperature, can simultaneously influence multiple factors of Equation (5.8). such as a_B^{α}, D, and reaction rates at both interfaces, etc. Moreover, from the thermodynamics point of view, $\mu_{Sn}(X_{Sn})$ of Cu-Sn and $\mu_{Sn}(X_{Sn})$ relation of Nb_3Sn may also change with temperature. As mentioned above, at low reaction temperatures, Sn source can lead to quite different Sn content gradients, but high reaction temperature overcomes this difference and makes their Sn contents equally high. This perhaps indicates that the plateau regime in the X_{Sn}-μ_{Sn} curve of Nb_3Sn extends to much lower μ_{Sn} regime (that is, the μ_{Sn}-X_{Sn} curve bends more severely) at high temperatures. This, however, requires further confirmation. Moreover, the equilibrium between Cu-Sn and Nb_3Sn may also be different from Figure 37 at a temperature other than 675 °C. For example, it was found in Ref. [111] that the minimum Sn content of Cu-Sn alloy needed to form Nb_3Sn drops with reaction temperature. This indicates that the region of Cu-Sn that is in equilibrium with Nb and Nb- $X_{II}^{\beta,eq}$ Sn shifts to the Cu-rich corner as temperature is increased. Thus, at higher reaction temperatures, even low-Sn Cu-Sn can be in equilibrium with high-Sn Nb_3Sn. Second, on the kinetics point of view, change of reaction temperature leads to variation in the diffusivity of Sn in Nb_3Sn grain boundary, grain size, and reaction rates at both interfaces, etc. In conclusion, the explanation of the influence of temperature on Sn contents using this theory requires knowledge of the quantitative variations of the factors in Equation (5.8) with temperature, and requires further studies, which are beyond the scope of this dissertation.

Another factor that has been demonstrated to significantly influence B_{irr} of Nb_3Sn wires is reaction time – both T_c and B_{irr} of Nb_3Sn wires have been found to increase with

reaction time during the growth of Nb_3Sn layer at an isothermal heat treatment. As mentioned in section 5.1, this is partly due to relief of the pre-compression strain that originates from the mismatch in the thermal contraction coeffients of different components in the composite: such a strain can markedly degrade B_{irr} of Nb_3Sn phase. This strain is remarkably larger for thin Nb_3Sn layers, and as Nb_3Sn layer grows thicker, the strain becomes smaller. This is, however, not the only cause. There are two more possible reasons for the increase of T_c and B_{irr} with reaction time. First, although the bulk diffusivity of Sn in Nb_3Sn is small, it is not zero, so there is still some Sn leakage from Nb_3Sn grain boundaries to grain interior as Sn flux diffuses along Nb_3Sn grain boundaries, and this enriches the Sn content of bulk Nb_3Sn with reaction time. Since the change of B_{irr} with Sn content is very sensitive (5-6 T/ at.% Sn), even a small Sn content increase that is within the data error range of EDS measurements is significant enough to cause a remarkable increase in B_{irr}. However, even if this effect does exist, the increase of Sn content with reaction time must be a very sluggish process, as can be seen from the above Sn-rich monofilament experiment. The second possibility is, whether the Sn flux along Nb_3Sn grain boundaries leaks into grain interior to enrich bulk Nb_3Sn or not, the Nb_3Sn lattice of bulk Nb_3Sn undergoes some change (or self-organization) at elevated temperatures with reaction time. For example, a neighbouring Nb atom can jump to a Sn vacancy to form a Nb-on-Sn antisite defect with a Nb vacancy, because a Nb-on-Sn antisite defect is more stable than Sn vacancy [107]. Perhaps this type of self-organization of Nb_3Sn lattice causes the increase of B_{irr} with reaction time.

Another factor that may influence the Sn content of Nb_3Sn, according to the above model, is the competition between the Sn diffusion rate across the Nb_3Sn layer and the Nb-Sn reaction rate at the Nb_3Sn/Nb interface. So far the influence of the competition between diffusion rate and reaction rate on the Sn content of Nb_3Sn has hardly been noticed, perhaps mainly because similar chemistry (mainly Cu, Sn, Nb, Ta elements) among present Nb_3Sn strands makes it hard to observe any difference in diffusion rate or reaction rate. However, some studies indicated that certain additions can change Nb_3Sn layer growth rate; for instance, Ti can accelerate it [65]. It has been shown that Ti addition segregates at Nb_3Sn grain boundaries, and causes greater lattice distortion at grain boundaries, which is believed to cause higher grain boundary diffusivity [21]. This, according to the theory presented in this section, explains why Ti addition tends to make the Sn content distribution more uniform in the Nb_3Sn layer [88]. On the other hand, as mentioned in section 5.1, Zn addition to Cu-Sn source tends to enhance Nb_3Sn layer growth rate and the Sn content of the Nb_3Sn layer as well [89]. This is because the Zn addition to Cu-Sn increases the activity of Sn in the Cu-Sn source [112], which can thus be explained by the above model.

In summary, the factors determining the Sn content of Nb_3Sn in a Sn source/Nb_3Sn/Nb diffusion reaction couple include the follows. The μ_{Sn} of Sn source and the Sn transfer rate at Sn source/Nb_3Sn interface together set up a limit for the Sn content of the frontier Nb_3Sn layer, while how far under this limit depends on the competition between the diffusion rate and reaction rate. If the reaction rate is very large relative to the diffusion rate, the Nb_3Sn/Nb interface moves before the Sn vacancies have time to

diffuse to Sn source, a lot of Sn vacancies will be left in the Nb_3Sn lattice, causing low Sn content. On the other hand, if reaction rate is very slow so that the Sn source, the Nb_3Sn grain boundaries, and the frontier Nb_3Sn layer have plenty of time to be homogenized, the μ_{Sn} of Nb_3Sn at the reaction frontier can be equal to that of the Sn source; in this case, μ_{Sn} of Sn source is the only limiting factor for the Sn content of Nb_3Sn. From the expression of J_{Sn} in equation 5.3, we see the diffusion rate can be improved by: a) increasing the diffusivity of Sn along the Nb_3Sn grain boundaries and along Nb_3Sn/Nb interface, b) increasing $\Delta\mu$ by increasing the μ_{Sn} of Sn source, c) decreasing the diffusion distance l by reducing the subelement size, and d) reducing grain size, because smaller grain size leads to more grain boundaries which can transport larger amounts of Sn to the reaction frontier.

Chapter 5: Reduction of grain size in Nb_3Sn strands via internal oxidation

5.1 The significance of refining grain size for Nb_3Sn conductors

The optimum pinning occurs in a type-II superconductor when the size of defects is comparable to the fluxon core size (which is the coherence length ξ), while their separation matches the flux line spacing [43]. The coherence length and the 12 T flux lattice spacing at 4.2 K in Nb_3Sn superconductor are about 5 nm and 15 nm, respectively. Apparently, the grain size of present state-of-the-art Nb_3Sn strands, 100-150 nm, is far above the optimum value.

As mentioned in section 1.3, the F_p-B curves of present Nb_3Sn strands shift upward (i.e., their maximum pinning force $F_{p,max}$s increase) as their grain sizes are reduced, but the F_p-B curves always peak at around $0.2B_{irr}$, following Kramer's flux shear model (the expressions shown in equations 1.1-1.3). However, an experiment on Nb_3Sn thin films fabricated by electron-beam co-evaporation deposition nearly 20 years ago [41,42] showed that if their grain sizes were reduced down to 15-30 nm, the peaks of their F_p-B curves would shift to $0.5B_{irr}$, as shown in Figure 39. That the F_p-B curves peak at $0.5B_{irr}$ has been realized in Nb-Ti superconductors, in which non-superconducting α-Ti precipitates serve as the primary flux line pinning centers. The spacing of these α-Ti

ribbons is below 10 nm [113], which is comparable to the flux line spacing, causing the F_p-B curves to peak at $0.5B_{irr}$.

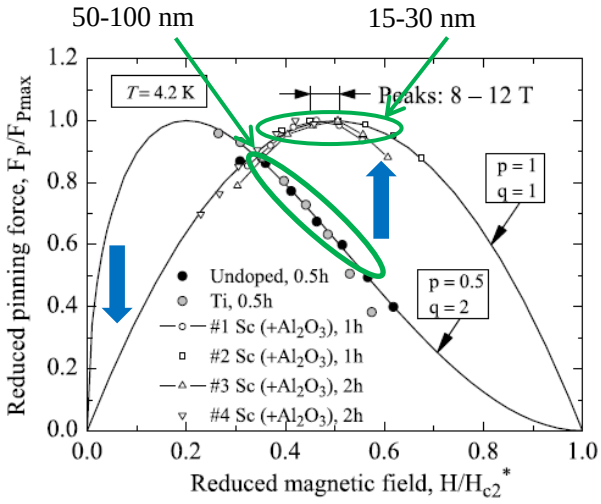

Figure 39. The normalized F_p-B curves for Nb_3Sn films with grain sizes of 50-100 nm and 15-30 nm [42].

The shift of the F_p-B curve peak from $0.2B_{irr}$ to $0.5B_{irr}$ brings two advantages. First, the high-field J_c is significantly improved provided that both strands have the same B_{irr}. Apparently, improvement of J_c at higher field is even greater. The second advantage is the reduction of low-field J_c. For present Nb_3Sn strands, J_cs increase sharply as field decreases, especially below 3 T; however, if F_p-B curve peaks at $0.5B_{irr}$, the variation of F_p with B can be expressed as

$$F_p = 4F_{p,\max} b(1-b) \tag{5.1}$$

or equivalently,

$$J_c = 4\frac{F_{p,\max}}{B_{irr}^2}(B_{irr} - B) \tag{5.2}$$

In this case the J_c-B curve is linear, leading to much smaller low-field J_c and associated magnetization. Because magnetization is the driving force for low-field flux jumps and also field errors in magnets, decreasing the low-field J_c by shifting the F_p-B curve peak to $0.5B_{irr}$ can be a very efficient approach for improving low-field stability and suppressing the persistent-current magnetization contribution to field errors in magnets.

5.2 Previous efforts to refine Nb_3Sn grain size by adding second phase particles

It has been shown above that reduction of grain size to the 15-30 nm level can significantly benefit both the high-field and low-field performances of Nb_3Sn strands. The question is, how to refine the Nb_3Sn grain size down to this level in practical strands? As mentioned earlier, the primary method used at present to reduce Nb_3Sn grain size is to decrease the heat treatment temperature of Nb-Sn precursors for the formation of Nb_3Sn. However, even at a temperature as low as 615 °C, the grain size is still 80-100 nm [39], far from the goal of 15-30 nm.

Another method that has been proven capable of effectively refining Nb_3Sn grain size is adding second phase particles to pin grain boundaries from migrating, and thus prevent grain coarsening. One of such efforts was to add rare earth elements Y or Gd to

Nb melt to make Nb-Y or Nb-Gd alloy [28,71]. Because Y and Gd have little solubility in Nb, they form fine precipitates in Nb. Motowidlo's experiments showed that at 750 °C, addition of 0.75 at.% Y led to a refinement of average grain size from 400-500 nm to 200-300 nm [71]. At 850 °C both Y and Gd worked more effectively to refine grain size. Magnetization measurements at 9 K showed that the $F_{p,max}$ of Y added sample was nearly twice that of the control sample when reacted at 750 °C. Perhaps a larger amount of Y addition can lead to an even more significant reduction of grain size.

Nevertheless, a problem with this method is, even this small amount of addition has hardened the Nb alloy enough to make processing difficult. As mentioned in section 1.3, the manufacturing process for a Nb_3Sn strand is consisted of the following procedures: it starts with a large-size composite of Sn, Cu and Nb metals or alloys (e.g., Nb-7.5 wt.%Ta), which, after many courses of deformation such as extrusion and drawing, forms the final-size strand, which is winded to a cable or coil. Then the heat treatment is applied to transform the precursors to superconducting Nb_3Sn phase. Since the reduction ratio of the deformation process is very large (the ratio of the starting cross-sectional area to the final cross-sectional area of the wires is typically above 100,000), the precursors must be very ductile. This precludes the possibility of adding particles to precursors prior to the deformation process, because the precipitation hardening may make the mechanical deformations of the precursors difficult. Then it leaves only one option, that is, the particles can only be formed through chemical reactions during heat treatment. With all the possibilities taken into consideration, a feasible approach to realize this is the internal oxidation method.

Internal oxidation means that oxygen diffuses into an A-B solid solution, and only selectively oxidizes the solute B. The oxide product of the solute may precipitate out in the matrix (solvent) in the form of fine particles, which may be used for dispersion strengthening or grain refinement. A schematic of the internal oxidation process for an A-B alloy is shown in Figure 40. In the region I (internal oxidation zone), solute B has been oxidized to form BO_n particles, while oxygen continues diffusing across this zone to region II, where internal oxidation is yet to occur. Since the B content in zone I is depleted, B tends to diffuse from zone II to zone I. To make the internal oxidation possible, there are several requirements [114]: the solute B must be much less noble than the solvent A, and the oxygen partial pressure must be high enough to oxidize B but not high enough to oxidize the matrix A, and oxygen must diffuse faster in matrix A than does the solute B; otherwise, a surface oxidation instead of internal oxidation will occur.

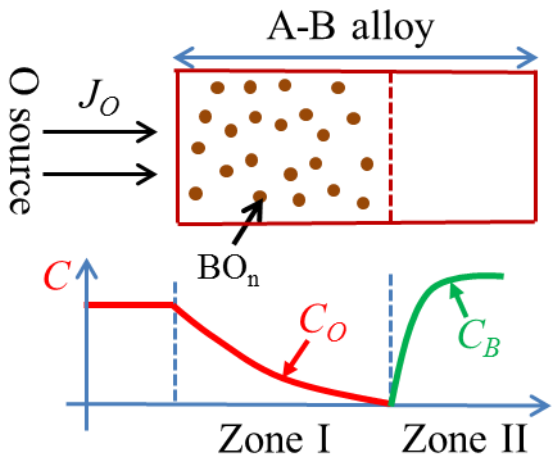

Figure 40. A schematic showing the propagation of the internal oxidation zone.

The internal oxidation method was successfully used in Nb_3Sn tapes in the 1960s [115,116]. To apply this method in the fabrication of a Nb_3Sn tape, commercially available Nb-1wt.%Zr alloy (in place of the usual Nb metal) was used because Zr has much stronger affinity to oxygen than Nb does [117]. Internal oxidation of Nb-1Zr forms fine ZrO_2 precipitates, which impede grain coarsening. The fabrication procedures of internally oxidized Nb_3Sn tapes include the following [116]. First, a Nb-1 wt.% Zr foil is anodized to form a layer of Nb_2O_5 on the surface, then it is annealed at 1000 °C so that Nb_2O_5 decomposes and releases oxygen, which diffuses into Nb-1Zr to form Nb-1Zr-2O alloy. Then the foil is coated with Sn on the surface and reacted at 1050 °C to form Nb_3Sn, with ZrO_2 particles distributed in the Nb_3Sn layer. It was reported that the amount of oxygen addition to Nb-1Zr foil had significant influence on both the Nb_3Sn layer growth rate and Nb_3Sn grain size. With no oxygen added to the Nb-1Zr foil, the reaction rate was relatively slow (with 10 μm of Nb_3Sn formed after 3000s at 1050 °C), and the grain size was very large (2~3 μm). For the foil with such an oxygen amount that O:Zr=1, the reaction rate and grain size were both intermediate (Nb_3Sn layer of 8μm was produced after 500s at 1050 °C and grain size was 500 nm). For the case with O:Zr=2, after reaction at 1050 °C for 200s, the layer thickness was nearly 15 μm and the average grain size was around 300 nm. This demonstrates that internal oxidation of Nb-1Zr can be a powerful method to refine Nb_3Sn grain size. Moreover, the internally oxidized sample also had much higher Nb_3Sn layer growth rate than the control sample at a reaction temperature of 1050 °C. In work [115] the authors reported that for the Nb-1Zr sample the critical current at 10 T was increased monotonically as the oxygen amount

was increased from 0 to 0.3 wt.% (which is equivalent to ~2 at.%). Further increase of oxygen amount beyond 0.3 wt.% would not lead to further I_c improvement, but would cause embrittlement. On the other hand, in pure Nb sample (with no Zr solute) the improvement in I_c with oxygen addition is negligible. Furthermore, they also reported that when nitrogen instead of oxygen was used, there was also a significant improvement in I_c relative to the nitrogen-free sample [115].

As mentioned in section 1.3, the Nb_3Sn conductors with the form of tapes have been replaced by those of wires, for the ease of cabling. Thus, a lot of efforts have been made to transfer the internal oxidation method to Nb_3Sn wires. However, this turns out to be a quite challenging task. A Nb_3Sn wire is different from a tape not only for its round cross section, but more importantly for its peripheral Cu matrix in which all subelements are embedded in. In a Nb_3Sn strand, due to the presence of the outside Cu matrix, oxygen cannot be delivered to the Nb-Zr alloy externally (e.g., by annodization or by annealing in an oxygen atmosphere). It will be shown later that a thick Cu sheath prevents a considerable amount of oxygen from diffusing through.

M. Benz (U.S. Pat. No. 20030085053A1 [118]) tried to pre-dissolve oxygen in Nb-1Zr alloy and to use this oxygen-containing Nb-1Zr for strand fabrication. Similar work was also repeated by B. Zeitlin later in a more systematic way [119,120]. However, both experiments ran into problems when trying to draw the oxygen-containing Nb-1Zr alloy down to a small size, because pre-dissolving oxygen in Nb-1Zr alloy markedly increased its strength and decreased its ductility. It has been mentioned earlier that a lot of

deformations must be performed on a green-state strand to obtain a small subelement diameter (typically 30 - 50 μm) for the sake of electromagnetic stability.

Then Zeitlin turned to use oxide powder as oxygen source [119], expecting the oxygen to be transferred from oxide powder to Nb-1Zr during heat treatment. With this scheme he fabricated a mono-element-internal-tin (MEIT) wire with Nb-1Zr filaments and a core composed of a mixture of SnO_2 and Sn powders (with the amount of SnO_2 enough to oxidize all the Zr in the Nb-1Zr rods), as shown in Figure 41 [119]. A control wire with the core of Sn + Cu powders instead of Sn + SnO_2 powders was also fabricated. Both wires were reacted at 785 and 815 °C. It turned out that the grain sizes of the wire with SnO_2 powder were not refined relative to the control wire. This indicates that the Nb-1Zr filaments were not successfully internally oxidized.

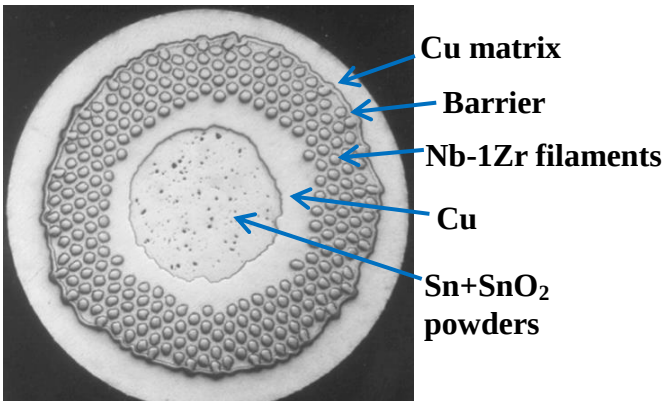

Figure 41. BSE/SEM image of the MEIT strand fabricated by Zeitlin for internal oxidation [119]. The diameter of the final-size wire is 0.254 mm.

Zeitlin speculated that a possible reason for the failure of internally oxidizing the MEIT wire is that this internal oxidation method may only work at high temperatures

(e.g., 1050 °C), but the kinetics and mechanism may not work at low temperatures. It was reported that for the internal oxidation of Nb-1Zr, below 900 °C ZrO_2 particles did not form; instead, oxygen atoms dissolved in Nb-1Zr and were bound to Zr atoms [121], while at higher temperatures ZrO_2 did precipitate out in Nb matrix [122]. Since the tapes were reacted at 1050 °C while the wires were reacted at around 800 °C, it seems to explain why this method worked in the former but failed in the latter.

5.3 The effects of internal oxidation on Nb_3Sn strands

To find out whether it is really impossible to apply the internal oxidation method to Nb_3Sn wires at low reaction temperatures, an experimental tube type monofilament with Nb-1Zr alloy was fabricated. BSE image of the cross section of this strand is shown in Figure 42. With this strand, the outside Cu matrix was etched off so that the Nb-1Zr alloy was exposed to the atmosphere during heat treatments. By heat treating the samples in pure Ar atmosphere, there was no oxygen supply. By using Ar-O mixture instead of pure Ar, sufficient oxygen could be supplied to oxidize the Zr in the Nb-1Zr alloy.

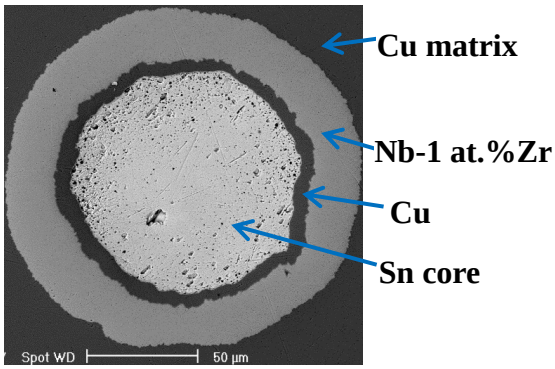

Figure 42. BSE/SEM image of the monofilament with Nb-1Zr alloy.

For comparison the samples were given the same heat treatments in pure argon and in argon-oxygen atmospheres at various temperatures from 650 to 850 °C. The magnified SE/SEM images of the fractured surfaces of the samples reacted at 750 °C in pure Ar and in Ar-O mixture are shown in Figure 43. Clearly the internally oxidized sample has much smaller grain size.

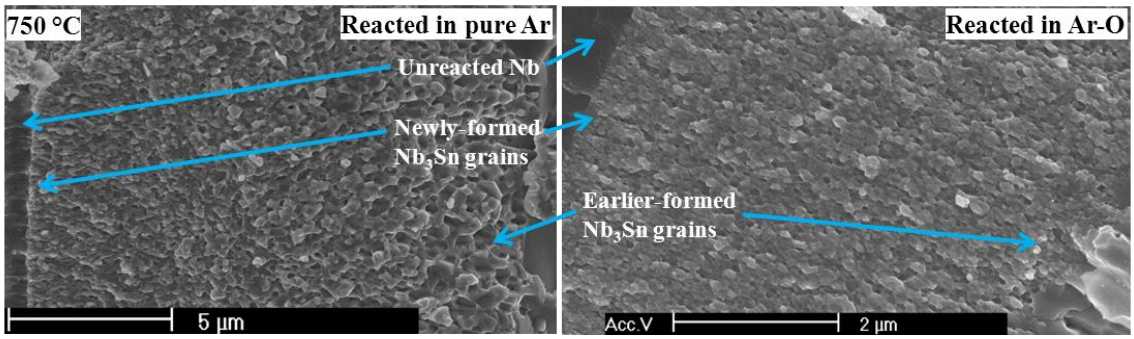

Figure 43. The magnified SE images of the Nb-1Zr monofilament reacted at 750 °C for 10 hours in pure argon and argon-oxygen atmospheres.

TEM image shown in Figure 44 displays the ZrO_2 particles in an internally oxidized sample reacted at 700 °C. There are both intra-granular and inter-granular particles, with

the size ranging from 5 to 20 nm, perhaps even smaller in samples reacted at lower temperatures (625 - 650 °C). The grain size variation with heat treatment temperature for the samples reacted in pure Ar and with sufficient oxygen supply is shown in Figure 45. It is clear that internal oxidation refines the grain size in the whole temperature range, from 650 °C to 850 °C.

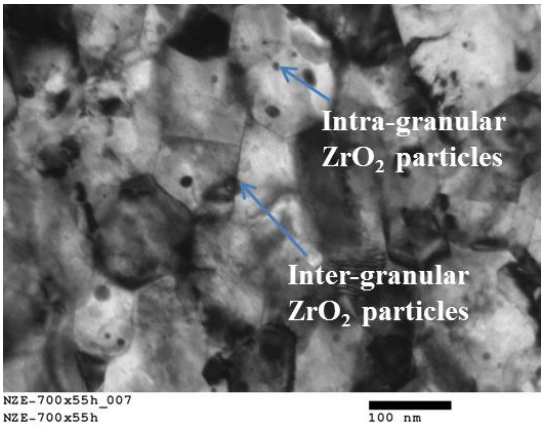

Figure 44. TEM image of the Nb-1Zr monofilament reacted at 700 °C for 55 hours in an argon-oxygen atmosphere. Examples of intra-granular and inter-granular ZrO_2 particles are marked.

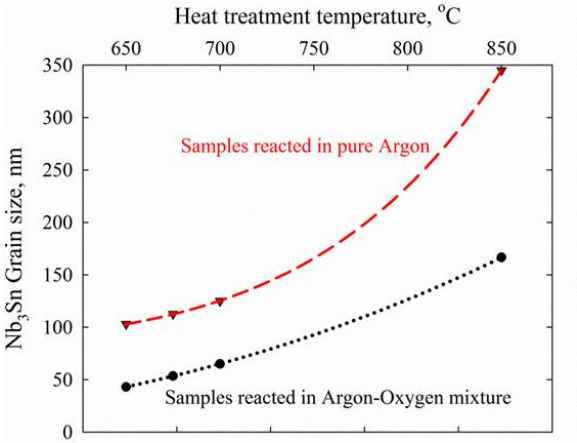

Figure 45. Average Nb_3Sn grain size as a function of reaction temperature for the Nb-1Zr monofilament reacted in pure argon and in argon-oxygen atmospheres. The dashed lines are exponential fits to the data.

Hence, the above experiment demonstrates that this internal oxidation method does work for Nb_3Sn at low reaction temperatures. Then what is the mechanism for grain size refinement due to internal oxidation? First, from Figure 43, it is clear that in the control sample with no internal oxidation, there is an apparent gradient in grain size across the Nb_3Sn layer, with earlier-formed grains clearly having larger grain size, which indicates that grains coarsen with heat treatment time. On the other hand, for the internal oxidation sample, except a gradient for the newly-formed grains (in a region of several hundred nano-meters), the grain size is fairly uniform across almost the entire layer. This indicates that the ZrO_2 particles must impede grain boundaries from migrating and thus inhibit grain coarsening with annealing time. Second, a closer observation of the newly-formed Nb_3Sn grains reveals that those in the internal oxidation sample are much smaller. This indicates that the ZrO_2 particles must serve as nucleation centers for Nb_3Sn grains as well, which would increase the number of grains and decrease their average size.

Here it is interesting to ask this question, if ZrO_2 particles cannot form in Nb-1Zr at low reaction temperatures (e.g., below 900 °C [121]), how could they precipitate out in Nb_3Sn after Nb-1Zr transforms to Nb_3Sn in the above monofilament? Before getting down to this question, let us first think about this pre-question: why Zr and O simply dissolve in Nb lattice at low temperatures, but precipitate out as ZrO_2 particles in Nb at high temperatures? A possible explanation is following. As oxygen diffuses in Nb-Zr, Zr atoms trap oxygen atoms because Zr has stronger affinity to oxygen than Nb does; this forms Zr-2O clusters in Nb matrix. Previous studies suggested that in a Zr-2O cluster, a pair of oxygen atoms are seated on opposite nearest neighbor octahedral sites of a Zr atom [123]. In order for ZrO_2 particles to precipitate out, they have to first nucleate. The overall Gibbs free energy change for homogeneous nucleation of ZrO_2 particles (which are assumed to be spheroidal) is:

$$\Delta G = 4/3\pi r^3(\Delta G_v + \Delta G_s) + 4\pi r^2\sigma \qquad (5.3)$$

where ΔG_v is the decrease of free energy per unit volume due to precipitation of the Zr-2O atoms in Nb (i.e., the free energy change associated with the chemical reaction Zr + 2O = ZrO_2), ΔG_s is the unit-volume strain energy change because precipitation of ZrO_2 particles removes Zr and O solutes from Nb matrix but adds ZrO_2 precipitates into it, and σ is unit-area surface energy of the interfaces between ZrO_2 particles and its surrounding matrix. In equation 4.3, ΔG_v is negative, σ is positive, while ΔG_s can be positive or negative, depending on whether the strain relief due to the removal of Zr and O solutes from matrix lattice can compensate the strain caused by insertion of ZrO_2 particles in the matrix. Apparently, as the nucleus radius r is small, the $4\pi r^2\sigma$ term dominates so that ΔG

is positive and the nucleation process is not favored. Only as the radius r is larger than a minimum radius r_c can the Gibbs free energy change becomes negative. To attain r_c, many of the Zr-O clusters must come together by diffusion in Nb. At low temperatures, the diffusivity of Zr in Nb is low (e.g., around 1.3×10^{-24} m^2/s at 1000 K [124]), making it hard to reach r_c, explaining why no ZrO_2 precipitates form at low temperatures. At high temperatures, however, the diffusivity of Zr in Nb is high (e.g., $\sim 5 \times 10^{-20}$ m^2/s at 1300 K [124]), allowing for precipitation.

Then why at low temperatures the Zr-2O clusters dissolving in Nb can precipitate out after Nb transforms to Nb_3Sn (or equivalently, after Nb_3Sn/Nb interface sweeps across)? There are a couple of possibilities. First, the ΔG_s and σ terms for the matrix of Nb_3Sn are different from those for Nb, which may make the critical radius in the Nb_3Sn matrix smaller and thus the precipitation easier. Second, Zr and O atoms in the Nb matrix can perhaps diffuse along the Nb_3Sn/Nb inter-phase interface as the interface comes across them. The fast diffusivity along the interface allows them to reach the critical radius and thus precipitate out. Another possibility is, Zr and O can diffuse faster in Nb_3Sn (either in bulk or along grain boundaries), allowing them to reach the critical radius in a shorter time and precipitate out. As mentioned earlier, ZrO_2 particles can serve as nucleation centers for Nb_3Sn grains, so some of the ZrO_2 particles must form at the Nb_3Sn/Nb interface, in a way described in the second possibility above.

5.4 Application of the internal oxidation method to practical Nb_3Sn strands

The results of the above monofilament with oxygen supplied externally demonstrate that internal oxidation can occur in Nb_3Sn at low reaction temperatures. Then the next question is, how to apply this method to practical Nb_3Sn strands? Since subelements (or filaments) are the basic superconducting units of these strands, let us only discuss the design of subelements (or filaments).

Generally speaking, two modifications need to be made on a subelement to enable internal oxidation. First, it must be fabricated with a Nb alloy (here denoted as Nb-M) that can be internally oxidized. Second, it must contain an oxygen source that can supply oxygen to the Nb-M alloy during heat treatment, because pre-dissolving oxygen in the Nb alloy is not feasible due to decrease in workability. The selection of the metal M is critical. First, M must have high solubility in Nb so that it can form a Nb-M solid solution with a decent content of M. Second, to guarantee that during heat treatment the metal M is selectively oxidized while Nb itself is left non-oxidized for the subsequent formation of Nb_3Sn, the element M must be much less noble than Nb. Furthermore, from equation 4.3, it is clear that the critical radius r_c is closely related to the affinity of M to oxygen: the more stable the M-O oxide particles (as the internal oxidation product) are, the more negative ΔG_v is, the smaller r_c is, and the more effectively the particles can refine the Nb_3Sn grain size. Among all the metals, Ti, Zr and Al are practical candidates satisfying both requirements. However, if Nb-Ti alloy is used, whether the TiO_2 precipitates in Nb_3Sn matrix are sufficiently fine and well-dispersed to effectively refine Nb_3Sn grains

still needs further verification. Internal oxidation of Nb-Zr or Nb-Al alloy, which forms respectively fine ZrO_2 or Al_2O_3 precipitates, is a more feasible choice.

On the other side, in this work oxide powders will be used as oxygen source because of the good flowability of powders during the drawing process. Thus, it is necessary to find out what are the issues with Zeitlin's MEIT wire that prevented itself from being internally oxidized. Two problems can be found. First, from the Ellingham diagram (which shows the formation energies of metal oxides) of the relevant metals as shown in Figure 46, it can be seen that Sn is less noble than Cu, so Cu cannot take up oxygen from SnO_2. However, in this MEIT wire (Figure 41), the SnO_2 powder is completely surrounded by Cu. Therefore, this inert Cu layer blocks the path of oxygen transfer, which must be the reason why this scheme failed.

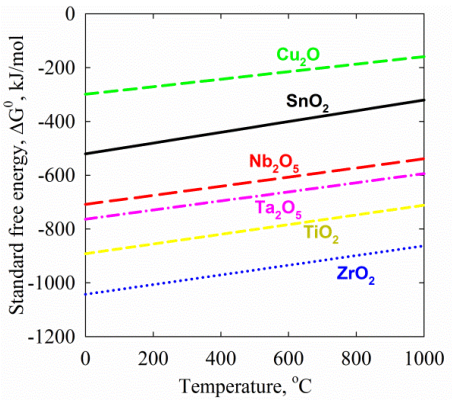

Figure 46. The Ellingham diagram of some metals showing the formation energies of metal oxides.

The second problem is that, even if Cu can absorb oxygen from the core (provided that another oxide powder such as CuO is used), a calculation shows that the oxygen

diffusion rate in Cu is too slow to supply sufficient amount of oxygen to oxidize the Zr in Nb-1Zr alloy of the MEIT strand. Suppose we have a Nb1Zr-sheathed Cu tube with the core filled by CuO powder to supply oxygen, which diffuses through the Cu tube and is absorbed by the outer Nb-1Zr alloy. Suppose the oxygen concentration in Cu at the CuO side is the solubility of oxygen in Cu, while that at the Nb-1Zr side is zero because all the oxygen is absorbed by Nb-1Zr. A calculation using the Fick's first law shows that the diffusion rate of oxygen through Cu per unit length can be expressed as:

$$\frac{dn}{dt} = \frac{2\pi D X_s}{\ln(r_o / r_i) V_m} \tag{5.3}$$

where D and X_s are respectively the diffusivity and solubility of oxygen in Cu, r_o and r_i are respectively the outer and inner radii of the Cu tube, and V_m is the molar volume of oxygen-containing Cu. Although the diffusivity of oxygen in Cu is high (about 10^{-12} m^2/s at 600 °C [125]), the solubility is very low (about 10^{-5} at.% at 600 °C [100]), making the amount of oxygen diffusing across the Cu layer in a certain period small, unless the Cu layer is very thin compared with its inner radius (i.e., r_o/r_i in equation 5.3 is very close to 1).

On the other hand, it can be seen from the Ellingham diagram (Figure 46) that Nb can indeed reduce SnO_2. Thus, if the Cu layer between Nb and SnO_2 powder is removed so that Nb and SnO_2 contact, Nb should take up the oxygen from SnO_2 powder during heat treatments. To verify whether this is a feasible plan for supplying oxygen, a simple wire composed of a Cu-sheathed Nb tube that is filled by SnO_2 powder was fabricated, and was reacted at various temperatures. The content of oxygen absorbed by the Nb was calculated from its critical temperature T_c which was obtained from its magnetization vs.

temperature (*M-T*) curve, because previous studies showed that T_c of Nb drops by 0.93 K for each at.% oxygen dissolved in [126]. It turned out that this structure can indeed supply sufficient oxygen. The normalized magnetic moment vs. temperature (*m-T*) curves for the samples after various heat treatments are shown in Figure 47 (a). It can be seen that the oxygen content increases with reaction temperature – which could be because of either increased absorption rate or increased oxygen solubility in Nb with temperature, reaching >2 at.% for the sample reacted at 500 °C. It is also interesting to note that for the samples reacted at and above 550 °C, NbO_2 and NbO compounds formed after a certain reaction time, an example shown in Figure 47 (b).

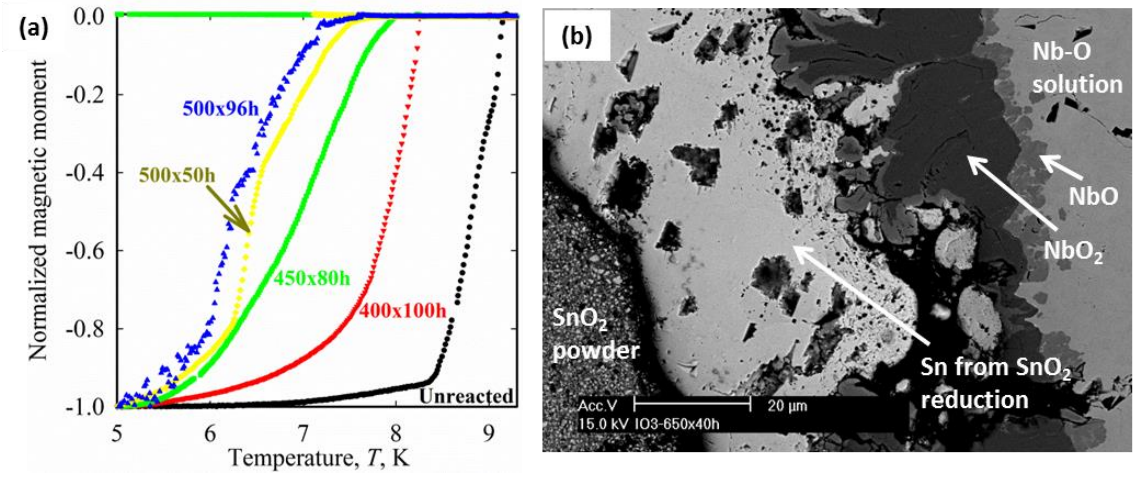

Figure 47. (a) Normalized *m-T* curves of the SnO_2/Nb/Cu wire reacted at various temperatures, and (b) SEM image of the sample reacted at 650 °C for 40 h, showing the Nb-O compounds [127].

It is found that these Nb-O compounds tend to form at high reaction temperatures, and once they form at the Nb alloy surface, they may prevent Sn from diffusing into Nb

for Nb_3Sn formation. So why do these Nb-O compounds form, particularly at high temperatures? A possible explanation is as follows. With oxygen supply from the oxide powder to Nb alloy surface, the oxygen also diffuses deeper into the Nb alloy, as shown in the schematic of Figure 40. However, if the oxygen supplying rate is larger than the diffusion rate in Nb alloy, the oxygen concentration at the SnO_2/Nb alloy interface will increase with time. As the oxygen concentration is above the oxygen solubility in Nb, Nb-O compounds would form. That the formation of Nb-O compounds is favored at high temperatures indicates that the increase of the oxygen supplying rate by oxide powder with temperature is faster than the increase of the oxygen diffusion rate in Nb. So how to avoid this problem? One way is to use a two-stage heat treatment: the low-temperature (e.g., 500 °C) stage is used to transfer oxygen from the oxide powder to Nb-Zr alloy, and the high-temperature (e.g., 650 °C) stage is used for Nb_3Sn formation. The other way is to use a more stable oxide (e.g., Nb_2O_5) as oxygen source instead of SnO_2, because oxides of a less noble metal should release oxygen slower. Meanwhile, it is worth mentioning that if other structures are used, this excess SnO_2 may not be a problem, which will be seen later.

The feasibility of using other oxide powders that can be reduced by Nb was also explored, which finally proved that CuO, SnO_2, ZnO, or Nb_2O_5 can all supply considerable amount of oxygen to Nb-1Zr alloy, while NbO_2 and NbO cannot, because they are more stable than Nb-O solution [128]. It was also found that SnO_2 can supply all of its oxygen until itself finally turns into liquid Sn; on the other hand, Nb_2O_5 can only transform to NbO_2.

Another experiment was conducted to find out whether direct contact between oxide powder and Nb alloy is necessary for oxygen transfer. Oxide powders including CuO, SnO_2, ZnO, and Nb_2O_5 were put respectively at the bottoms of quartz tubes, and the quartz tubes were necked at a certain height above the powders so that: (i) Nb pieces were constrained above the necks without getting direct contact with the oxide powders, and (ii) the atmospheres between the Nb pieces and the oxide powders still connected through the necks. A picture of a tube with Nb_2O_5 powder is shown in Figure 48 (a). The quartz tubes were pumped to high vacuum ($<1 \times 10^{-3}$ Pa) and then backed up with 200 torr of argon. Then the tubes were transferred to a furnace for heat treatments at 600-800 °C. It was found that oxygen could still be transferred from the oxide powders to the Nb strips, and with excess Nb, SnO_2 powder finally transformed to liquid Sn, while Nb_2O_5 transformed to NbO_2. The normalized *m*-*T* curve of a Nb piece with Nb_2O_5 powder after a heat treatment of 700 °C/40 hr is shown in Figure 48 (b). This experiment demonstrates that as long as the atmosphere connects, oxide powders can supply oxygen to Nb alloy through atmosphere.

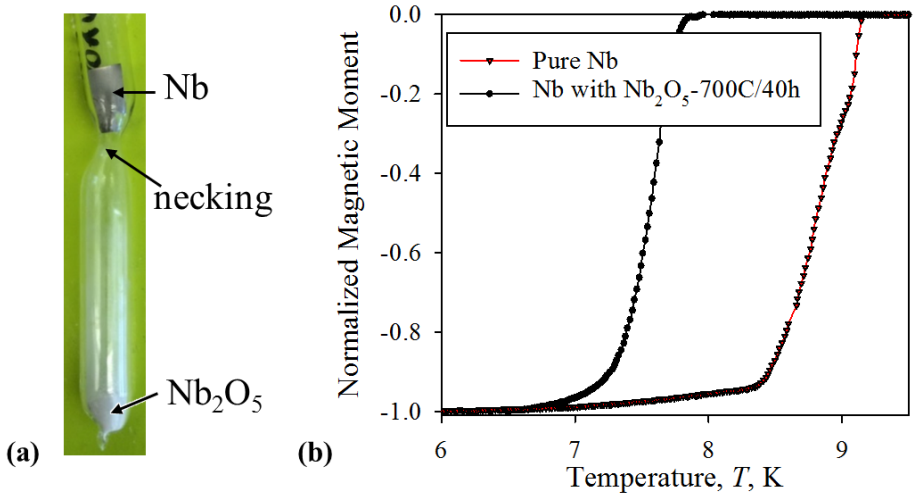

Figure 48. (a) A picture showing the separation of the Nb_2O_5 powder and a Nb piece, and (b) normalized *m-T* curves showing that Nb piece with Nb_2O_5 powder after a heat treatment of 700 °C/40 hr had taken the oxygen.

In the above, the characteristics of oxygen transfer from oxide powder to Nb alloy are discussed. Based on these instructions, the subelement structures of various types of Nb_3Sn strands will be properly modified in the following, so that the oxide powder is located in proper positions inside the subelements to release sufficient amount of oxygen to oxidize the Zr or Al atoms in Nb-Zr or Nb-Al alloy during heat treatments.

A feasible subelement (or filament) structure enabling internal oxidation in a tube type wire is illustrated in Figure 49. The subelement is comprised of five concentric layers, namely, the central Sn rod, the Cu layer, the oxide powder layer, the Nb-Zr or Nb-Al alloy tube, and the Cu matrix. This design has two modifications with respect to a conventional tube type subelement: first, the standard Nb-7.5wt.%Ta alloy is replaced by Nb-Zr or Nb-Al alloy because Nb-Ta alloy cannot be internally oxidized; second, a layer

of oxide powder is added into the subelement. The oxide powder is deliberately positioned between the Cu layer and the Nb alloy tube, so that the Nb alloy can reduce the oxide powder and take up the oxygen during heat treatment. If the oxide powder is located between the Cu layer and the central Sn rod, excess heat treatment time may be needed to supply sufficient amount of oxygen to Nb alloy through the Cu layer. If the oxide powder is located between the Nb alloy tube and the Cu matrix, there will be two problems: first, the reduction product of the oxide powder, which is usually pure metal (such as liquid Sn), may poison Cu matrix; second, after reaction the vacant space left in the original oxide powder layer may block current transfer from Cu matrix to Nb_3Sn.

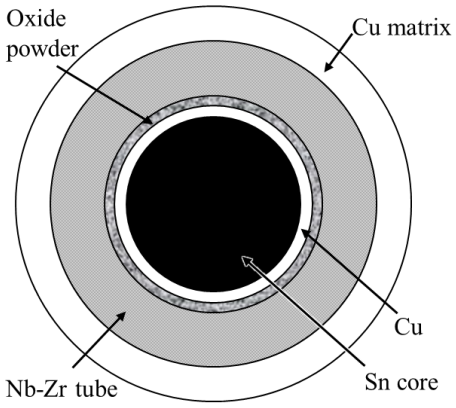

Figure 49. A schematic representation of a modified tube type subelement to realize internal oxidation.

Figure 50 shows a convenient scheme to realize internal oxidation in a powder-in-tube subelement (or filament). The subelement is comprised of a Cu-jacketed Nb-Zr or Nb-Al alloy tube, which is filled with a mixture of Sn source (e.g., Cu-Sn or Nb-Sn intermetallics) and oxide powders.

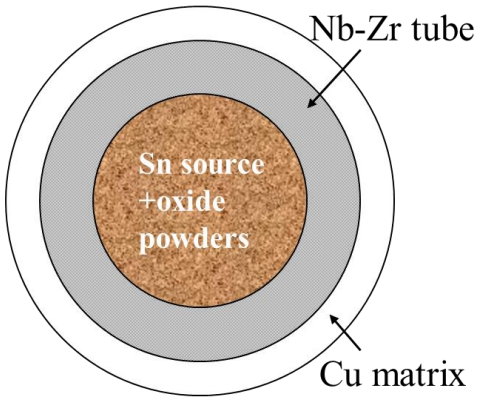

Figure 50. A schematic representation of a modified powder-in-tube subelement to realize internal oxidation.

During heat treatment, the oxide powder in the core releases oxygen for Nb alloy to be internally oxidized. Experiments described earlier demonstrated that oxide powder such as SnO_2 or Nb_2O_5 can supply oxygen to Nb alloy through atmosphere. Hence, even the oxide powder in the core is blended with the Sn-source powder and thus does not contact the Nb alloy tube in Figure 50, it can still supply oxygen to Nb alloy. However, one possible problem with this scheme is the competition between the outward diffusion of Sn and outward diffusion of oxygen: once Nb-Sn intermetallic compounds begin to form at inner surface of the Nb alloy tube, the newly formed $NbSn_2$ or Nb_6Sn_5 layer may block the connection between the oxide powder and the unreacted Nb alloy, and thus terminate the oxygen transfer process. A cure to this problem is to increase the amount of oxide powder in the core to guarantee the full oxidation of the Nb-Zr alloy. Furthermore, as described in section 3.3, Cu-Nb-Sn ternary phase first forms during the temperature

ramping up, followed by the $NbSn_2$ phase as the temperature reaches a certain value. If the Cu-Nb-Sn ternary phase allows for oxygen transfer, then another possible solution to the above problem is to add a pre-heat treatment stage at a temperature (e.g., 450 °C) below the formation temperature of $NbSn_2$ phase. However, whether this method truly works still needs further confirmation.

For tube type and powder-in-tube subelements, the oxide powder can also be put into the axial holes drilled through the Nb alloy tube wall, a schematic shown in Figure 51. Such a structure has two advantages over the above PIT subelement structure shown in Figure 50. First, as mentioned above, in the above PIT subelement where both Sn source and oxygen source are in the core, due to the formation of Nb-Sn layers which block oxygen transfer, excess oxide powder may be needed to fully oxidize the Nb-Zr alloy, which certainly leads to a large core size and reduces Nb_3Sn area fraction after reaction. The structure shown in Figure 51, however, avoids this problem because oxygen source is separated from the Sn core. Second, in the structure shown in Figure 51, Ti addition can be easily realized by using Sn-Ti alloy in the core. In contrast, addition of Ti in the core of the above PIT subelement would lead to reaction between Ti and oxygen, making both Ti doping and oxygen transfer unsuccessful. In such a PIT structure, Ta or Ti doping can perhaps only be realized by using specially-made Nb-Zr-Ta or Nb-Zr-Ti ternary alloy, which increases the cost of the strand.

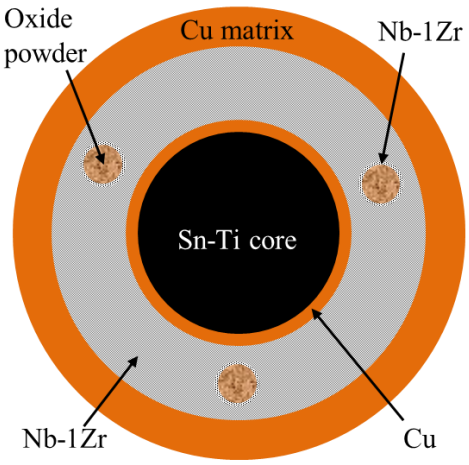

Figure 51. A schematic of a modified tube type subelement with axial holes enabling internal oxidation.

Figure 52 shows a schematic representation of a modified distributed-barrier internal-tin subelement that enables internal oxidation. It comprises of a Sn core, a Cu can, a stacking of Cu-encased Nb-Zr rods, a certain number of which are replaced by oxide powder-filled Cu tubes, a Nb alloy barrier, and Cu matrix. As mentioned earlier, the diffusion rate of oxygen through Cu layer is slow, so in order to supply sufficient amount of oxygen through a Cu layer to Nb-Zr, the Cu layer should be thin (that is, r_o/r_i should be close to 1). Besides, it is always helpful to break one master CuO-powder source into a number of distributed, small ones so that each CuO-powder source only needs to supply a relatively small amount of oxygen to its surrounding Nb-Zr alloy, which certainly reduces the required time for oxygen supply. In a final-size RIT subelement, the thickness of the Cu layer among the Nb alloy rods is no more than hundreds of nano-meters, which allows for rapid transfer of oxygen from the oxide powder to the surrounding Nb alloy rods. It should be noted, however, whether SnO_2 or

Nb_2O_5 powder is able to work for this purpose needs further verification, because these oxides cannot be reduced by Cu and thus may not be able to supply oxygen through Cu. If this is the case, CuO powder is a feasible choice. If, on the other hand, after pre-heat treatments at 210 °C and 400 °C, most of the original Cu channels among Nb alloy filaments become voids due to Cu-Sn interdiffusion, as shown in Figure 22, these voids may allow for connection of atmosphere within the subelement, facilitating transfer of oxygen. In this case, SnO_2 and Nb_2O_5 powders also work.

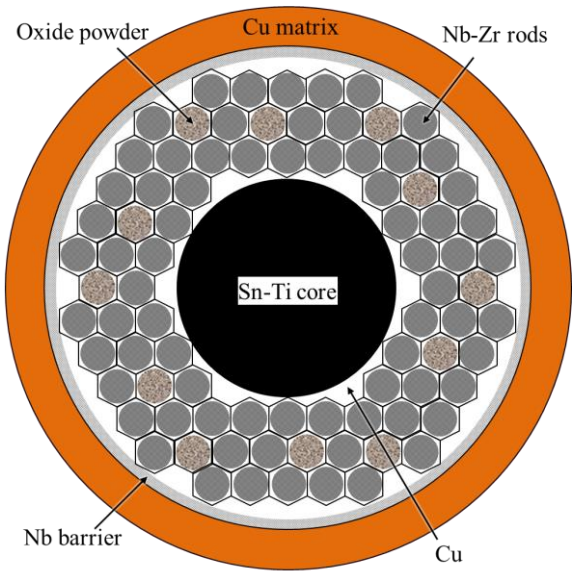

Figure 52. A schematic representation of a modified distributed-barrier internal-tin subelement to realize internal oxidation.

The above structure works for distributed-barrier internal-tin subelements thanks to their low local area ratios of Cu to Nb. However, for single-barrier internal-tin or bronze-process wires, due to their thick Cu or bronze layers among Nb alloy filaments, a

different structure is required for internal oxidation of the filaments: an example for the bronze-process strands is shown in Figure 53. In this scheme each Nb-Zr rod contains an axial gun-drilled hole which is filled with oxide powder for supplying oxygen to this Nb alloy rod.

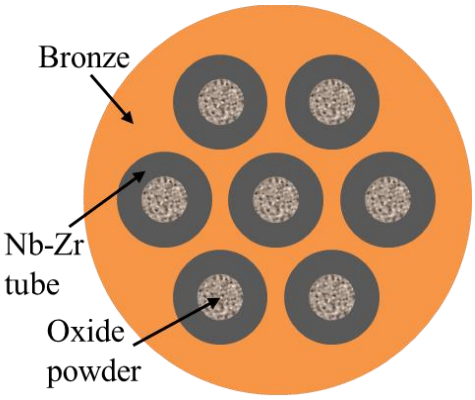

Figure 53. A schematic representation of a modified bronze-process wire to realize internal oxidation.

To verify whether the above schemes are really feasible, a tube type subelement following the structure of Figure 49 was fabricated, with BSE image shown in Figure 54. The outer diameter of the Nb-1Zr tube in the final-size subelement was 0.22 mm. A control wire with NbO_2 powder instead of SnO_2 was also fabricated, because NbO_2 supplies little oxygen to Nb-Zr. Both strands were heat treated at 650 °C for 150 hours.

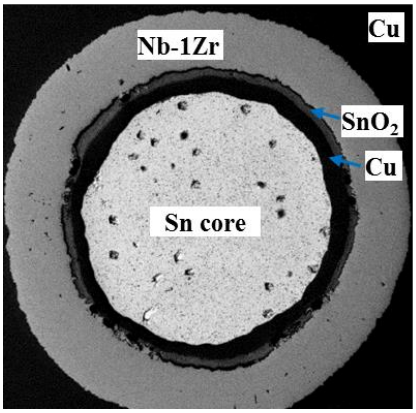

Figure 54. BSE image of the monofilament wire with Nb-1Zr tube and SnO_2 powder.

Figure 55 shows the *m-T* curves for both samples, from which it can be seen that the T_c of the unreacted Nb-1Zr in the strand with NbO_2 powder was 8.9 K, whereas the value for that with SnO_2 was 6.6 K, indicating that the NbO_2 powder supplied little oxygen (<0.5 at.%) to the Nb-1Zr alloy, while in the strand with SnO_2 powder nearly 3 at.% oxygen was absorbed by the Nb-1Zr alloy.

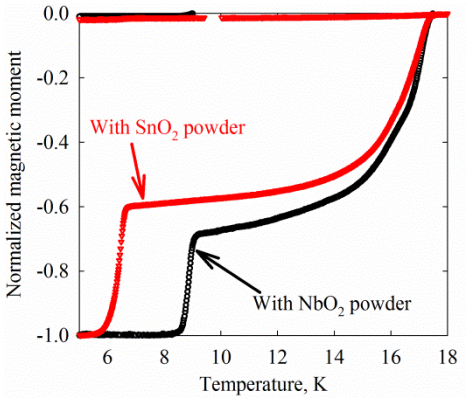

Figure 55. Normalized *m-T* curves for the strands with NbO_2 and SnO_2 powders, both reacted at 650 °C for 150 hours.

As a consequence, the grain sizes of the samples with NbO_2 and SnO_2 reacted at 650 °C for 150 hours were quite different, as can be seen from the SE images of fractured surfaces in Figure 56: the average grain size of the NbO_2 wire was 104 nm, while that of the SnO_2 wire was only 43 nm. Apart from being reacted at 650 °C, both strands were also heat treated at 625 °C for 800 hours. The grain size distribution of the strand with SnO_2 was mainly within 20-50 nm, with an average of 36 nm, while that of the strand with NbO_2 was mainly within 30-160 nm, averaging out at 81 nm, which is slightly smaller than conventional Nb_3Sn strands reacted at 625 °C (100-110 nm) [70], perhaps because the small amount of oxygen released by the NbO_2 contributed to the refinement of grain size. The above data show that internal oxidation in the strand with SnO_2 not only markedly refined the grain size, but also made the span of grain size distribution relatively smaller. Since grain coarsening is a process in which larger grains grow at the expense of their neighboring smaller grains, the grain-boundary-pinning effect of the ZrO_2 particles may explain the more uniform distribution of grain size in such samples.

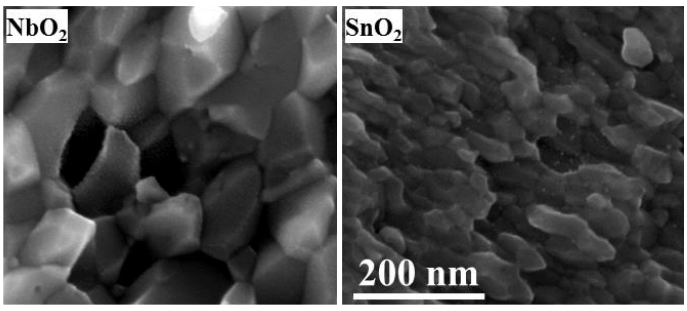

Figure 56. Magnified SE images on fractured surfaces of the subelements with NbO_2 and SnO_2 powders, both reacted at 650 °C for 150 hours.

However, it was also noticed that in the internally oxidized samples grain coarsening might occur after long reaction times. SEM images of the strand with SnO_2 powder reacted at 650 °C for 150 and 400 hours are shown in Figure 57 (a) and (b), respectively. After a 150-hour reaction, all the grains were very fine; however, when the reaction time was prolonged to 400 hours, some grains (denoted "unrefined" in Figure 57) grew to sizes similar to those of conventional Nb_3Sn strands. This perhaps indicates that the refined grains associated with ZrO_2 pinning are in fact in a metastable state. This may be due to the coarsening of the ZrO_2 particles themselves for long reaction times, and a corresponding local coarsening of the grain size. The coarsening of ZrO_2 particles may indicate that Zr and O can diffuse in bulk Nb_3Sn or along Nb_3Sn grain boundaries, which is consistent with the third explanation in section 4.3 for the precipitation of ZrO_2 particles in Nb_3Sn layer. For those regions where ZrO_2 particles disappear, Nb_3Sn grains coarsen again. Fortunately, subelements in practical Nb_3Sn wires are much smaller than the experimental monofilaments and thus do not require such long reaction times.

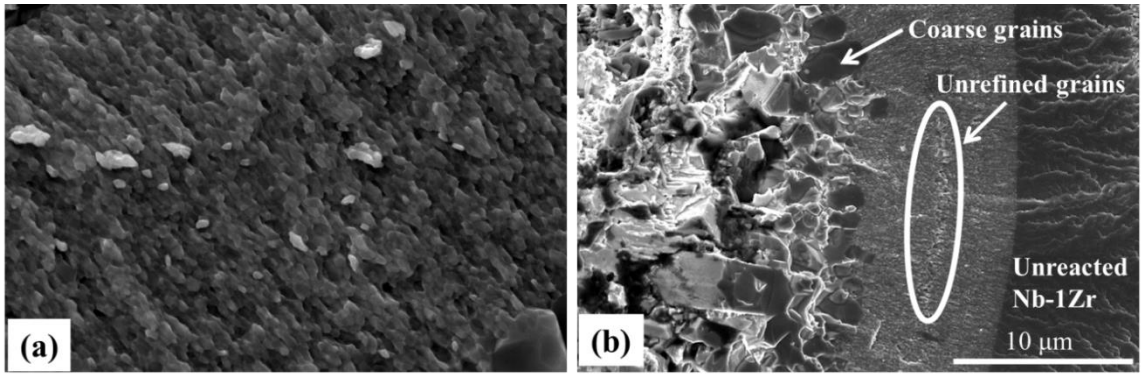

Figure 57. SE images of fractured surfaces of the strand with SnO_2 powder, reacted at 650 °C for (a) 150 and (b) 400 hours.

Next let us see how the J_c of a Nb_3Sn strand is influenced by internal oxidation. An attempt to measure the transport J_c of the above monofilament wire with SnO_2 powder using the four-point method was not quite successful, because the measurements quenched before the critical currents were reached due to the large subelement size. The measured 10 T layer current density at quench for the strand with SnO_2 (650 °C / 400 h) was 10,600 A/mm^2. Then the magnetic J_cs of these samples were measured. Magnetic moment vs field (*m*-*B*) loops were measured for these samples at 4.2 K, and the Nb_3Sn layer J_cs were then calculated based on the expression for a hollow cylinder in a perpendicular field, $J_c=3\Delta m/\{L\cdot(d_o^3-d_i^3)\}$, where Δm is the height of the *m*-*B* loop, L is the sample length, d_o and d_i are the outer and inner diameters of the current-carrying Nb_3Sn layer, respectively. The d_o was measured from the BSE image of the reacted strand; but the inner boundary could not be easily discerned due to the presence of a layer of ill-connected Nb_3Sn coarse grains, which are transformed from Nb_6Sn_5 phase and do not carry transport current. Thus, Nb_3Sn layer thicknesses, *t*s, from the SE images of fracture surfaces (e.g., Figure 57) were measured, and d_is were extracted using $d_i=d_o-2t$. To minimize error, several images were taken from various positions of the cross section, and on each image at least 6 line measurements were performed; t was calculated by averaging these measurements, with the error estimated to be smaller than 5%. The calculated layer J_cs are shown in Figure 58 (a). The 4.2 K, 12 T layer J_cs of the strand with NbO_2 reacted at 625 °C for 800 h is 4400 A/mm^2, close to those of the present-day high-J_c Nb_3Sn strands. On the other hand, the values of the strand with SnO_2 reacted at

650 °C for 400 h and at 625 °C for 800 h are 8500, and 9600 A/mm^2, respectively, with the latter one almost doubling that of the best present-day Nb_3Sn strands.

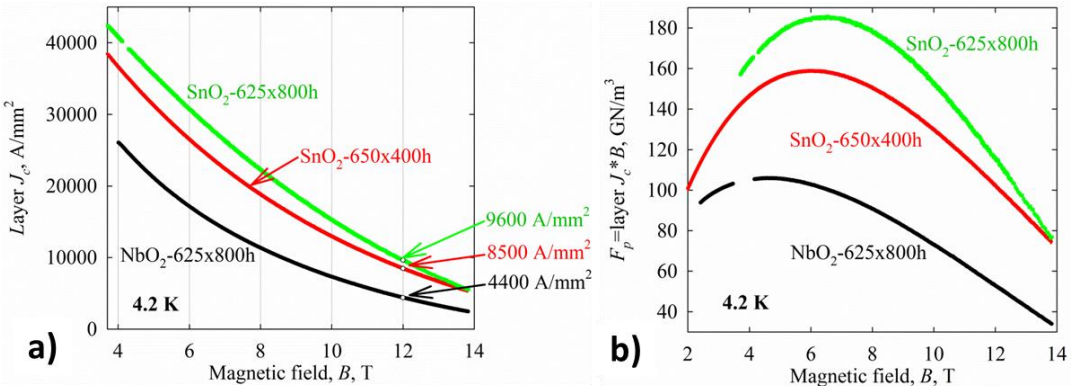

Figure 58. (a) Layer J_c-B curves and (b) F_p-B curves (4.2 K) for the strands with NbO_2 and SnO_2 given the specified reactions.

Then the F_p-B curves are calculated from the J_c-B curves, and shown in Figure 58 (b). Figure 59 (a) shows the $F_{p,max}$ vs. the reciprocal of grain size, 1/d, of the internally oxidized samples, along with data for some conventional PIT and RIT strands. It is interesting to note that $F_{p,max}$ increases linearly with 1/d when grain size is large, but the curve bends over as the grain size goes below ≈100 nm. Subsequently, the F_p-B curves in Figure 58 (b) were fitted to a universal scaling law $F_p=Kb^p(1-b)^q$ (where K is a pre-factor related to the maximum pinning force $F_{p,max}$, and $b=B/B_{irr}$) to obtain the B_{irr} values [129]. The B_{irr} value for the strand with NbO_2 (625 °C/800 h) is 20.9 T, while those of the strand with SnO_2 are 23 T (for 650 °C/400 h) and 20 T (for 625 °C/800 h). And by normalizing F_p to $F_{p,max}$ and B to B_{irr}, normalized F_p-B curves were generated and are shown in Figure 59 (b), from which it can be seen that the strand with NbO_2 peaks at

≈0.2B_{irr}, following the common characteristic of conventional Nb_3Sn strands [32]. For the strand with SnO_2 (650 °C/400h), the average grain size of which is 43 nm, with a peak at 0.26B_{irr}, indicating a slight shift to higher field. The shift for the strand with SnO_2 (625 °C/800 h) is, however, quite clear, to 1/3B_{irr}.

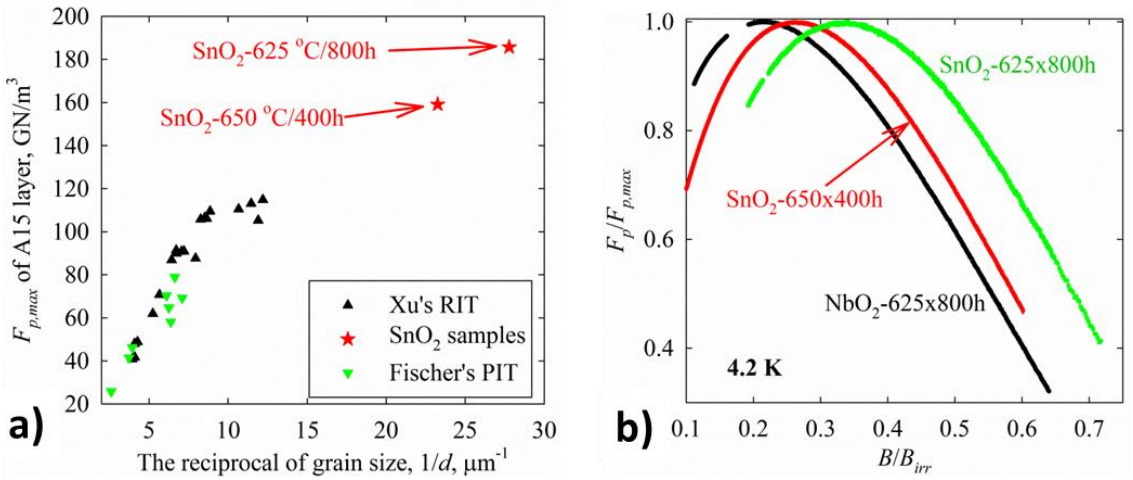

Figure 59. (a) $F_{p,max}$ vs reciprocal grain size for the internally oxidized samples and some conventional Nb_3Sn [39,57], and (b) normalized F_p-B curves (4.2 K) for the strands with NbO_2 and SnO_2 given the specified reactions.

There are some debates about the mechanism for the shift of F_p-B curve peak to one third of B_{irr} for the sample with grain size of 36 nm. Some argue that this is due to point pinning by ZrO_2 particles, and thus follows the point-pinning behavior proposed by Dew-Hughes [129]. If this is the mechanism, then F_p-B curve peak cannot be shifted further to >1/3B_{irr}. The second explanation is, as the refined grain size becomes closer to flux line spacing, it becomes an individual pinning behavior; and if this mechanism is true, then the F_p-B curve can eventually shift to half of B_{irr} by further refining grain size. So, which

mechanism is correct? The easiest way to find out the answer is to further refine grain size, and see if the peak can further shift to higher field. To obtain smaller grain size, a PIT strand fabricated with the scheme of Figure 50 was heat treated at 600 °C, which led to an average grain size of about 30 nm (SE image of a fractured surface is shown in Figure 60 a). And a fit to its F_p-B curve at 4.2 K gave that the curve peaks at $0.4B_{irr}$, as shown by the Figure 60 (b), which indicates that the second mechanism is correct. An extrapolation shows that the F_p-B curve peak can shift to half of B_{irr} by further refining grain size down to roughly 20-25 nm.

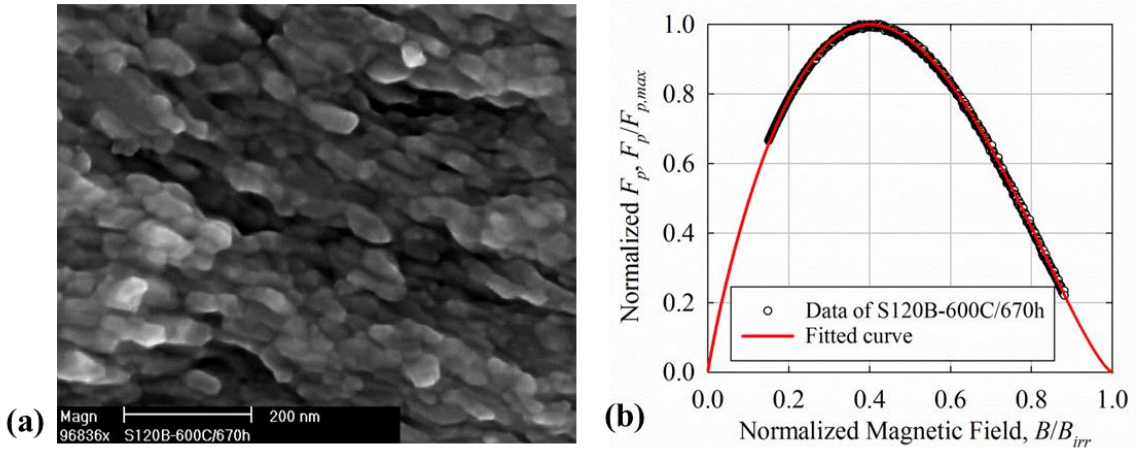

Figure 60. (a) SE image of the fractured surface of an internally oxidized PIT strand reacted at 600 °C, and (b) its normalized F_p-B curve at 4.2 K with a fit using the general scaling law.

Herein, it can be concluded that when grain size is above ≈50 nm, a decrease of the grain size only shifts the F_p-B curve upward (while the peak remains at $0.2B_{irr}$). However, as grain size goes below a threshold of ~50 nm, not only does $F_{p,max}$ increase, but also the F_p-B curve peak shifts to higher fields, which gives extra benefit for high-field J_c

improvement. Why does the F_p-B curve of a Nb_3Sn superconductor with grain size of around 100 nm peak at $0.2B_{irr}$, while the peak shifts toward $0.5B_{irr}$ as the grain size is reduced down to 15-30 nm? Possible explanations are as follows. The case where grain size is several times larger than the flux line spacing (which is about 10-20 nm at >6 T) was addressed by Kramer [32]. In this case, a large fraction of fluxons are not directly pinned by grain boundaries; Lorentz forces F_L on these flux lines are transferred to those directly-pinned fluxons through the rigidity of the flux line lattice (or equivalently, the repulsion force among the flux lines). For small J_c, the F_L is small, so the flux line lattice undergoes elastic deformation, which is a reversible process and does not dissipate heat. Once the J_c is high enough so that the F_L exceeds the shear strength of the flux line lattice, the lattice undergoes plastic deformation, during which process heat is generated and the superconductivity is destroyed. In this case, F_p is limited by the shear strength of the fluxon lattice, causing the F_p-B curve to peak at $0.2B_{irr}$; a detailed derivations for the expression of F_p-B relation were developed by Kramer [32]. As grain size is comparable to flux line spacing, on the other hand, flux lines interact with grain boundaries individually [130], so loss in superconductivity is only possible if the Lorentz force is high enough for flux lines to break free from the pinning of grain boundaries; in this case the bulk pinning force per volume, F_p, is a direct summation of pinning force on each flux line, making the F_p-B curve peak at $0.5B_{irr}$.

To improve the B_{irr} of the above tube type monofilament with SnO_2 powder, an attempt to add Ti to the Sn core of this strand via Sn-Ti alloy was performed, with the BSE image shown in Figure 61 (a). However, it turned out that after a reaction at 650 °C,

less than 0.5 at.% O was absorbed by Nb-1Zr, as calculated from the *m-T* curve of the residual Nb-1Zr in Figure 61 (b). This indicates that the addition of Ti prevented the absorption of oxygen by Nb-1Zr alloy.

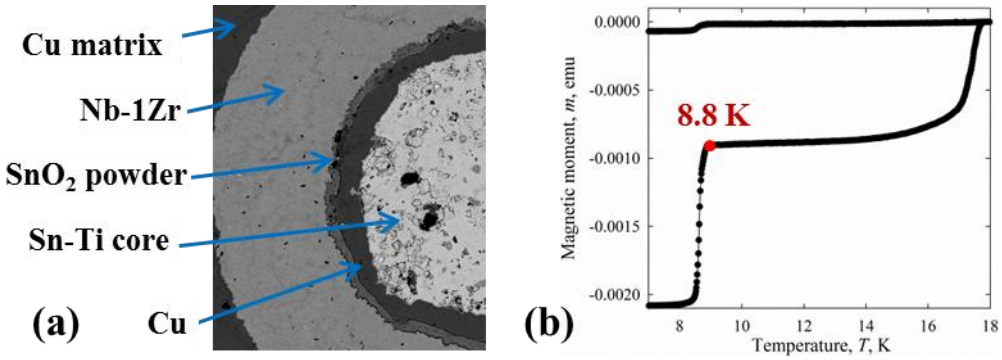

Figure 61. (a) SEM image of a tube type filament with Ti addition via Sn-Ti core, and (b) *m-T* curve of this strand after being reacted at 650 °C.

A possible reason is that after liquid Sn-Ti and Cu mixed, Ti in the Cu-Sn-Ti liquid was exposed to the SnO_2 powder, so oxygen and Ti began to react to form TiO_2. The process of the reaction between Ti and oxygen was faster than the process of oxygen diffusing into Nb-Zr alloy for two reasons. First, oxygen diffuses faster in liquid Sn than it does in Nb-Zr alloy [131]. Second, as Ti in the Cu-Sn-Ti liquid next to the SnO_2 powder reacted with oxygen to form TiO_2, the Ti content gradient in the Cu-Sn-Ti liquid promoted Ti diffusion from the center of the core to the Cu-Sn-Ti/SnO_2 interface; since the diffusivity of Ti in Cu-Sn-Ti liquid is fast, there was a continuous supply of Ti and oxygen until either Ti or oxygen was completely consumed up. Since TiO_2 cannot be reduced by Nb because Ti has stronger affinity to oxygen than Nb does, it cannot serve as

Ti source or oxygen source. Therefore, this indicates that for the addition of Ti, either the oxygen source or the Ti source has to be moved away from the core. This can be easily realized in RIT subelements: since the oxygen source is distributed among the Nb alloy filaments, Ti can be added to the Sn core by using Sn-Ti alloy. For tube type and PIT subelements, a possibly feasible plan is, Ti is still added using Sn-Ti alloy in the core, while the oxide powder is put into the axial holes in the Nb-Zr tube wall. Another option is to use ternary alloy, such as Nb-1Zr-7.5wt.%Ta or Nb-1Zr-1.5at.%Ti to add Ta or Ti.

5.5 The prospects for further improvements of Nb_3Sn strands

The above results on the tube type monofilament wire with SnO_2 powder demonstrate that the internal oxidation method can significantly improve the performance of Nb_3Sn strands. Nevertheless, since these results were obtained from a under-reacted, large-size monofilament that was based on binary Nb_3Sn phase, there is still quite a lot of room for further improvement through optimization. So, what is the real limit of the J_c of Nb_3Sn? In this section, we will look forward to the prospects for the performance limit of Nb_3Sn superconducting wires.

First, the high-field J_c of the above monofilament wire with SnO_2 powder reacted at 625 °C for 800 hours can be improved by enhancing its B_{irr} value, which is only about 20 T, much lower than those of present tube type and PIT strands reacted at 625 °C (which are 25-26 T, see Figure 26). The low B_{irr} of this sample is mainly due to two reasons.

First, this wire (with a subelement diameter of 0.22 mm) was highly under-reacted after 800 h at 625 °C. Many studies (for example, Fischer's study on powder-in-tube strands, which is reprinted in Figure 61 [57]) clearly manifest that B_{irr} of a strand increases dramatically with reaction time and that a under-reacted strand can have a highly degraded B_{irr}. For instance, according to Fischer's measurements, while the 4.2 K B_{irr} of the binary PIT strand is above 23 T if fully reacted (for ≥64 h at 675 °C), this value dropped to ≤ 20 T if the reaction time was less than 16 h [57]. The possible origins of low B_{irr} for under-reacted Nb_3Sn strands were already discussed in chapter 4. Thus, it is expected that if the above internal oxidation subelement is processed down to a smaller size (≤ 50 μm) and fully reacted, the B_{irr} should be improved by several tesla. For example, the B_{irr} of the above monofilament with SnO_2 powder reacted at 650 °C for 400 h is 23 T, which is close to the maximum B_{irr} value obtained in Fischer's binary PIT strand reacted at 675 °C, indicating that the Nb_3Sn with ZrO_2 nanoparticles and refined grain size can achieve at least the same B_{irr} with the ordinary strands.

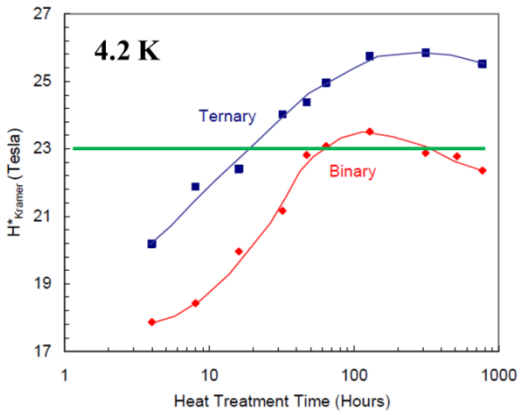

Figure 62. B_{irr} values at 4.2 K obtained by extrapolating Kramer plots of binary and ternary PIT strands, by Fischer [57].

Second, this subelement was based on binary Nb_3Sn, while present tube type, PIT and RRP strands all have Ta or Ti additions, which are well known to effectively improve the B_{irr} of Nb_3Sn. As shown by Fischer's measurements (Figure 62), addition of 4 at.% Ta led to an improvement of B_{irr} from 23 T to > 25 T. Thus, addition of Ta or Ti dopants to internal oxidation subelements could be an effective way for B_{irr} improvement. The approaches to add Ta or Ti in the above structures have been discussed in section 5.4.

Suppose by adding Ti, we can increase the 4.2 K B_{irr} to 25 T while still keeping grain size of 36 nm, then what will be the J_c like? As demonstrated in the previous mono-filament with SnO_2 powder, at such a grain size, F_p-B curve peaks at $1/3B_{irr}$, and $F_{p,max}$ is 180 GN/m^3. The F_p-B curve of this case is shown as this red curve in Figure 63, along with that for the present RRP wires shown in black. As can be seen, the 12 T, 15 T, and 20 T J_c are improved by factors of 2.7, 3, and 3.5, respectively.

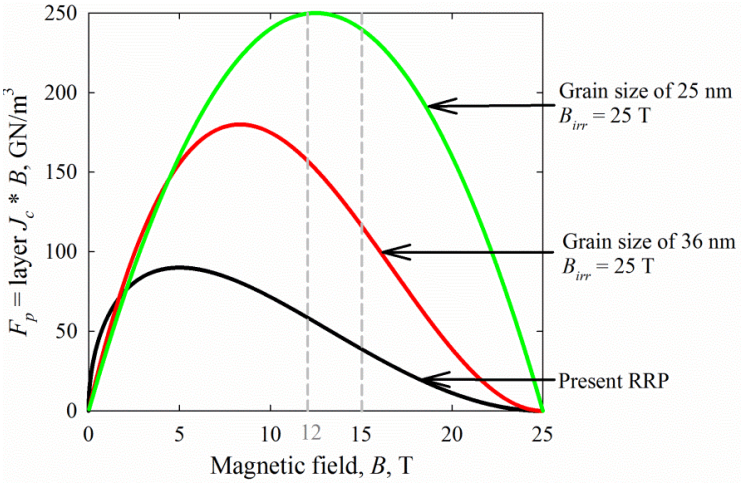

Figure 63. The F_p-B curves (4.2 K) of the three specified cases.

Second, the grain size of the wire with SnO_2 powder reacted at 625 °C is 36 nm. It is still possible to further refine grain size. First, the commercially available Nb-1%Zr alloy was used in the above monofilament wire; the use of Nb-Zr alloy with higher Zr content may generate a greater density of ZrO_2 particles for more effective grain size refinement. Second, this large-size monofilament was heat treated at 625 °C for 800 hours, but for practical strands with much smaller subelement size, the reaction time could be much shorter, which should lead to smaller grain size. Suppose by using higher Zr content, the grain size can be reduced down to 25 nm, then by extrapolating the curve in Figure 59 (a), it can be estimated that the $F_{p,max}$ may reach 250 GN/m^3. As mentioned in section 4.1, the grain size of 15-30 nm causes the F_p-B curve peak to move to $0.5B_{irr}$. Herein, the F_p-B curve of this case is shown as the green curve in Figure 63. Apparently, there is still huge room for further improvement of high-field J_c of Nb_3Sn superconductors by further refining grain size.

Chapter 6: Summary and Conclusions

This dissertation involves the efforts to further improve the high-field J_c of superconducting Nb_3Sn strands. From study of literature, it is summarized that the non-matrix J_c of a Nb_3Sn strand is mainly determined by the following factors: the current-carrying Nb_3Sn area fraction in a subelement, the Nb_3Sn layer J_c, which is further determined by the irreversibility field B_{irr}, and the pinning characteristic. Prospects to improve these three factors (Nb_3Sn area fraction, B_{irr}, and pinning) were explored in the chapters 3, 4, and 5, respectively. In chapter 3, how do the architecture and fractions of Cu, Nb, and Sn precursors influence the Nb_3Sn area fraction in a subelement is discussed. In chapter 4, a thermodynamic/kinetic model is developed to study the Sn source/Nb_3Sn/Nb diffusion reaction couple, and how each factor influences the stoichiometry of Nb_3Sn is explored. In chapter 5, a method to form nano-particles in Nb_3Sn layer is introduced, which can be used to refine Nb_3Sn grain size and improve the pinning capacity.

As a summary, the performance of a Nb_3Sn strand mainly depends on the following four aspects.

First, since a Nb_3Sn strand is fabricated by heat treating a green-state strand composed of precursors (specifically, Nb, Sn, and Cu metals or alloys), the fractions and

architectures of the precursors have significant influence on both the quality and quantity of the Nb_3Sn phase formed. The influence of this factor on the Nb_3Sn area fraction is explored in chapter 3, and its influence on the Nb_3Sn stoichiometry and B_{irr} is studied in chapter 4.

Second, the additions (such as Ta or Ti) to the precursors, which are finally included into the Nb_3Sn phase after phase transformation, can influence the Nb_3Sn B_{irr}, which is discussed in chapters 1 and 4.

Third, heat treatment temperature and time of a green-state strand can influence both the Nb_3Sn stoichiometry and grain size, which further determine the B_{irr} and pinning capacity, respectively. These are discussed in chapters 1, 4, and 5.

Fourth, other methods can be used to engineer the microstructure. For example, an internal oxidation method is introduced in chapter 5, which needs a proper modification of the precursors (i.e., use of Nb-Zr alloy and addition of oxygen source) to introduce nano-particles to refine Nb_3Sn grain size, in order to improve the pinning capacity.

Furthermore, some of these factors may also influence other factors; for example, the Cu/Nb/Sn ratios and architecture in a strand and its heat treatment can also influence the RRR of this strand.

To design a Nb_3Sn strand with the best performance (i.e., high J_c at high fields, and high RRR and good processibility), it is necessary to take all of these factors into careful consideration.

References

[1] A. Godeke, "Performance boundaries in Nb_3Sn superconductors", Ph.D. dissertation, The University of Twente, Netherland (2005).

[2] C. D. Hawes, "Investigation of the inhomogeneity of a powder-in-tube Nb_3Sn conductor", M.S. thesis, University of Wisconsin-Madison (2000).

[3] J. P. Charlesworth, I. Macphail and P. E. Madsen, "Experimental Work on the Niobium-Tin Constitution Diagram and Related Studies," *J. Mat. Sci.*, **5**, 580-603 (1970).

[4] G. Lefranc and A. Muller, "Effect of Copper Additions to Superconducting Niobium-Tin Sinter Material", *J. Less-Common Met.* **45** 339 (1976).

[5] R. Besson, S. Guyot, and A. Legris, "Atomic-scale study of diffusion in A15 Nb_3Sn", *Phys. Rev. B* **75**, 054105 (2007).

[6] R. Mailfert, B.W. Batterman, J.J. Hanak, "Low temperature structural transformation in Nb_3Sn", *Physics Letters A*, **24**, 315-316 (1967).

[7] R. Bormann, D. Y. Yu, R. H. Hammond, T. H. Geballe, S. Foner and E. J. Mcniff, "Origin of the B_{c2} enhancement in ternary Nb-Sn phases", *IEEE Trans. Magn.*, **21**, 1140-1143 (1985).

[8] L. D. Cooley, Y. F. Hu and A. R. Moodenbaugh, "Enhancement of the upper critical field of Nb_3Sn utilizing disorder introduced by ball milling the elements", *Appl. Phys. Lett.*, **88**, 142506 (2006).

[9] A. R. Kaufmann and J. J. Pickett, "Multifilament Nb_3Sn Superconducting Wire", *Bull. Am. Phys. Soc.* **15**, 333 (1970).

[10] M. N. Wilson, Superconducting Magnets, *Oxford University Press*, 139–141 (1983).

[11] Sumption M D and Collings E W, "Modeling current-field instabilities in high performance Nb_3Sn strands in moderate field", *IEEE Trans. Appl. Supercond.* **17**, 2714 -7 (2007).

[12] B. Bordini, "Thermomagnetic Instabilities in Nb_3Sn Superconducting Accelerator Magnets", Ph.D. dissertation, Pisa University (2006).

[13] B. Bordini, E. Barzi, S. Feher, L. Rossi and A. V. Zlobin, "Self-field effects in magneto-thermal instabilities for Nb-Sn strands", *IEEE Trans. Appl. Supercond.* **18**, 1309-12 (2008).

[14] M. D. Sumption, "Stability in Nb_3Sn Conductors; Magnetic and Self-Field Instability Considerations at 4 K and 2 K", *Adv. Cryog. Eng.* **1219** 199-207 (2010).

[15] V. V. Kashikhin and A. V. Zlobin, "Magnetic instabilities in Nb_3Sn strands and cables", *IEEE Trans. Appl. Supercond.* **15**, 1621-4 (2005).

[16] E. Barzi, N. Andreev, V. V. Kashikhin, D. Turrioni and A. V. Zlobin, "Study of Nb_3Sn cable stability at self-field using a SC transformer", *IEEE Trans. Appl. Supercond.* **15**, 1537-40 (2005).

[17] A. K. Ghosh, L. D. Cooley, A. R. Moodenbaugh, J. A. Parrell, M. B. Field, Y. Zhang, S. Hong, "Magnetization studies of high Jc Nb_3Sn strands", *IEEE Trans. Appl. Supercond.* **15**, 3494-7 (2005).

[18] L. D. Cooley, P. S. Chang and A. K. Ghosh, "Magnetization, RRR and Stability of Nb_3Sn Strands with High Sub-element Number", *IEEE Trans. Appl. Supercond.* **17**, 2706-9 (2007).

[19] R. M. Scanlan, D. R. Dietderich, S. A. Gourlay, "A new generation Nb_3Sn wire, and the prospects for its use in particle accelerators", *Adv. Cryo. Eng.* **50** 349-58 (2004).

[20] X. Peng *et al.*, "Strain and Magnetization Properties of High Subelement Count Tube-Type Nb_3Sn Strands", *IEEE Trans. Appl. Supercond.* **21** 2559-62 (2011).

[21] M. J. R. Sandim, D.Tytko, A. Kostka, P. Choi, S. Awaji, K. Watanabe, and D. Raabe, "Grain boundary segregation in a bronze-route Nb_3Sn superconducting wire studied by atom probe tomography", *Supercond. Sci. Technol.* **26**, 055008 (2013).

[22] J. A. Parrell, Y. Z. Zhang, M. B. Field, P. Cisek and S. Hong, "High field Nb_3Sn conductor development at Oxford Superconducting Technology", *IEEE Trans. Appl. Supercond.* **13** 3470-3 (2003).

[23] J. A. Parrell, M. B. Field, Y. Zhang and S. Hong, "Advances in Nb_3Sn strand for fusion and particle accelerator applications", *IEEE Trans. Appl. Supercond.* **15** 1200–4 (2005).

[24] X. Xu, M. D. Sumption, S. Bhartiya, X. Peng and E. W. Collings, "Critical current densities and microstructures in rod-in-tube and Tube Type Nb_3Sn strands – Present status and prospects for improvement", *Supercond. Sci. Technol.* **26** 075015 (2013).

[25] V. Nezareth, "Characterization of the interdiffusion microstructure, A15 layer growth and stoichiometry in tube-type Nb_3Sn composites", M.S. thesis, The Ohio State University (2008).

[26] W. L. Neijmeijer, "Microstructural and Kinetic studies of the manufacturing of superconducting Nb_3Sn", Ph.D. dissertation, The University of Twente (1988).

[27] W. L. Neijmeijer and B. H. Kolster, "Microstructure and Kinetics of the Formation of Nb_3Sn from Reaction between Nb_6Sn_5 and Nb", *Z. Metallkd.* **81** 314-21 (1990).

[28] L. R. Motowidlo, P. J. Lee, and D. C.Larbalestier, "The Effect of Second Phase Additions on the Microstructure and Bulk Pinning Force in Nb_3Sn PIT Wire", *IEEE Trans. Appl. Supercond.* **19**, 2568-2572 (2009).

[29] T. Boutboul, L. Oberli, A. den Ouden, D. Pedrini, B. Seeber, and G. Volpini, "Heat treatment optimization studies on PIT Nb_3Sn strand for the NED project," *IEEE Trans. Appl. Supercond.*, **19**, 2564 – 2567 (2009).

[30] M. Suenaga, A. K. Ghosh, Y. W. Xu, D. O. Welch, "Irreversibility Temperatures of Nb_3Sn and Nb-Ti", *Phys Rev Lett.* **66**, 1777-1780 (1991).

[31] L. D. Cooley, C. M. Fischer, P.J. Lee, D.C. Larbalestier, "Simulations of the effects of tin composition gradients on the superconducting properties of Nb_3Sn conductors", *J. Appl. Phys.* **96**, 2122-2130 (2004).
[32] E. J. Kramer, "Scaling Laws for Flux Pinning in Hard Superconductors", *J. Appl. Phys.* **44**, 1360-1370 (1973).
[33] M. Suenaga, "Metallurgy of continuous filamentary A15 superconductors", technical report, Brookhaven National Laboratory (1980).
[34] R. Flukiger, D. Uglietti, C. Senatore, F. Buta, "Microstructure, composition and critical current density of superconducting Nb_3Sn wires", *Cryogenics*. **48**, 293-307(2008).
[35] J. E. Kunzler, E. Buehler, F. S. L. Hsu, and J. H. Wernick, "Superconductivity in Nb_3Sn at High Current Density in a Magnetic Field of 88 kgauss", *Phys Rev lett.* **6**, 89-91(1961).
[36] R. M. Scanlan, W. A. Fietz, E. F. Koch, "Flux Pinning Centers in Superconducting Nb_3Sn", *J. Appl. Phys.* **46**, 2244-2249 (1975).
[37] W. Schauer, W. Schelb, "Improvement of Nb_3Sn High-Field Critical Current by a 2-Stage Reaction", *IEEE Trans. Magn.* **17**, 374-377 (1981).
[38] P. J. Lee and D. C. Larbalestier, "Microstructure, Microchemistry and the Development of Very High Nb_3Sn Layer Critical Current Density", *IEEE Trans. Appl. Supercond.* **15**, 3474-3477 (2005).
[39] X. Xu, M. D. Sumption, and E. W. Collings, "Influence of Heat Treatment Temperature and Ti doping on Low Field Flux Jumping and Stability in (Nb-Ta)$_3$Sn Strands," *Supercond. Sci. Technol.* **27**, 095009 (2014).
[40] W. Schelb. "Electron microscopic examination of multifilamentary bronze-processed Nb_3Sn," *J Mater Sci.* **16**, 2575-2582 (1981).
[41] D. Dietderich and R. Scanlan, "Nb_3Sn artificial pinning microstructures", *IEEE Trans. Appl. Supercond.* **7**, 1201-1204 (1997).
[42] D. R. Dietderich and A. Godeke, "Nb_3Sn research and development in the USA – wires and cables", *Cryogenics* **48**, 331-340 (2008).
[43] R. Zhou, "Processing and characterization of Nb and Nb_3Sn superconductors with artificial pinning centers", Ph.D. dissertation, Rutgers University (1994).
[44] D. Rodrigues, Jr., L. B. S. Da Silva, C. A. Rodrigues, N. F. Oliveira, Jr., and C. Bormio-Nunes, "Optimization of Heat Treatment Profiles Applied to Nanometric-Scale Nb_3Sn Wires With Cu-Sn Artificial Pinning Centers", *IEEE Trans. Appl. Supercon.* **21**, 3150-3 (2011).
[45] X. Peng, M. D. Sumption, R. Dhaka, M. Bhatia, M. Tomsic, E. Gregory, and E. W. Collings, "Composition profiles and upper critical field measurement of internal-Sn and tube-type conductors", *IEEE Trans. Appl. Supercond.* 17, 2668-2671 (2007).
[46] R. D. Parks, *Superconductivity*, Marcel Dekker, New York (1969).
[47] P. G. de Gennes, *Superconductivity of Metals and Alloys*, Westview Press, New York (1966).

[48] T. P. Orlando, M. R. Beasley, E. J. Mcniff, S. Foner, "Critical Fields, Pauli Paramagnetic Limiting, and Material Parameters of Nb_3Sn and V_3Si", *Phys Rev B* **19**, 4545-4561 (1979).
[49] T. P. Orlando, *et al.* , "The Role of Disorder in Maximizing the Upper Critical-Field in the Nb-Sn System", *IEEE Trans. Magn.* **17**, 368-369 (1981).
[50] J. J. Hanak, K. Strater, and R.W. Cullen, *RCA Review* **25**, 342 (1964).
[51] A. Godeke, "A review of the properties of Nb_3Sn and their variation with A15 composition, morphology and strain state", *Supercond. Sci. Technol.* **19**, R68-R80 (2006).
[52] H. Flukiger, W. Schauer, W. Specking, B. Schmidt, E. Springer, "Low temperature phase transformation in Nb_3Sn multifilamentary wires and the strain dependence of their critical current density", *IEEE Trans. Magn.* **17**, 2285-2288 (1981).
[53] J. W. Ekin et al., "Compressive Pre-Strain in High-Niobium-Fraction Nb_3Sn Superconductors", *IEEE Trans. Appl. Supercon.* **15**, 3560-3 (2005).
[54] S. Foner and E.J. McNiff Jr., "Upper Critical Fields of Cubic and Tetragonal Single-Crystal and Polycrystalline Nb_3Sn in Dc-Fields to 30-Tesla" *Solid State Commun.* **39**, 959-964 (1981).
[55] J. Zhou, Y. J. Jo, Z. H. Sung, H. D. Zhou, P. J. Lee, D. C. Larbalestier, "Evidence that the upper critical field of Nb_3Sn is independent of whether it is cubic or tetragonal", *Appl. Phys. Lett.* **99**, 122507 (2011).
[56] J. Zhou, "The effects of variable tin content on the properties of A15 superconducting niobium-3-tin", Ph.D. thesis, Florida State University (2011).
[57] C. M. Fischer, "Investigation of the relationships between superconducting properties and Nb_3Sn reaction conditions in Powder-in-Tube Nb_3Sn", M.S. Thesis, University of Wisconsin-Madison (2002).
[58] K. Togano, T. Asano, K. Tachikawa, "Effects of Magnesium Addition to the Cu-Sn Matrix in the Composite-Processed Nb_3Sn Superconductor", *J. Less-Common Met* **68**, 15-22 (1979).
[59] T. Takeuchi, T. Asano, Y. Iijima, K. Tachikawa, "Effects of the Iva Element Addition on the Composite-Processed Superconducting Nb_3Sn", *Cryogenics* **21**, 585-590 (1981).
[60] M. Suenaga, D. O. Welch, R. L. Sabatini, O. F. Kammerer, S. Okuda, "Superconducting Critical-Temperatures, Critical Magnetic-Fields, Lattice-Parameters, and Chemical-Compositions of Bulk Pure and Alloyed Nb_3Sn Produced by the Bronze Process", *J. Appl. Phys.* **59**, 840-853 (1986).
[61] J. Wecker, R. Bormann, H. C. Freyhardt, "Effects of Additives on the Superconducting Properties of Powder-Metalurgically Produced Cu-Nb_3Sn Composite Wires", *J. Appl. Phys.* **54**, 3318-3324 (1983).
[62] C. V. Renaud, W. T. Nachtrab, and T. Wong, "Observations on Titanium Diffusion in ITT Type Nb_3Sn Superconductors", *IEEE Trans. Appl. Supercon.* **21**, 2579-2583 (2011).

[63] M. Cantoni, C. Scheuerlein, P. Y. Pfirter, F. de Borman, J. Rossen, G. Arnau, L. Oberli, and P. Lee, "Sn concentration gradients in Powder-in-Tube superconductors", *J. Phys.* **234**, 022005 (2010).

[64] J. D. Livingston, "Effect of Ta additions to bronze-processed Nb_3Sn superconductors", *IEEE Trans. Magn.* **14**, 611-613 (1978).

[65] X. Wu, X. Peng, M. D. Sumption, E. Gregory, M. Tomsic and E. W. Collings, "Titanium diffusion and phase formation in tube-type rod-in-tube and internal-tin Nb_3Sn strands", *Adv. Cryo. Eng.* **52**, 504-12 (2006).

[66] S. Bhartiya, M.D. Sumption, X. Peng, E. Gregory, M.J.Tomsic, D. Doll, and E. W. Collings, "Comparison of A15 Stoichiometry and Grain Morphology in Internal Sn and Tube Type Strands; Influence of Strand Design, HTs and Alloying," *Adv. Cryog. Eng.* **56**, 175-182 (2010).

[67] S. Bhartiya, "A15 stoichiometry and grain morphology in rod-in-tube and Tube Type Nb_3Sn strands; Influence of strand design, heat treatments and ternary additions", M.S. thesis, The Ohio State University (2010).

[68] L. F. Goodrich, N. Cheggour, X. F. Lu, J. D. Splett, T. C. Stauffer and B. J. Filla, "Method for determining the irreversible strain limit of Nb_3Sn wires", *Supercond. Sci. Tech.* **24**, 075022 (2011).

[69] A. K. Ghosh, E. A. Sperry, J. D'Ambra, L. D. Cooley, "Systematic changes of the Nb-Sn reaction with time, temperature, and alloying in restacked-rod-process (RRP) Nb_3Sn strands", *IEEE Trans. Appl. Supercond.* **19**, 2580-3 (2009).

[70] X. Xu, E. W. Collings, M. D. Sumption, C. Kovacs and X. Peng, "The effects of Ti addition and high Cu/Sn ratio on tube type $(Nb,Ta)_3Sn$ strands, and a new type of strand designed to reduce unreacted Nb ratio", *IEEE Trans. Appl. Supercond.* **24**, 6000904 (2014).

[71] L. R. Motowidlo, J. Distin, P. J. Lee, D. C. Larbalestier, A. K. Ghosh, "New Developments in Nb_3Sn PIT Strand: The Effects of Titanium and Second Phase Additions on the Superconducting Properties", *IEEE Trans. Appl. Supercond.* **21**, 2546-2549 (2011).

[72] P. J. Lee, J. R. Ruess and D. C. Larbalestier, "Quantitative image analysis of filament coupling and grain size in ITER $Nb(Ti)_3Sn$ strand manufactured by the internal Sn process", *IEEE. Trans. Appl. Supercon.* **7**, 1516-9 (1997).

[73] X. Xu, M. Majoros, M. D. Sumption, and E. W. Collings, "Persistent-Current magnetization of Nb_3Sn Strands: Influence of Applied Field Angle and Transport Current", *IEEE Trans. Appl. Supercond.* **25**, 8200704 (2015).

[74] M. T. Naus, "Optimization of internal-Sn Nb_3Sn conposites", Ph.D. thesis, The University of Wisconsin-Madison (2002).

[75] S. Bhartiya, M. D. Sumption, X. Peng, E. Gregory, M. J. Tomsic, E. W. Collings, "Investigation of the Effects of Low Temperature Heat Treatments on the Microstructure and Properties of Multifilamentary, Tube-Type Nb_3Sn Strands", *IEEE Trans. Appl. Supercond.* **19**, 2588-2592 (2009).

[76] K. T. Hartwig, S. Balachandran, R. Mezyenski, N. Seymour, J. Robinson and R. E. Barber, "Fabrication of fine-grain tantalum diffusion barrier tube for conductors", *AIP Conf. Proc.* **1574**, 204 (2014).

[77] C. Scheuerlin et al., "Phase transformations during the reaction heat treatment of Nb_3Sn superconductors", *Journal of Physics: Conference Series* **234**, 022032 (2010).
[78] X. Xu, M. D. Sumption, E. W. Collings, "A Model for Phase Evolution and Volume Expansion in Tube Type Nb_3Sn Conductors," *Supercond. Sci. Technol.* **26**, 125006 (2013).
[79] W. L. Neijmeijer and B. H. Kolster, "The Ternary-System Nb-Sn-Cu at 675°C", *Z. Metallkd.* **78** 730-37 (1987).
[80] I. Pong, L.Oberli and L. Bottura, "Cu diffusion in Nb_3Sn internal tin superconductors during heat treatment", *Supercond. Sci. Technol.* **26**, 105002 (2013).
[81] C. Scheuerlein, M. Di Michiel, G. Arnau, R. Flükiger, F. Buta, I. Pong, L. Oberli, and L. Bottura, "Coarse Nb_3Sn Grain Formation and Phase Evolution During the Reaction of a High Sn Content Internal Tin Strand", *IEEE Trans. Appl. Supercon.* **21**, 2554 (2011).
[82] M. C. Jewell, A. Godeke, P. J. Lee, D. C. Larbalestier, "The upper critical field of stoichiometric and off-stoichiometric bulk, binary Nb_3Sn", *Adv. in Cryo.Eng.* **711**, 474-481(2004).
[83] R. Dhaka, "Sn and I diffusion, phase formation, stoichiometry, and superconducting properties of internal-Sn-type Nb_3Sn conductors", M.S. thesis, The Ohio State University (2007).
[84] V. Abächerli, D. Uglietti, P. Lezza, B. Seeber, R. Flükiger, M. Cantoni, and P. A. Buffat, "The Influence of Ti Doping Methods on the High Field Performance of $(N,Ta,Ti)_3Sn$ Multifilamentary Wires Using Osprey Bronze", *IEEE Trans. Appl. Supercon.* **15**, 3482 (2005).
[85] A. K. Kumar and A. Paul, "Interdiffusion and Growth of the Superconductor Nb_3Sn in Nb/Cu(Sn) Diffusion Couples", *J. Electron. Mater.* **38**, 700-705 (2009).
[86] G. Rupp, "The importance of being stressed", in Filamentary A15 Superconductors, edited by M. Suenaga and A. F. Clark, Plenum (1980).
[87] D. Smarthers and D. Larbalestier, "An Auger Electron Spectroscopy Study of Bronze Route Niobium-Tin Diffusion Layers", in Filamentary A15 Superconductors, edited by M. Suenaga and A. F. Clark, Plenum (1980).
[88] C. Tarantini1, Z-H. Sung, P. J. Lee, A. K. Ghosh and D. C. Larbalestier, "Significant enhancement of compositional and superconducting homogeneity in Ti rather than Ta-doped Nb_3Sn", *Appl. Phys. Lett.* **108**, 042603 (2016).
[89] N. Banno, Y. Miyamoto, and K. Tachikawa, "Multifilamentary Nb_3Sn wires fabricated through internal diffusion process using brass matrix", *IEEE Trans. Appl. Supercon.* DOI: 10.1109/TASC.2016.2531123 (2016).
[90] M. Kim, S. Baek, U. Paik, S. Nam, & J. Byun, "Electrical conductivity and oxygen diffusion in nonstoichiometric TiO_{2-x}", *J. Korean Phys. Soc.* **32**, S1127-S1130 (1998).
[91] S. I. Park, C. C. Tsuei, & K. N. Tu, "Effect of oxygen deficiency on the normal and superconducting properties of $YBa_2Cu_3O_{7-\delta}$", *Phys. Rev. B* **37**, 2305-2308 (1988).

[92] R. D. Noebe, R. R. Bowman, & M. V. Nathal, "Physical and mechanical properties of the B2 compound NiAl", *Int. Mater. Rev.* **38**, 193-232 (1993).
[93] M. Suenaga, in Superconductor Materials Science: Metallurgy, Fabrication, and Applications, edited by S. Foner and B. B. Schwartz, Plenum (1981).
[94] H. H. Farrell, G. H. Gilmer, & M. J. Suenaga, "Grain boundary diffusion and growth of intermetallic layers: Nb_3Sn", *J. Appl. Phys.* **45**, 4025-4035 (1974).
[95] U. Gosele, & K. N. Tu, "Growth kinetics of planar binary diffusion couples: "Thin-film case" versus "Bulk cases"", *J. Appl. Phys.* **53**, 3252-3260 (1982).
[96] V. I. Debkov, in Reaction Diffusion and Solid State Chemical Kinetics, 3-19 IPMS (2002).
[97] A. M. Gusak, et al. in Diffusion-controlled Solid State Reactions: In Alloys, Thin Films and Nanosystems, 99-133, Wiley-VCH (2010).
[98] K. N. Tu, & A. M. Gusak, in Kinetics in Nanoscale Materials, 187-193, Wiley-VCH (2014).
[99] A. A. Kodentsov, G. F. Bastin, & F. J. J. van Loo, "The diffusion couple technique in phase diagram determination", *J. Alloy Compd.* **320**, 207-217 (2001).
[100] W. Gong, L. Zhang, H. Wei, & C. Zhou, "Phase equilibria, diffusion growth and diffusivities in Ni-Al-Pt system using Pt/β-NiAl diffusion couples", *Prog. Nat. Sci.* **21**, 221-226 (2011).
[101] T. Laurila, V. Vuorinen, A. K. Kumar, and A. Paul, "Diffusion and growth mechanism of superconductor grown by bronze technique", *Appl. Phys. Lett.* **96**, 231910 (2010).
[102] J. Svoboda, F. D. Fischer, P. Fratzl, & A. Kroupa, "Diffusion in multi-component systems with no or dense sources and sinks for vacancies", *Acta Mater.* **50**, 1369-1381 (2002).
[103] J. Svoboda, F. D. Fischer & P. Fratzl, "Diffusion and creep in multi-component alloys with non-ideal sources and sinks for vacancies", *Acta Mater.* **54**, 3043-3053 (2006).
[104] F. D. Fischer, & J. Svoboda, "Substitutional diffusion in multicomponent solids with non-ideal sources and sinks for vacancies", *Acta Mater.* **58**, 2698-2707 (2010).
[105] Z. W. Cui, F. Gao, & J. M. Qu, "Interface-reaction controlled diffusion in binary solids with applications to lithiation of silicon in lithium-ion batteries", *J. Mech. Phys. Solids.* **61,** 293-310 (2013).
[106] H. Müller and Th. Schneider, "Heat Treatment of Nb_3Sn Conductors", *Cryogenics* **48**, 323 (2008).
[107] R. Besson, S. Guyot, & A. Legris, "Atomic-scale study of diffusion in A15 Nb_3Sn", *Phys. Rev. B* **75,** 054105 (2007).
[108] M. Li, Z. Du, C. Guo, & C. Li, "Thermodynamic optimization of the Cu-Sn and Cu-Nb-Sn systems", *J. Alloys Compd.* **477**, 104-117 (2009).
[109] M. Hansen, & R. P. Anderko, in Constitution of binary alloys, 634, McGraw-Hill (1958).
[110] C. Toffolon, C. Servant, J. C. Gachon, & B. Sundman, "Reassessment of the Nb-Sn system", *J. Phase Equilib.* **23**, 134-139 (2002).

[111] B. V. Reddi, V. Raghavan, S. Ray & A. V. Narlikar, "Growth kinetics of monofilamentary Nb3Sn and V3Ga synthesized by solid-state diffusion", *J Mater. Sci.* **18**,1165-1173 (1983).
[112] J. S. Kirkaldy, R. J. Brigham, and D. H. Weichert, "Diffusion interactions in Cu-Zn-Sn as determined from infinite and finite diffusion couples," *ACTA Metallurgica* **13**, 907-915 (1965).
[113] L. D. Cooley, P. D. Jablonski, P. J. Lee, and D. C. Larbalestier, "Strongly enhanced critical current density in Nb 47 wt. % Ti having a highly aligned microstructure", *Appl. Phys. Lett.* **58**, 2984 (1991).
[114] I. Anzel, A. C. Kneissl, L. Kosec, R. Rudolf, and L. Gusel, *Z. Metallkd.* **2003**, *94*, 993.
[115] D. L Martin, M. G Benz, "Method of making superconductors containing flux traps", US3429032 A (1969).
[116] L. E. Rumaner, M. G. Benz and E. L. Hall, "The Role of Oxygen and Zirconium in the Formation and Growth of Nb_3Sn Grains", *Metall. Mater. Trans. A* **25**, 213-219 (1994).
[117] R. DeHoff, "Thermodynamics in Materials Science", CRC Press, 376-377 (2006).
[118] M. Benz, "Zirconia-stabilized multi-filamentary niobium-tin superconducting wire", US 2003/0085053 A1 (2003).
[119] B. A. Zeitlin, E. Gregory, J. Marte, M. Benz, T. Pyon, R. Scanlan and D. Dietderich, "Results on Mono Element Internal Tin Nb_3Sn Conductors (MEIT) with Nb7.5Ta and Nb(1Zr+Ox) Filaments", *IEEE Trans. Appl. Supercond.* **15**, 3393 (2005).
[120] B. A. Zeitlin, E. Gregory, J. Marte, M, Benz, R. Scanlan, D. Dietderich, "The Effects on the Superconducting Properties on the Addition of Oxygen and Titanium to $(Nb\text{-}1Zr)_3Sn$ Mono Element Internal Tin(MEIT) Conductors", *Adv. Cryo. Eng.* **52B**, 513-519 (2006).
[121] D. L. Corn, "Internal oxidation of niobium alloys containing hafnium and zirconium", Ph. D. University of California (1990).
[122] D.L. Douglass, D, .L. Corn and F. Rizzo, "Internal oxidation of Nb-Zr alloys over the range 1555-1768 °C at low oxygen pressures", *Journal de Physique IV* **03 (C9)**, C9-75-C9-84 (1993).
[123] R. A. Perkins and R. A. Padgett, "Oxygen Diffusion in Niobium and Nb-Zr Alloys", *Acta. Metall.* **25**, 1221-1230 (1977).
[124] H. Mehrer, "Diffusion in Solid Metals and Alloys", Landolt-Börnstein - Group III Condensed Matter (1990).
[125] M. L. Narula, V. B. Tare and W. L. Worrell, "Diffusivity and Solubility of Oxygen in Solid Copper Using Potentiostatic and Potentiometric Techniques", *Metall Trans B* **14**, 673 – 677 (1983).
[126] C. C. Koch, J. O. Scarbrough and D. M. Kroeger, "Effects of Interstitial Oxygen on Superconductivity of Niobium", *Phys. Rev. B* **9**, 888-897 (1974).
[127] X. Xu, M. D. Sumption, X. Peng and E. W. Collings, "Refinement of Nb_3Sn grain size by the generation of ZrO_2 precipitates in Nb_3Sn wires", *Appl. Phys. Lett.* **104** 082602 (2014).

[128] C. Benvenuti, S. Calatroni and V. Ruzinov, "Diffusion of oxygen in niobium during bake-out", *Proceedings of 10th workshop on RF superconductivity,* 441-442 (2001).
[129] Dew-Hughes, "Flux pinning mechanisms in type II superconductors", *Phil. Mag.* **30**, 293-305 (1974).
[130] L. Cooley, X. Song, D. Larbalestier, "Improving flux pinning at high fields in intermetallic superconductors: clues from MgB_2 and $MgCNi_3$", *IEEE Trans. Appl. Supercond.* **13**, 3280 (2003).
[131] S. Otsuka, Z. Kozuka, Y. A. Chang, "Oxygen Solubility in Liquid Indium and Oxygen Diffusivity in Liquid Indium and Tin", *Metall. Trans. B* **15**, 329-335 (1984).